



Michigan Technological University  
*Create the Future* Digital Commons @ Michigan Tech

---

Dissertations, Master's Theses and Master's  
Reports - Open

Dissertations, Master's Theses and Master's  
Reports

---

2014

## WATER TRANSPORT THROUGH POROUS MEDIA AND IN FLOW CHANNELS OF PROTON EXCHANGE MEMBRANE FUEL CELL

Mehdi Mortazavi  
*Michigan Technological University*

Follow this and additional works at: <https://digitalcommons.mtu.edu/etds>

 Part of the [Energy Systems Commons](#)


Copyright 2014 Mehdi Mortazavi

---

### Recommended Citation

Mortazavi, Mehdi, "WATER TRANSPORT THROUGH POROUS MEDIA AND IN FLOW CHANNELS OF PROTON EXCHANGE MEMBRANE FUEL CELL", Dissertation, Michigan Technological University, 2014.  
<https://doi.org/10.37099/mtu.dc.etds/856>

Follow this and additional works at: <https://digitalcommons.mtu.edu/etds>

 Part of the [Energy Systems Commons](#)

WATER TRANSPORT THROUGH POROUS MEDIA AND IN FLOW  
CHANNELS OF PROTON EXCHANGE MEMBRANE FUEL CELL

By

Mehdi Mortazavi

A DISSERTATION

Submitted in partial fulfillment of the requirements for the degree of

DOCTOR OF PHILOSOPHY

In Mechanical Engineering-Engineering Mechanics

MICHIGAN TECHNOLOGICAL UNIVERSITY

2014

© 2014 Mehdi Mortazavi

This dissertation has been approved in partial fulfillment of the requirements for the Degree of DOCTOR OF PHILOSOPHY in Mechanical Engineering-Engineering Mechanics.

Department of Mechanical Engineering - Engineering Mechanics

**Dissertation Advisor:** *Dr. Kazuya Tajiri*

**Committee Member:** *Dr. Jeffrey Allen*

**Committee Member:** *Dr. Reza Shahbazian Yassar*

**Committee Member:** *Dr. Wenzhen Li*

**Department Chair** *Dr. William W. Predebon*

# Contents

Table of Contents . . . . .	iii
List of Figures . . . . .	vii
List of Tables . . . . .	xiii
preface . . . . .	xv
Abstract . . . . .	xvii
<b>1 Introduction . . . . .</b>	<b>1</b>
<b>2 In-Plane Microstructure of Gas Diffusion Layers With Different Properties for PEFC . . . . .</b>	<b>4</b>
2.1 Abstract . . . . .	4
2.2 Introduction . . . . .	5
2.3 Experimental . . . . .	8
2.4 Results and discussion . . . . .	12
2.4.1 Contact Angle . . . . .	12
2.4.2 Mean Pore Diameter . . . . .	16
2.4.3 Pore Diameter Distribution . . . . .	19
2.4.4 In-Plane Variation of Pore Diameter Distribution . . . . .	20
2.4.5 Pore Roundness Distribution . . . . .	21
2.4.6 Effect of Threshold on Mean Pore Diameter . . . . .	24
2.5 Conclusion . . . . .	24



<b>3</b>	<b>Liquid water breakthrough pressure through gas diffusion layer of proton exchange membrane fuel cell . . . . .</b>	<b>27</b>
3.1	abstract . . . . .	27
3.2	Introduction . . . . .	28
3.3	Experimental setup . . . . .	31
3.3.1	Water breakthrough experiment . . . . .	31
3.3.2	Sample preparation . . . . .	34
3.3.3	Contact angle measurement . . . . .	34
3.4	Results and discussion . . . . .	36
3.4.1	Contact angle . . . . .	36
3.4.2	Liquid water breakthrough pressure . . . . .	37
3.5	Conclusion . . . . .	53
<b>4</b>	<b>Effect of the PTFE Content in the Gas Diffusion Layer on Water Transport in Polymer Electrolyte Fuel Cells (PEFCs) . . . . .</b>	<b>55</b>
4.1	Abstract . . . . .	55
4.2	Introduction . . . . .	56
4.3	Experimental setup . . . . .	60
4.3.1	Apparatus design . . . . .	60
4.3.2	High speed imaging . . . . .	64
4.3.3	Contact angle measurement . . . . .	64
4.3.4	Flow condition . . . . .	65
4.4	Results and discussion . . . . .	65
4.4.1	Contact angle . . . . .	65
4.4.2	Droplet growth . . . . .	68
4.4.3	Droplet detachment diameter . . . . .	69

4.5	Conclusion . . . . .	79
<b>5</b>	<b>Two-phase flow pressure drop in flow channels of proton exchange membrane fuel cells-a review . . . . .</b>	<b>81</b>
5.1	abstract . . . . .	81
5.2	Introduction . . . . .	82
5.3	Two-Phase Flow . . . . .	87
5.3.1	Channel classification . . . . .	87
5.3.2	Two-phase flow patterns . . . . .	88
5.3.3	Liquid water transport through the porous GDL . . . . .	93
5.4	Two-Phase Flow Pressure Drop Models . . . . .	94
5.4.1	Homogeneous Equilibrium Model . . . . .	99
5.4.2	Separated Flow Model . . . . .	101
5.5	Pressure Drop with PEM Fuel Cell Application . . . . .	112
5.5.1	Two-phase flow pressure drop for different flow patterns in PEM fuel cell . . . . .	117
5.5.2	Two-phase flow pressure drop and cell performance . . . . .	119
5.5.3	Effect of flow field geometry on the two-phase flow pressure drop	121
5.5.4	Effect of gas stoichiometry on the two-phase flow pressure drop	126
5.5.5	Effect of wettability on the two-phase flow pressure drop . . .	129
5.5.6	Effect of temperature on the two-phase flow pressure drop . .	132
5.5.7	Effect of MPL on the two-phase flow pressure drop . . . . .	136
5.5.8	Hysteresis effects in two-phase flow pressure drop . . . . .	138
5.6	Two-phase flow pressure drop models for the application of PEM fuel cell . . . . .	142
5.7	Conclusion . . . . .	147

<b>6</b>	<b>Two-phase flow pressure drop measurement in PEM fuel cell flow channels . . . . .</b>	<b>150</b>
6.1	abstract . . . . .	150
6.2	Experimental setup . . . . .	151
6.3	Results and discussion . . . . .	155
6.4	Conclusion . . . . .	161
<b>7</b>	<b>Two-phase flow pressure drop during droplet emergence and growth</b>	<b>162</b>
7.1	Introduction . . . . .	162
7.2	Experimental Setup . . . . .	162
7.3	Result and discussion . . . . .	164
7.3.1	Pressure drop and droplet diameter . . . . .	164
7.4	Conclusion . . . . .	170
<b>8</b>	<b>Conclusion . . . . .</b>	<b>172</b>
	<b>Bibliography . . . . .</b>	<b>174</b>
	Appendix-Copyright Permissions	202

# List of Figures

2.1	SEM Image processing steps . . . . .	11
2.2	Droplet contact angle on treated and untreated GDLs . . . . .	14
2.3	GDL mean pore size as a function of its thickness . . . . .	18
2.4	SEM image of different locations on a treated GDL sample . . . . .	20
2.5	Pore diameter distribution for GDLs of different thicknesses . . . . .	21
2.6	Pore diameter distribution for three random locations on untreated TGP_120 . . . . .	22
2.7	Pore roundness distribution of GDLs . . . . .	23
2.8	The variation of calculated mean pore diameter as a function of thresh- old for TGP_060 . . . . .	24
3.1	Experimental setup . . . . .	31
3.2	Drainage phase diagram . . . . .	32
3.3	Experimental range shown on the drainage phase diagram. Dashed lines represent the hypothetical limits of flow regimes. . . . .	33
3.4	Droplets contact angles on GDL samples . . . . .	36
3.5	Liquid water pressure profile, water flow rate $500\mu\ell\text{h}^{-1}$ , TGP-120, 10 wt.PTFE . . . . .	38
3.6	Liquid water breakthrough pressure for untreated and Nafion loaded GDLs. Water flow rate was $500\mu\ell\text{h}^{-1}$ . . . . .	40

3.7	Minimum pore diameter calculated with reconstructed pore-network of GDL. GDL pore diameter distribution reported in Ref. (1) has been utilized. . . . .	42
3.8	Breakthrough pressure measured for different GDLs . . . . .	43
3.9	The ratio of the breakthrough pressure of treated GDLs ( $P_b$ ) to the breakthrough pressure of untreated GDL ( $P_0$ ). Water flow rate was $500\mu\ell h^{-1}$ . The plot also includes the results presented in (2) and (3). . . . .	44
3.10	Water breakthrough pressure for different GDLs, GDL substrate TGP-060 . . . . .	49
3.11	Comparison of pressure profiles for different MPL/GDL configurations at $500\mu\ell/h$ water flow rate . . . . .	50
3.12	Liquid water pressure profile for different water flow rates, GDL sample untreated TGP-060 . . . . .	52
4.1	Experimental apparatus . . . . .	60
4.2	GDL areal mass and PTFE content based on PTFE concentration in emulsion . . . . .	62
4.3	Schematic of experimental setup . . . . .	63
4.4	Contact angle measurement (a) 10 wt. PTFE treated fresh GDL, contact angle = $153.7^\circ \pm 1.57^\circ$ (b) 10 wt. PTFE treated aged GDL, contact angle = $147.3^\circ \pm 1.49^\circ$ (c) untreated fresh GDL, contact angle = $129.7^\circ \pm 8.84^\circ$ . . . . .	67
4.5	Droplet contact angle on treated and untreated GDLs . . . . .	68
4.6	Droplet growth rate under superficial air velocity of $11.1m s^{-1}$ on treated and untreated GDLs . . . . .	69
4.7	Forces applied on a droplet in general configuration . . . . .	70

4.8	Multiple droplets emerging at different breakthrough locations on 10 wt. PTFE GDL surface; (a) breakthrough location for first few droplets (b, c) droplets emerging at different locations after a while . . . . .	71
4.9	Droplet detachment diameter under $11.1 \text{ m s}^{-1}$ superficial air velocity and at different PTFE wt.for treated GDL. Sliding diameter is considered for untreated GDL (runs A1-A5 in Table 5.1). . . . .	72
4.10	Droplet sliding on untreated GDL without detaching . . . . .	74
4.11	Droplet detachment diameter under $40 \text{ m s}^{-1}$ superficial hydrogen velocity with different PTFE wt. (runs H1-H4 in Table 5.1) . . . . .	76
4.12	Droplet detachment diameter under different superficial air velocities and 25 wt.PTFE treated and untreated GDL (runs A1, A3, A6-A8 and A9) . . . . .	77
4.13	Droplet detachment diameter for different hydrogen superficial velocity in gas channel (runs H2, H3, H5-H14) . . . . .	78
5.1	Two phase flow patterns reported by Triplett et al. (4). a) Bubbly flow $j_f = 3.021 \text{ m/s}$ , $j_g = 0.083 \text{ m/s}$ b) Slug flow $j_f = 0.213 \text{ m/s}$ , $j_g = 0.154 \text{ m/s}$ c) Churn flow $j_f = 1.205 \text{ m/s}$ , $j_g = 4.631 \text{ m/s}$ d) Slug-annular flow $j_f = 0.043 \text{ m/s}$ , $j_g = 4.040 \text{ m/s}$ e) Annular flow $j_f = 0.082 \text{ m/s}$ , $j_g = 73.30 \text{ m/s}$ . . . . .	89
5.2	Two phase flow patterns observed in PEM flow channels reported by Zhang et al. (5). a) corner flow with emergence of droplets b) annular film flow c) slug flow . . . . .	91
5.3	Two-phase flow pattern map reported by Lu et al. (6) . . . . .	92

5.4	The two-phase flow pressure drop signature reported by Grimm et al. (7): (a) spikes in pressure drop signature due to slug formation for water flow rate of $0.1\text{m}\ell\text{min}^{-1}$ and air flow rate of 330 sccm, (b) fluctuation in pressure drop due to film flow for water flow rate of $0.04\text{m}\ell\text{min}^{-1}$ and air flow rate of 1981 sccm, (c) pressure drop signature for mist flow for water flow rate of $0.02\text{m}\ell\text{min}^{-1}$ and air flow rate of 2311 sccm. . . . .	118
5.5	Cell performance and the cathode and anode pressure drop reported by Liu et al. (8) Parallel gas flow field fuel cell operating at $25^{\circ}\text{C}$ and $69.6\text{m}\ell\text{min}^{-1}$ oxygen flow rate and $139.3\text{m}\ell\text{min}^{-1}$ hydrogen flow rate.	120
5.6	Pressure drop measured in different flow fields reported by Hsieh et al. (9) . . . . .	123
5.7	Cross-sectional geometries of the gas channels that were considered by Akhtar et al. (10) (a) R1, $1\text{mm} \times 1\text{mm}$ , (b) R2, $0.5\text{mm} \times 1\text{mm}$ , (c) R3, $1\text{mm} \times 0.5\text{mm}$ , (d) R5, $0.5\text{mm} \times 0.5\text{mm}$ , and (e) V1, $0.5\text{mm}$ and $53^{\circ}124$	
5.8	Minimum pressure drop required for drop removal reported by Akhtar et al. (10) . . . . .	124
5.9	Effect of the gas stoichiometry on the pressure drop reported by Anderson et al. (11) . . . . .	127
5.10	Effect of channel wall surface energy on the two-phase flow frictional multiplier reported by Lu et al. (12). (a) $j_f = 3.0 \times 10^{-4}\text{m/s}$ , (b) $j_f = 7.5 \times 10^{-4}\text{m/s}$ . The horizontal axis, $U_G$ , is the superficial gas velocity. . . . .	130
5.11	Effect of temperature on two-phase flow pressure drop reported by Liu et al. (8) . . . . .	133

5.12	Effect of the relative humidity on the two-phase flow frictional multiplier reported by Hussaini and Wang (13) . . . . .	135
5.13	Effect of MPL on the (a) cathode and (b) anode pressure drop reported by Blanco et al. (14). 25BA refers to SGL 25BA (GDL without MPL) and 25BC refers to SGL 25BC (GDL with MPL). . . . .	137
5.14	Pressure drop hysteresis at $j_f = 0.0033\text{ms}^{-1}$ reported by Zhang et al. (15) . . . . .	139
5.15	Effect of the channel inclination angle, $\beta$ , on the two-phase flow pressure drop hysteresis reported by Zhang et al. (16) . . . . .	140
5.16	Effect of temperature on the pressure drop hysteresis reported by Anderson et al. (17) . . . . .	141
5.17	Water introduction model considered by Zhang et al. (18) . . . . .	143
5.18	Comparison of the two-phase flow pressure drop model proposed by Zhang et al. (18) with experimentally measured two-phase flow pressure drop. Line tagging with Equation (10) corresponds to uniform liquid water introduction which is given by Equation 5.28 in the current review. Also line tagging with Equation (11) corresponds to non-uniform liquid water introduction which is given by Equation 5.29 in the current review. . . . .	145
6.1	Photograph and the schematic of the experimental setup . . . . .	153
6.2	Comparing the experimental and theoretical friction factor for single phase air flow. . . . .	155
6.3	Two-phase flow pressure drop predictions based on different models. Air flow rate was considered to be at $1600\text{ml}/\text{min}$ . . . . .	156



6.4	Comparison of experimental two-phase flow pressure drop with models for different mass fluxes at 1600ml/min air flow rate. . . . .	157
6.5	Comparison of experimental two-phase flow pressure drop with English and Kandlikar's model at different air flow rates. . . . .	159
6.6	Comparing the English and Kandlikar's model with Mishima and Hibiki's model for 600ml/min air flow rate . . . . .	160
6.7	Two-phase flow pressure drop profiles for different mass qualities and at 1600ml/min air flow rate. . . . .	160
7.1	Schematic of test section . . . . .	163
7.2	Pressure profile and droplet diameter . . . . .	165
7.3	Normalized droplet projected area at pressure profile change . . . . .	167
7.4	Droplet emergence and growth for 6.66m/s superficial air velocity. The images belong to the first pressure spike shown in Figure 7.2a. The red line in the figure shows the droplet emergence line and the green cross shows the droplet detachment location. The droplet moves $\sim 1.3$ mm from the emergence to the detachment location. . . . .	168
7.5	Drag coefficient and pressure profile change . . . . .	170

# List of Tables

2.1	Properties of GDLs used in this study . . . . .	10
2.2	Contact angle measured for GDLs with different thicknesses . . . . .	15
2.3	Mean pore diameter of GDLs with different thicknesses . . . . .	17
3.1	Water flow rate considered in this study . . . . .	33
3.2	Properties of GDL samples . . . . .	34
3.3	Linear fitting of the pressure profile between points marked on Figure 5, $\text{Pressure} = a \times \text{time} + b$ . . . . .	39
3.4	Breakthrough pressure for different GDL compressions. Water was injected at $500\mu\text{lh}^{-1}$ . GDL becomes more compressed as normalized GDL thickness decreases. . . . .	47
4.1	GDL properties for different PTFE loading . . . . .	61
4.2	Experiment conditions . . . . .	63
5.1	Literature comparing the predicted and measured two-phase flow pres- sure drops . . . . .	97
5.2	Two-phase viscosity model . . . . .	100
5.3	Values of Chisholm parameter (19) . . . . .	102
5.4	Two-phase frictional pressure gradient correlation . . . . .	105
5.5	Literatures studying the pressure drop in PEM fuel cells . . . . .	114

6.1	Test conditions used in this study . . . . .	154
6.2	Test conditions used in Ref.(20) and the lowest air flow rate in the current study . . . . .	159
7.1	Water flow rate considered in this study . . . . .	163

# Preface

The publications presented in this dissertation have been part of research work carried out at Michigan Technological University, during my PhD in the period of 2011-2014. Liquid water transport through gas diffusion layer (GDL) and within the gas flow channels of proton exchange membrane (PEM) fuel cells have been studied.

Chapter 2 presents GDL microstructural properties that have been obtained by analyzing SEM images of GDL samples. The microstructural properties that have been obtained in this chapter are used throughout this dissertation. The contents of this chapter has been published by ASME Journal of Fuel Cell Science and Technology with the copyright permission being provided at appendix. The contributions of the first author (Mehdi Mortazavi) to this article include taking SEM images, analyzing the images with a MATLAB code, analyzing and organizing results, and writing the paper. The contributions of the second author of this article (Kazuya Tajiri) were supervising the progress of the study and proof-reading the article.

Chapter 3 presents liquid water transport through GDL. Liquid water breakthrough pressure has been measured for GDLs with different conditions. The contents of this chapter has been published by International Journal of Hydrogen Energy with the copyright permission being provided at appendix. The contributions of the first author (Mehdi Mortazavi) to this paper include designing and fabricating the experimental setup, running experiments, gathering data, analyzing data, and writing the paper. The contributions of the second author of this paper (Kazuya Tajiri) include supervising the progress of the study and proof-reading the article.

Chapter 4 studies the effect of PTFE content within the GDL on liquid water removal from the surface of the GDL. Air and hydrogen were supplied within gas flow channel of an ex-situ PEM fuel cell setup. The contents of this chapter has been published by

Journal of Power Sources with the copyright permission being provided at appendix. The contributions of the first author of this article (Mehdi Mortazavi) include designing and building the experimental setup, running experiments, gathering data, analyzing data, and writing the paper. The contributions of the second author of this paper (Kazuya Tajiri) include supervising the progress of the study and proof-reading the article.

Chapter 5 reviews the two-phase flow pressure drop for the application of PEM fuel cell. The two-phase flow pressure drop models are reviewed and the effect of different PEM fuel cell working conditions on two-phase flow pressure drop have been reviewed. This paper has been submitted to the Journal of Renewable and Sustainable Energy Reviews and it is still under review. The contribution of the first author of this article (Mehdi Mortazavi) include reviewing all references and writing the paper. The contributions of the second author of this paper (Kazuya Tajiri) include supervising the progress of the study and proof-reading the article.

In Chapter 6, the two-phase flow pressure drop has been measured in an ex-situ PEM fuel cell setup. The measured pressure drop are then compared with the models introduced in Chapter 5. The contents of Chapter 6 will appear in proceeding of ASME 2014 12th Fuel Cell Conference. The contributions of the first author of this article (Mehdi Mortazavi) include designing and fabricating the experimental setup, running experiments, gathering data, analyzing data, and writing the paper. The contributions of the second author of this paper (Kazuya Tajiri) include supervising the progress of the study and proof-reading the article.

# Abstract

Proton exchange membrane (PEM) fuel cell has been known as a promising power source for different applications such as automotive, residential and stationary. During the operation of a PEM fuel cell, hydrogen is oxidized in anode and oxygen is reduced in the cathode to produce the intended power. Water and heat are inevitable byproducts of these reactions. The water produced in the cathode should be properly removed from inside the cell. Otherwise, it may block the path of reactants passing through the gas channels and/or gas diffusion layer (GDL). This deteriorates the performance of the cell and eventually can cease the operation of the cell.

Water transport in PEM fuel cell has been the subject of this PhD study. Water transport on the surface of the GDL, through the gas flow channels, and through GDL has been studied in details. For water transport on the surface of the GDL, droplet detachment has been measured for different GDL conditions and for anode and cathode gas flow channels. Water transport through gas flow channels has been investigated by measuring the two-phase flow pressure drop along the gas flow channels. As accumulated liquid water within gas flow channels resists the gas flow, the pressure drop increases along the flow channels. The two-phase flow pressure drop can reveal useful information about the amount of liquid water accumulated within gas flow channels. Liquid water transport through GDL has also been investigated by measuring the liquid water breakthrough pressure for the region between the capillary fingering and the stable displacement on the drainage phase diagram. The breakthrough pressure has been measured for different variables such as GDL thickness, PTFE/Nafion content within the GDL, GDL compression, the inclusion of a micro-porous layer (MPL), and different water flow rates through the GDL. Prior to all these studies, GDL microstructural properties have been studied. GDL mi-

crostructural properties such as mean pore diameter, pore diameter distribution, and pore roundness distribution have been investigated by analyzing SEM images of GDL samples.

**Keyword:** Water transport, gas diffusion layer, PEM flow channels, two-phase flow

# Chapter 1

## Introduction

Proton exchange membrane (PEM) fuel cell has been known as a promising power source for automotive, residential and stationary applications. While their efficiency is high, they can operate at high volumetric power density without emitting any greenhouse gases. As a PEM fuel cell operates, oxygen is reduced in the cathode and hydrogen is oxidized in the anode. The oxygen reduction reaction is accompanied by water production within the cathode. Some portion of the produced water may hydrate the membrane and improve its proton conductivity. This eventually can increase the performance of the cell. Some other portion of this produced water may transport into the anode by back diffusion. It is also probable that some fraction of the produced water evaporates into the gas channel. However, any excess amount of liquid water may fill open pores in the gas diffusion layer (GDL). As the water amount within the GDL increases, it can ultimately saturate the GDL. GDL saturation blocks the transport of reactants to the catalyst layer and is referred to as flooding. Flooding is reported to significantly decrease the performance of the cell. Water transport phenomena for the application of PEM fuel cell has been the subject of the author's PhD study. Specifically, water transport through the GDL, water transport in the



gas channels, and two-phase flow pressure drop within the gas channels have been studied. Prior to these studies, GDL microstructural properties have been studied by analyzing SEM images taken from GDLs.

GDL is a macro-porous layer that is used for different purposes. It can provide a uniform transport of reactants to the catalyst layer, removes excess water from the membrane by providing pathways of water to the gas channel, mechanically protects the fragile membrane, and provides electrical conductivity between the electrodes and the current collectors. GDL microstructural properties are studied by analyzing SEM images of GDLs. The results obtained from this study is utilized throughout this dissertation. Acquiring a proper knowledge about water transport phenomena for the application of PEM fuel cell demands a detailed investigation about GDL microstructural properties. Properties such as mean pore diameter and pore diameter distribution of Toray carbon papers are investigated in Chapter 2 of this dissertation. In Chapter 3 of this dissertation, water transport through GDL is studied. Different models that previously have been proposed to describe water transport through GDL are introduced and discussed in this chapter. Liquid water breakthrough pressure has been measured for Toray carbon papers with different properties. The effect of adding micro-porous layer (MPL) to GDL has also been studied in this chapter. The microstructural properties reported in Chapter 2 have been utilized for further discussion in Chapter 3.

In Chapter 4 water transport on the surface of the GDL and within gas flow channels has been studied. Generally, liquid water transport through PEM fuel cell flow channels can occur in different patterns, dependin on the water production rate and gas flow rate within the channel. When the water production rate is low and gas flows in a low rate, water can spread over hydrophilic channels and drain via channel corners. This pattern is known as the corner flow. For moderate water production

rate, the corner flow is not capable of removing liquid water with a comparable rate. Therefore the corner flow may change into annular film flow. The instability of thick water films may turn the annular film flow into slug flow which eventually clogs the channel and shuts off the cell. For high gas flow rate, the gas shear force may detach water droplets from the surface of the GDL.

In Chapter 5 a comprehensive review about the topic of two-phase flow in PEM fuel cell flow channels is provided. The literature review includes the two-phase flow pressure drop models that have been proposed over the years and for different engineering applications.

In Chapter 6 the two-phase flow pressure drop have been measure in an ex-situ PEM fuel cell flow channel. Two parallel flow channels have been used with pressure drop measurements reading from one channel. The results are compared with different models that have been discussed in Chapter 5.

In Chapter 7, a high accuracy pressure transducer is synchronized with a high speed camera to record the two-phase flow pressure drop and the image of a growing droplet simultaneously.

## Chapter 2

# In-Plane Microstructure of Gas Diffusion Layers With Different Properties for PEFC

1

### 2.1 Abstract

Gas diffusion layer (GDL) is undoubtedly one of the most complicated components used in a polymer electrolyte fuel cell (PEFC) in terms of liquid and gas transport phenomena. An appropriate fuel cell design seeks a fundamental study of this tortuous porous component. Currently, porosity and gas permeability have been known as some of the key parameters affecting liquid and gas transport through GDL. Although these are dominant parameters defining mass transport through porous layers, there are still many other factors affecting transport phenomena as well as overall cell

---

<sup>1</sup>The contents of this chapter has been published by Journal of Fuel Cell Science and Technology, 2014, Vol. 11, 021002-1021002-9

performance. In this work, microstructural properties of Toray carbon papers with different thicknesses and for polytetrafluoroethylene (PTFE) treated and untreated cases have been studied based on scanning electron microscopy (SEM) image analysis. Water droplet contact angle as a dominant macro-scale property as well as mean pore diameter, pore diameter distribution, and pore roundness distribution as important micro-scale properties have been studied. It was observed that the mean pore diameter of Toray carbon paper does not change with its thickness and PTFE content. Mean pore diameter for Toray carbon papers was calculated to be around  $26\mu\text{m}$  regardless of their thicknesses and PTFE content. It was also observed that droplet contact angle on GDL surface does not vary with GDL thickness. The average contact angle for 10 wt.% PTFE treated GDLs of different thicknesses was measured about  $150^\circ$ . Finally, the heterogeneous in-plane PTFE distribution on the GDL surface was observed to have no effect on mean pore diameter of GDLs.

## 2.2 Introduction

Although Polymer electrolyte fuel cell (PEFC) has gained lots of consideration as a clean type of energy system, there are still some technical challenges needed to be solved before this type of energy system can be commercially released. Among these challenges, one can refer to water management in PEFC. During the operation of a PEFC, oxygen is reduced in the cathode and is accompanied by water production. Some amount of this produced water may fill open pores of gas diffusion layer (GDL). GDL is macro-porous layer with multifunction purposes such as providing a uniform transport of reactants to the catalyst layer, removing excess water from the membrane by providing pathways of water to the gas channel, mechanically protecting the membrane as a fragile thin layer, and providing electrical conductivity between

the electrodes and the current collectors. An appropriate design of GDL has been reported to have a significant contribution on proper water balance within the cell (21–24).

For a continues transport of reactants to the catalyst layer and transport of excess water to the gas channel, GDL pores should be free from accumulated liquid water. Excess water accumulated within the GDL pores and gas flow channels blocks reactants flow to catalyst layer and finally results in oxidant starvation and performance loss. Liquid water accumulated within the GDL pores, emerges from the GDL surface in form of droplet.

Liquid water transport mechanism on GDL surface is a function of superficial gas velocity, defined as the bulk velocity of gas flowing within the channel cross sectional area, and droplet emergence rate (5). While for high superficial gas velocities the drag force from shear gas flow can easily detach water droplet from the GDL surface, moderate or low superficial gas velocity is not capable of detaching the droplet directly from the GDL surface. Instead, droplet grows in size until it touches the gas channel walls and spreads over them. In such cases, capillary flow drains liquid water through the corners, forming annular film flow. For high liquid water production rate and/or low superficial gas velocity, water film will not be drained properly and the channel will be clogged as the liquid film grows.

Water transport mechanisms within the GDL are quite different from liquid water transport on GDL surface and can be categorized into diffusion, pressure driven hydraulic permeation and evaporation (25). Liquid water behavior on GDL surface can be studied by simple optical visualization techniques (5, 26–29) while water behavior within the GDL cannot be monitored easily. Some of the techniques used for studying water behavior within the GDL are X-ray and neutron radiography (30) since both X-ray and neutron beams are capable of penetrating through the GDL. However each

of these techniques has their own drawbacks. For instance, expensive hardware of neutron imaging requires challenging calibration to ensure a reliable data acquisition (31).

It is a common practice to treat GDLs with some hydrophobic media such as polytetrafluoroethylene (PTFE) to enhance gas transport as well as liquid water transport through the pores when the cell is operating at flooding condition (32). Park et al. (33) tested GDLs with different amount of PTFE and obtained I-V curves of a single cell working at different level of relative humidities. They concluded that among different water transport mechanisms within the GDL, evaporation and shear force are more dominant than capillary force and attributed that to relatively large pore diameters of GDLs compared to microporous layer and catalyst layer. Pasaogullari and Wang (34) used one-dimensional analytical solution and concluded that liquid water transport within the GDL is controlled by capillary forces arising from the gradient in phase saturation. Nam and Kaviany (35) studied water transport within the GDL by developing a capillary pressure model and hypothesized that water is distributed as an "upside-down tree" capillary network. Litster et al. (36) followed a fluorescence microscopy technique and visualized liquid water transport in GDL. They suggested that water transport within the GDL is mostly dominated by fingering and channeling in such a way that as a breakthrough path within the GDL forms, liquid water existing in other pathes recede back and find their way through the newly formed breakthrough path. The hereby illustrated literature review highlights different and sometimes opposite hypotheses made regarding liquid water transport through the GDL.

Water transport through and on the surface of GDL can be characterized by two independent parameters of GDL microstructure and pore surface wettability (23). GDL pore diameter, for instance, was known to directly affect the water vapor pres-

sure at which condensation occurs according to Kelvin equation (37) and for a vapor pressures below saturation pressure, water vapor starts condensing in a pore smaller than critical pore diameter (21). In this article, GDL microstructure has been studied by processing SEM images taken from untreated and treated GDLs with different thicknesses. SEM images of Toray carbon papers with different thicknesses have been analyzed to obtain microstructural properties such as mean pore diameter, pore diameter distribution, and pore roundness. Since all of the GDLs used in this study have the same production procedure, it is expected to obtain similar microstructure for all the samples used. Air permeability, on the other hand, is a property that can be used for comparing microstructure of porous materials (3). Very close air permeability of the GDL samples used in this study as listed in Table 1 can be an indication of similar microstructure of Toray carbon papers of different thicknesses (3).

## 2.3 Experimental

Toray carbon papers with different thicknesses were used as GDL in this study. GDLs with manufacturer specified thicknesses of  $110\mu\text{m}$ ,  $190\mu\text{m}$ ,  $280\mu\text{m}$ , and  $370\mu\text{m}$  have been used. For each thickness, untreated and 10 wt.% PTFE treated papers were tested for microstructural analysis. For PTFE treating the GDL samples, Toray carbon papers were loaded with PTFE based on the procedure given in (38). This procedure is described as follows. The substrates were first dipped in PTFE emulsion (60 wt.% dispersion in  $H_2O$ , ALDRICH) for ten hours and then they were put in furnace at  $120^\circ\text{C}$  for one hour to make them dry. In order to make a uniform distribution of the PTFE within the GDL substrates, they were sintered at  $360^\circ\text{C}$  for one hour. Static contact angles of liquid water droplet on GDL samples with different PTFE contents were measured using a house-made setup designed and made specif-

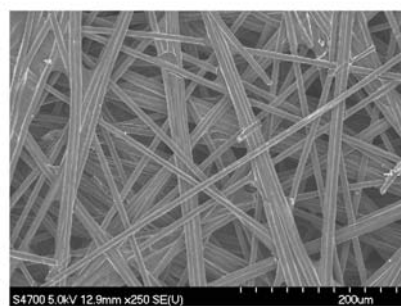
ically for this purpose (39) with procedure and theory given in (40). Ten droplets with diameters within the range of 1mm – 3mm were dropped on GDL surfaces and mean contact angles were considered. Table 1 lists measured and calculated physical properties of the samples used in this study. GDL thicknesses were measured using an electronic micrometer (Mitsutoyo, Japan). The measured thicknesses were slightly different from the thicknesses specified by the manufacturer. However, the manufacturer specified thicknesses are used for the remainder of the paper.

The surface morphology of GDL samples were scanned using a JEOL JSM-6400LV scanning electron microscope (SEM) at 20keV and 250 $\times$  magnification. For each sample, three random locations were chosen and images were obtained. SEM images were analyzed for mean pore diameter, pore diameter distribution, and pore roundness distribution based on the procedure introduced in (41). A MATLAB code was used for analyzing SEM raw images with first applying median filtering (42) to smoothen out high frequency noise. The filtered images were then segmented processed (43) by thresholding based on Otsu method (44) in order to convert the gray level images into binary black and white images. Thus, all carbon fibers became black and empty pores of GDL became white. Finally, the black and white images were gap filled to remove small gaps in the fibers and the pores. In order to make gap filling step more accurate, pore diameters less than 5 $\mu$ m were filtered out in our analysis. Figure 1 shows the four steps of image processing used in this study.

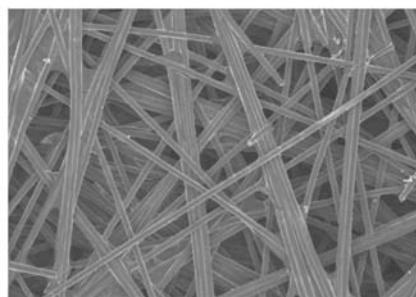


Table 2.1: Properties of GDLs used in this study

Toray Carbon Paper Type	Manufacturer Specified GDL Thickness ( $\mu\text{m}$ )	Manufacturer Specified Porosity	Bulk Density $\text{g cm}^{-3}$	Fiber Diameter $\mu\text{m}$	Air Permeability $(\text{m}^2)$	Areal Mass $(\text{mg cm}^{-2})$	PTFE Concentration in Emulsion (wt.%)
TGP-030	110	80%	-	-	-	4.7	10.4 wt.%
TGP-060	190	76% (78% (3, 45))	0.44 (3)	-	-	8.6	10.3 wt.%
TGP-090	280	78% (80% (46))	0.45 (3)	9.2 (46)	$8.9 \times 10^{-12}$ (46)	12.6	10.5 wt.%
TGP-120	370	78%	0.45 (3)	-	$8.7 \times 10^{-12}$ (27)	16.5	10.4 wt.%



(a) Raw SEM image



(b) Filtered image



(c) Binary black and white image



(d) Gap filled black and white image

Figure 2.1: SEM Image processing steps

## 2.4 Results and discussion

SEM images were processed for microstructural analysis. Analysis includes mean pore diameter, pore diameter distribution and pore roundness distribution for different GDL samples used. Other than conducting a case by case comparison for GDLs of different thicknesses and for treated and untreated sample, pore diameter distribution for one untreated GDL sample (TGP\_120) and at three different locations was also obtained as will be discussed in “In-Plane Pore Distribution” section. These distribution plots may be used to define the order of anisotropy of GDLs in future studies but no quantitative analysis were done on them in this study. Finally, as mentioned in EXPERIMENTAL section, SEM images were processed based on Otsu method for threshold setting. In order to examine the validity of the results obtained based on this approach, the effect of threshold setting on mean pore diameter was also studied. Before all these microstructural analysis, liquid water droplet contact angle on GDLs were measured. Contact angle is a macro-scale property that represents the wetting ability of a solid surface by liquid. It is a function of interfacial energy along the three phase boundary. Measured contact angles can help illuminating the variation of GDL surface energy for different PTFE content within the GDL.

### 2.4.1 Contact Angle

Droplet contact angle describes solid surface interfacial tensions based on the Young’s mechanical equilibrium relation. Liquid droplet contact angle on a solid surface like GDL introduces mechanical equilibrium of the droplet under the influence of three phase interfacial tensions (47). Furthermore, droplet contact angle on GDL surface is one of the most important parameters in water management with application in PEFC since it directly affects some major properties with dominant effects on liquid

water transport within and on GDL surface. Surface adhesion force (given in Eqn. 2.1), drag force from shear gas flow in gas channel (given in Eqn. 2.2), the capillary pressure and even droplet shape on GDL surface are some properties contact angle directly affects. Surface adhesion force keeps the droplet on GDL surface:

$$F_s = 2\sigma_{lv}d_d \sin^2 \theta \sin(\Delta\theta) \quad (2.1)$$

where  $\sigma_{lv}$  is the surface tension between liquid and vapor,  $d_d$  is the diameter of a droplet upon detachment,  $\theta$  is the contact angle and  $\Delta\theta$  is the difference between advancing and receding contact angle (5). Drag force tries to detach the droplet from the GDL surface:

$$F_D = \frac{1}{2}\rho C_D A_P V^2 \quad (2.2)$$

where  $\rho$  is the density of the gas flowing in the gas channel,  $C_D$  is the drag coefficient,  $A_P$  is the droplet projected area perpendicular to the gas flow and  $V$  is the superficial gas velocity.

Static contact angles measured in this study for each GDL sample is shown in Figure 2. Error bars shown represent the standard deviation calculated for each contact angle data point. It can be observed that droplet contact angle significantly changes from an untreated to a treated GDL surface while adding more amount of PTFE does not make any change on the contact angle. Furthermore, it seems that the GDL thickness does not affect the droplet contact angle. As Whitesides and Laibinis (48) reported, droplet behavior on GDL surface is mostly controlled by the wetting characteristics of the top few monolayers of the surface. That is why the thickness of the GDL shows no contribution to the droplet contact angle. Table 2 lists the mean contact angle measured for ten droplets being dropped on GDLs as well as the standard deviation

calculated. For each GDL thickness, droplet contact angles on untreated GDL and treated GDLs with different amount of PTFE are shown. It can be concluded from Table 2 and Figure 2 that the average contact angle droplets make is about  $150^\circ$  on treated GDLs no matter the PTFE content and as mentioned earlier, the GDL thickness has no effect on this contact angle. Similar contact angle on GDLs with different PTFE contents has been observed and reported by other groups such as Fairweather et al. (49) and Benziger et al. (2). It also lead us to draw a conclusion that PTFE particles mostly penetrate through the GDL and agglomerate within the GDL rather than sitting on its surface.

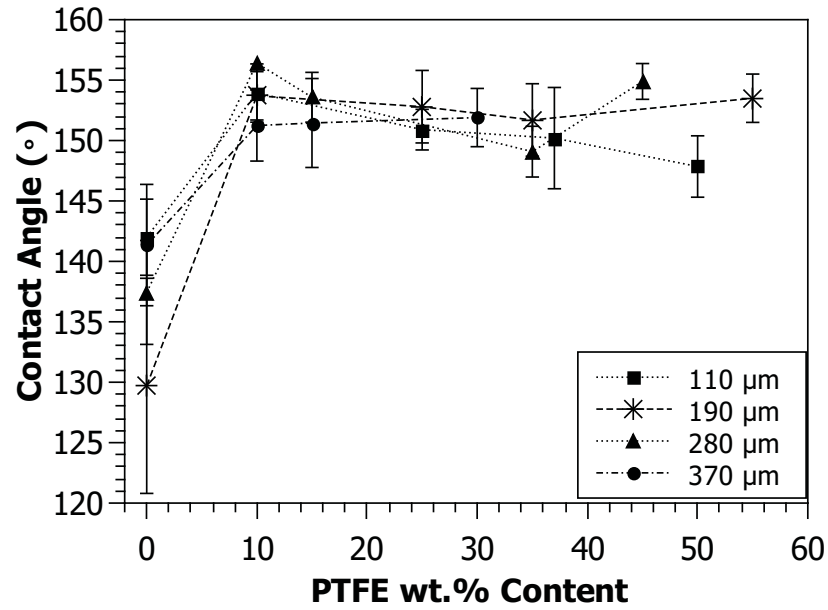


Figure 2.2: Droplet contact angle on treated and untreated GDLs

Table 2.2: Contact angle measured for GDLs with different thicknesses

GDL Type	Contact Angle ( $^{\circ}$ ) (Untreated GDL)	Contact Angle ( $^{\circ}$ ) (PTFE content level #1)	Contact Angle( $^{\circ}$ ) (PTFE content level #2)	Contact Angle( $^{\circ}$ ) (PTFE content level #3)	Contact Angle( $^{\circ}$ ) (PTFE content level #4)
TGP-030	$142.0^{\circ} \pm 3.1^{\circ}$	$153.9^{\circ} \pm 2.4^{\circ}$ (10 wt.%)	$150.9^{\circ} \pm 1.7^{\circ}$ (25 wt.%)	$150.2^{\circ} \pm 4.3^{\circ}$ (37 wt.%)	$147.8^{\circ} \pm 2.5^{\circ}$ (50 wt.%)
TGP-060	$129.7^{\circ} \pm 8.8^{\circ}$	$153.7^{\circ} \pm 2^{\circ}$ (10 wt.%)	$152.8^{\circ} \pm 3^{\circ}$ (25 wt.%)	$151.7^{\circ} \pm 3^{\circ}$ (35 wt.%)	$153.5^{\circ} \pm 2^{\circ}$ (55 wt.%)
TGP-090	$137.4^{\circ} \pm 4.3^{\circ}$	$156.4^{\circ} \pm 1.5^{\circ}$ (10 wt.%)	$153.6^{\circ} \pm 2^{\circ}$ (15 wt.%)	$149^{\circ} \pm 2^{\circ}$ (35 wt.%)	$154.9^{\circ} \pm 1.5^{\circ}$ (45 wt.%)
TGP-120	$141.3^{\circ} \pm 5.0^{\circ}$	$151.2^{\circ} \pm 2.9^{\circ}$ (10 wt.%)	$151.4^{\circ} \pm 3.7^{\circ}$ (15 wt.%)	$151.9^{\circ} \pm 2.4^{\circ}$ (30 wt.%)	NA

### 2.4.2 Mean Pore Diameter

GDLs mean pore diameters were obtained by analyzing SEM images based on the procedure introduced by Parikh et al. (41). For each GDL case, five SEM images were obtained with scan size of  $507\mu\text{m} \times 356\mu\text{m}$  defined by ImageJ software developed by National Institute of Health. The overall mean pore diameter was calculated by averaging mean pore diameters obtained for each SEM image. GDL pore diameter is characterized by *equivalent pore diameter*, EPD, given by Eqn. 2.3:

$$EPD = 2\sqrt{A/\pi} \quad (2.3)$$

where  $A$  is the area of the pore (50).

GDL pore size is one of the most important parameters in liquid water transport from catalyst layer, where water is produced as one of the byproducts of electrochemical reaction, to gas channel, where it can be drained either by detachment caused by shear gas flow or corner flow across the edges of the gas channels (5). Liquid water passes through the GDL pores when its pressure exceeds the capillary pressure, and for a continuous flow, its pressure should remain higher than the capillary pressure (35). Capillary pressure is defined as the difference between the pressure of liquid and gas phase at equilibrium ( $P_c = P_l - P_g$ ) and is a function of mean curvature of water-air interface, contact angle and surface energy:

$$P_c = \frac{2\sigma_{\text{water}} \cos \theta}{r_{\text{pore}}} \quad (2.4)$$

where  $\sigma_{\text{water}}$  is interfacial surface tension,  $\theta$  is the contact angle and  $r_{\text{pore}}$  is the pore radius. The smaller the pore radius, the greater the capillary pressure liquid water should overcome to be able to pass through the GDL. Tamayol and Bahrami (3) modeled GDL as a network of pores connected by throats. Based on their model, it is

assumed that air and liquid water are stored in the pores and the the volume occupied by throats is negligible. Only throats resist liquid water transport and pores do not make any resistance to the flow (51). It was reported that the capillary pressure increases with Toray carbon paper thickness (3). Based on the model argued in (3), as the thickness of the GDL increases, the number of layers forming the GDL also increases. This directly increases the breakthrough pressure of the liquid water. Table 3 lists the mean pore diameter calculated for GDLs of different thicknesses. Based on the results obtained by this approach, GDL mean pore diameter is not changing with GDL thickness and even the mean pore diameter for untreated and treated GDLs are the same. The mean pore diameter obtained for all GDLs is about  $26\mu\text{m}$  which is in well agreement with the mean pore diameter reported by Parikh et al. (41) for Toray carbon paper. The mean pore size given in (27, 52) is within the range of  $30 - 40\mu\text{m}$  that is again in agreement with the results obtained in this work.

Table 2.3: Mean pore diameter of GDLs with different thicknesses

Toray Carbon Paper Type	GDL Thickness ( $\mu\text{m}$ )	Untreated GDL Mean Pore Diameter ( $\mu\text{m}$ )	10 wt.% Treated GDL Mean Pore Diameter ( $\mu\text{m}$ )
TGP-030	110	$25.23 \pm 0.47$	$25.46 \pm 0.86$
TGP-060	190	$25.95 \pm 0.66$	$26.94 \pm 2.27$
TGP-090	280	$27.68 \pm 1.05$	$26.49 \pm 3$
TGP-120	370	$25.45 \pm 0.22$	NA

Considering average pore diameter of  $26\mu\text{m}$ , average contact angle of  $150^\circ$  and water surface tension of  $0.072\text{Nm}^{-1}$ , the capillary pressure will be calculated at  $9.5\text{kPa}$  based on Eqn. 2.4. This pressure is almost twice as much as the breakthrough pressure reported in (53). The reason behind is that for a mean pore diameter of  $26\mu\text{m}$ , there are some pores with larger diameter in the GDLs that result in lower capillary pressure, and as Bazylak et al. (54) had reported, liquid water chooses the



path of least resistance through the GDL and emerge from the surface of the GDL in the form of droplet. Further discussion about pore diameter distribution will be given in next section. Figure 3 shows the calculated mean pore diameter as a function of GDL thickness both for treated and untreated GDL. As mentioned earlier, mean pore diameter does not change neither with GDL thickness nor with PTFE content within the GDL. PTFE particles are within the range of 50 – 500nm (55) that is much smaller than the mean pore diameter.

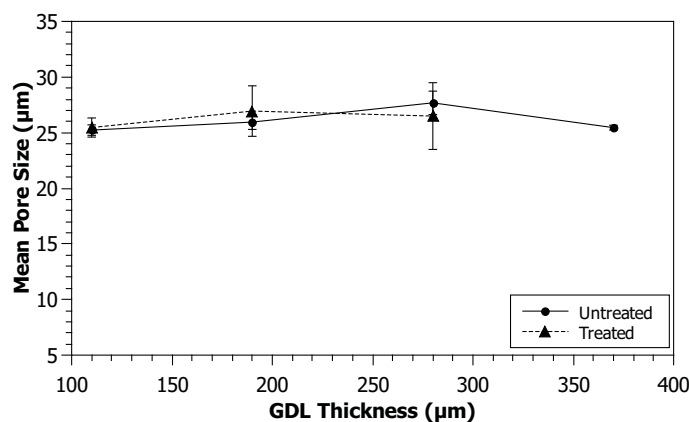


Figure 2.3: GDL mean pore size as a function of its thickness

Figure 2.3 and Table 2.3 also show higher standard deviation of mean pore diameter for treated GDLs compared to untreated ones. SEM images of treated GDL surface are shown in Figure 4. As shown on the Figure 4, the white areas between carbon fibers are PTFE emulsion dried on the surface of the GDL. Figure 4 shows even for the same GDL sample PTFE is not uniformly distributed and there can be some areas with higher PTFE content (Figure 4b) and some areas with lower PTFE content (Figure 4d). Other than uneven PTFE distribution in the plane of the GDL, Figure 4 shows PTFE emulsion mostly covers top layers of the GDL and it seems from the figure that PTFE hardly penetrates into the GDL. Same observation has been reported by Lim and Wang (56) when they took SEM images of carbon papers

treated with fluorinated ethylene propylene (FEP). However, this observation is in discrepancy with the conclusion drawn from contact angle measurement. PTFE distribution through the GDL will be further studied by the authors. Rofaiel et al. (55) had measured heterogeneous through-plane PTFE distribution in carbon papers by using SEM energy dispersive X-ray spectrometry (EDS) and detected larger concentration of fluorine (as PTFE's high concentration element) along the surface fibers and less fluorine in the central region of the GDL. Fishman et al. (57) measured through-plane porosity distribution of GDLs and concluded that PTFE accumulates at local minima near the surface of the paper GDLs. The SEM images taken for this study, however, cannot be used for PTFE through-plane distribution analysis.

### 2.4.3 Pore Diameter Distribution

Pore diameter distributions were obtained from the MATLAB code and are shown in Figure 5 for each GDL sample. It can be concluded that for both treated and untreated GDLs, the majority of pores have diameters of less than  $20\mu\text{m}$ . However, the existence of larger pores mitigate liquid water transport through the GDL by lowering the capillary pressure required for intrusion. Furthermore, pore diameter distributions show the thinnest GDL (TGP\_030) has more number of pores compared to other two GDLs. This can be interpreted as the thinnest GDL is more porous compared to other samples. This result is in well agreement with the manufacturer specified porosity values given in Table 1 although the difference is minor. Pore size distribution could also be obtained by using mercury intrusion porosimetry (MIP) (45, 58). In such technique, mercury as a non-wetting fluid on most surfaces is penetrated into the pores of GDL by applying pressure. The pressure applied is a function of pore diameter. Williams et al. (21) used this approach and obtained pore size distribution for E-TEK carbon paper, E-TEK carbon cloth and SGL carbon

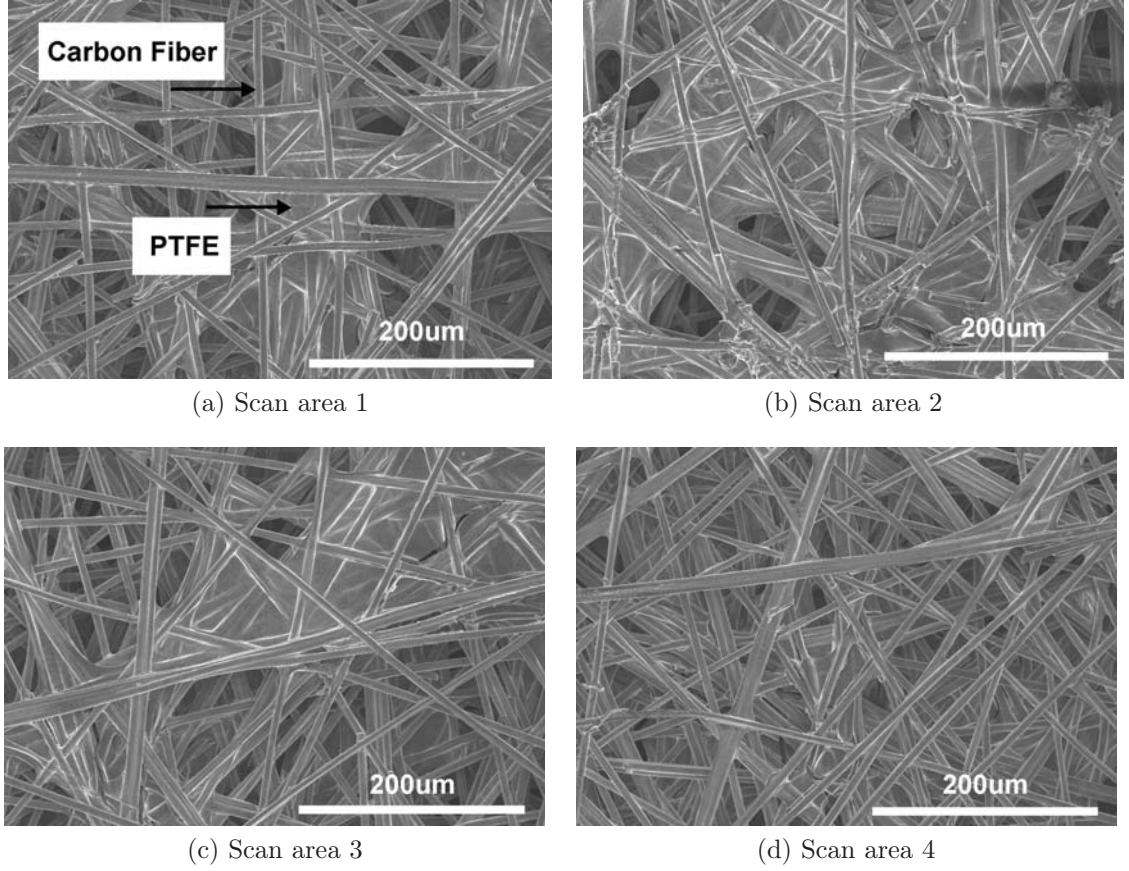
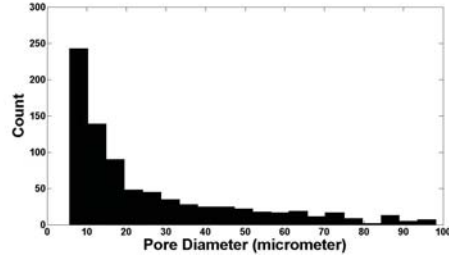


Figure 2.4: SEM image of different locations on a treated GDL sample

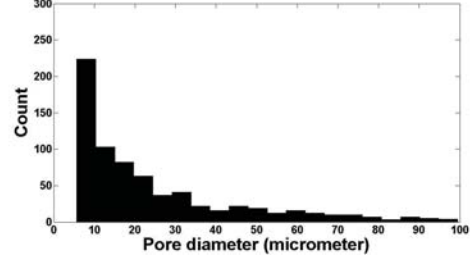
paper.

#### 2.4.4 In-Plane Variation of Pore Diameter Distribution

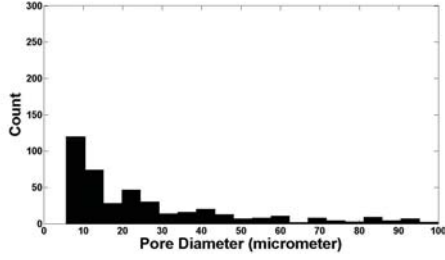
Pore diameter distribution for one GDL and at three random locations on its surface is also studied in this work. Figure 6 shows the pore diameter distribution for three different locations on the untreated thickest GDL (TGP\_120). Although the mean pore calculated for all three cases is about  $25\mu\text{m}$ , the number of pores detected within each range of diameters are different. Again, it can be observed that the majority of pores detected have diameters of less than  $20\mu\text{m}$  while there are larger pores detected



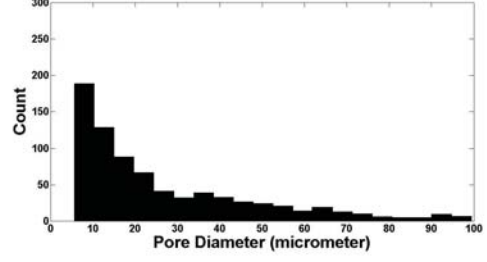
(a) Untreated GDL, TGP\_030, (110 $\mu$ m)



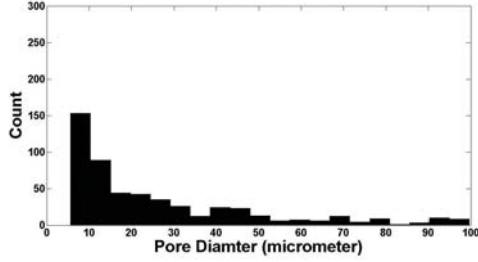
(b) Treated GDL, TGP\_030, (110 $\mu$ m)



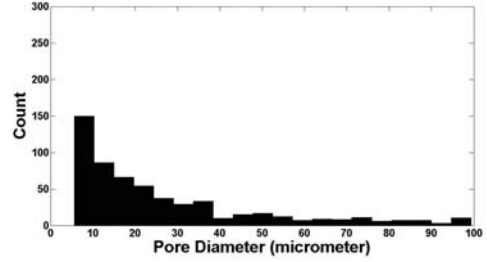
(c) Untreated GDL, TGP\_060, (190 $\mu$ m)



(d) Treated GDL, TGP\_060, (190 $\mu$ m)



(e) Untreated GDL, TGP\_090, (280 $\mu$ m)



(f) Treated GDL, TGP\_090, (280 $\mu$ m)

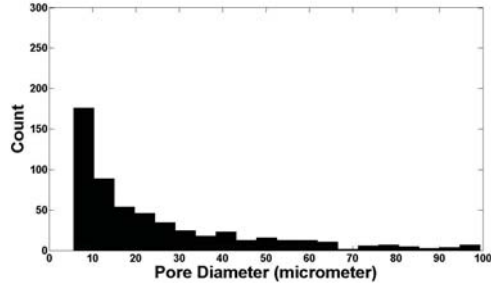
Figure 2.5: Pore diameter distribution for GDLs of different thicknesses

in all three locations.

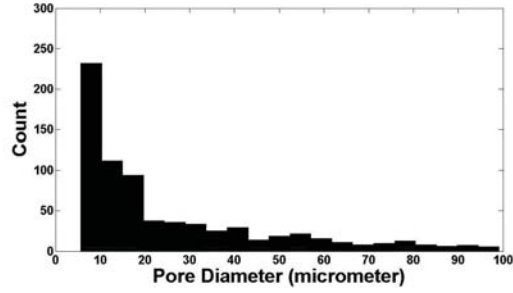
### 2.4.5 Pore Roundness Distribution

Pore roundness,  $S$ , is a property that describes the shape of the pores and is defined by Eqn. 2.5:

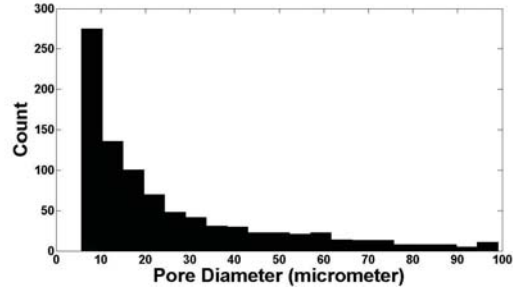
$$S = 4\pi A/P^2 \quad (2.5)$$



(a) location 1, mean pore diameter  $25.3\mu\text{m}$



(b) location 2, mean pore diameter  $25.7\mu\text{m}$

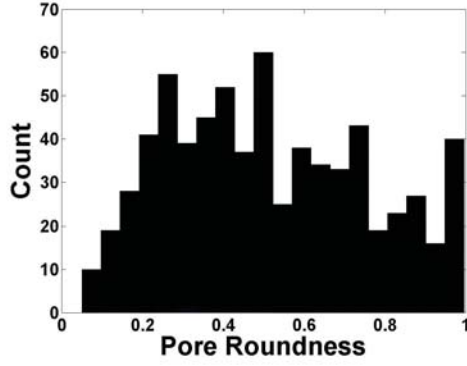


(c) location 3, mean pore diameter  $25.35\mu\text{m}$

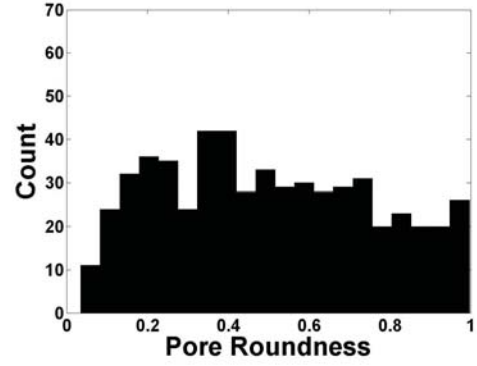
Figure 2.6: Pore diameter distribution for three random locations on untreated TGP\_120

where  $A$  is the pore area and  $P$  is the perimeter of the pore. For a perfect circle, pore roundness is 1 and as the roundness of the shape decreases, this value also decrease. Pore roundness distribution of GDLs with different thicknesses are given in Figure 7. In general, no specific trend can be detected based on these histograms. It may be concluded that Toray carbon paper pores are mostly in random shape and don't

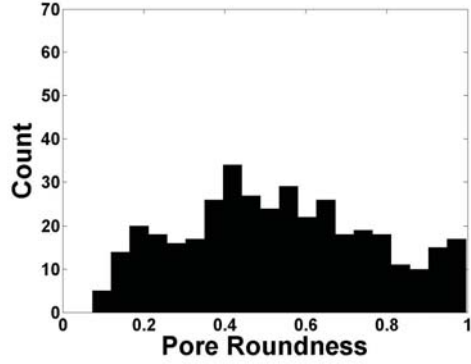
follow any specific trend of a shape.



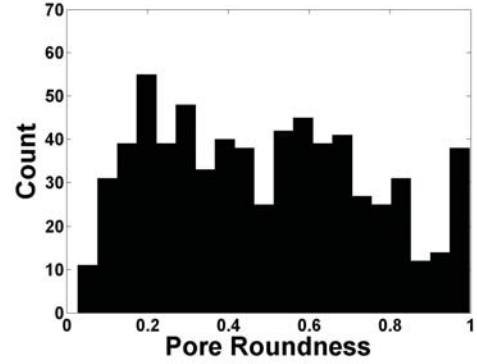
(a) Untreated GDL, TGP\_030, (110 $\mu$ m)



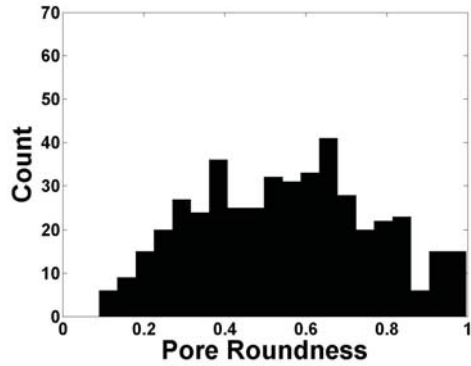
(b) Treated GDL, TGP\_030, (110 $\mu$ m)



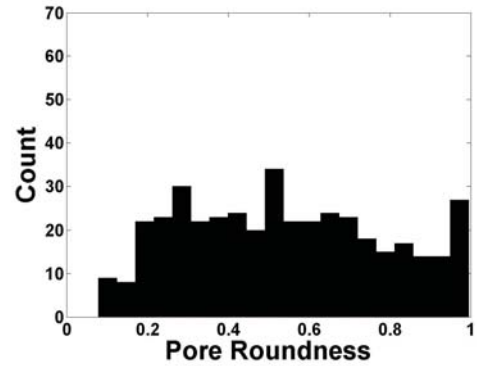
(c) Untreated GDL, TGP\_060, (190 $\mu$ m)



(d) Treated GDL, TGP\_060, (190 $\mu$ m)



(e) Untreated GDL, TGP\_090, (280 $\mu$ m)



(f) Treated GDL, TGP\_090, (280 $\mu$ m)

Figure 2.7: Pore roundness distribution of GDLs

### 2.4.6 Effect of Threshold on Mean Pore Diameter

The MATLAB code processes the SEM images by converting gray level images into binary based on Otsu method. Threshold changes the degree of black and white objects in the image and can change the results obtained from images. In this section the effect of threshold setting on the mean pore diameter is studied. Figure 8 shows the variation of mean pore diameter as a function of threshold for TGP\_060 GDL. The threshold defined based on Otsu method for this image was 0.3875. MATLAB code was ran to obtain the mean pore diameter for different thresholds starting from 0.35 with steps of 0.0125. Figure 8 shows negligible variation of mean pore diameter for different threshold settings. This strengthens the validity of the results obtained based on this approach.

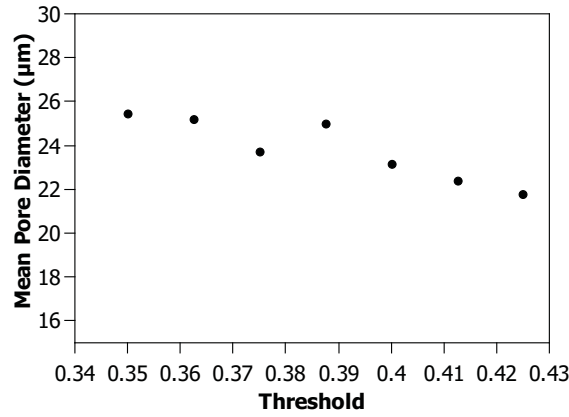


Figure 2.8: The variation of calculated mean pore diameter as a function of threshold for TGP\_060

## 2.5 Conclusion

GDL microstructural surface properties for different GDL thicknesses and for PTFE treated and untreated cases have been studied based on SEM images obtained. Con-

sequent steps of image processing have been taken and SEM images were analyzed for mean pore diameter, pore diameter distribution and pore roundness as microstructural properties of the GDL. Droplet static contact angle on GDLs, as a macroscale surface property, has been measured using a setup made for this purpose. The following conclusions can be drawn from this study:

1. GDL thickness was observed to have no effect on droplet contact angle.
2. While droplet contact angles significantly increased from an untreated GDL to a PTFE treated one, the amount of PTFE content in GDL was observed to have no impact on the contact angles measured.
3. GDL mean pore diameter does not change with its thickness. Furthermore, mean pore diameter was observed to be the same for untreated and treated GDLs. Using SEM image, the mean pore diameter was analyzed to be around  $26\mu\text{m}$  for treated and untreated Toray carbon papers of different thicknesses used.
4. The standard deviation of the mean pore diameter calculated for untreated GDLs were smaller than for untreated GDLs.
5. The PTFE loading approach taken in this study resulted in an uneven PTFE distribution on GDL surface (in-plane).
6. Threshold value in the range of the threshold defined by Otsu method was observed to have negligible effect on mean pore diameter.
7. Pore diameter distribution plots indicate that the majority of pores fall within less than  $20\mu\text{m}$  pore diameter.



8. Pore roundness distribution plots suggest a non attributable shape of Toray carbon paper pores.

## Chapter 3

# Liquid water breakthrough pressure through gas diffusion layer of proton exchange membrane fuel cell

1

### 3.1 abstract

The dynamic behavior of liquid water transport through the gas diffusion layer (GDL) of the proton exchange membrane fuel cell is studied with an ex-situ approach. The liquid water breakthrough pressure is measured in the region between the capillary fingering and the stable displacement on the drainage phase diagram. The variables studied are GDL thickness, PTFE/Nafion content within the GDL, GDL compression, the inclusion of a micro-porous layer (MPL), and different water flow rates through the GDL. The liquid water breakthrough pressure is observed to increase with GDL

---

<sup>1</sup>The contents of this chapter has been published by International Journal of Hydrogen Energy, 2014, Vol. 39, 9409-9419

thickness, GDL compression, and inclusion of the MPL. Furthermore, it has been observed that applying some amount of PTFE to an untreated GDL increases the breakthrough pressure but increasing the amount of PTFE content within the GDL shows minimal impact on the breakthrough pressure.

## 3.2 Introduction

Proton exchange membrane (PEM) fuel cells have gained much attention over the last few decades as a promising power source for automotive, portable, and stationary applications (59). As a PEM fuel cell operates, hydrogen is oxidized in the anode and oxygen is reduced in the cathode to produce electricity, the intended product, with water and heat as byproducts. While some amount of the produced water can enhance the performance of the cell by hydrating its membrane, an excess amount of liquid water can threaten a continuous performance of the cell by filling the open pores of the gas diffusion layer (GDL). The GDL serves different roles in a PEM fuel cell. It enhances electrical contacts between the catalyst layer and the bipolar plate, supports the thin and fragile electrolyte membrane from mechanical damage, diffuses reactants over the catalyst layer, and facilitates water transport from the catalyst layer to the gas channel. Saturation of the GDL pores with liquid water is referred to as GDL flooding. GDL flooding blocks the transport of the reactants to the catalyst layer and lowers the performance of the cell by causing reactant starvation. The accumulation of excess water within the gas channel can also deteriorate the performance of the cell by narrowing the flow cross sectional area within the flow channel. This phenomenon is referred to as gas channel flooding and similar to GDL flooding, it can substantially deteriorate the performance of the cell. A steady performance of the cell relies on an appropriate balance between the water produced and water removed from the catalyst

layer. This can be achieved by acquiring an accurate insight into the water transport phenomena across the electrode and GDL. Some studies reviewed water transport in PEM fuel cell and its balance within the membrane (24, 25). Water transport on the surface of the GDL has been previously studied by many researchers, including Mortazavi and Tajiri (60). The current work focuses on the liquid water transport through the porous GDL.

Water transport through the porous media in fuel cells has been studied in some works. Different models have been proposed to describe the microscale liquid water transport through the GDL and micro-porous layer (MPL). Nam and Kaviani (35) studied the distribution of condensed water within the GDL and suggested that the liquid water transports from the catalyst layer to the gas channel in a branching-type geometry. According to their model, water transports through the GDL via capillary motion in a large main stream that is extended from the catalyst layer to the gas channel. The main water path is fed by smaller streams of liquid water that transport condensed micro-droplets to macro-droplets. This model has been confirmed by Pasaogullari and Wang (34) when they took a one-dimensional analytical solution of water transport phenomena within the GDL. Park et al. (33) argued that liquid shear force and water evaporation are the dominant driving forces that transport liquid water within the GDL. Litster et al. (36) suggested that the water transport through the GDL occurs by fingering and channeling. According to their hypothesis, water recedes when a dead end occurs and flows into adjacent breakthrough channels.

Similar to the GDL, water transport through the MPL has been speculated with a wide variety of hypotheses. While some studies conclude that coating a GDL with an MPL facilitates water transport from the catalyst layer to the GDL because of the pore size gradient (35, 61, 62), a completely opposite conclusion can also be found in literature (33). Similarly, while some studies report that the cathode MPL enhances

the back diffusion of water from the cathode to anode (27, 32, 63), others argue that the MPL has no particular impact on the back diffusion of water (64–67).

These controversial hypotheses emphasize the need for further studies of water transport through the GDL and MPL. A correct understanding about the liquid water transport mechanism through these components can lead to proper water removal from inside the cell. It should be added that the unique wettability and microstructural properties of each layer adds to the complication of this study.

As a common practice, GDLs are usually treated with a hydrophobic agent such as polytetrafluoroethylene (PTFE). The hydrophobic nature of the PTFE particles facilitates water removal from the GDL to the gas channel (49). It also keeps liquid water from reentering the GDL after being expelled (36, 68). Furthermore, it has been reported that adding PTFE to GDL enhances both the gas and water transport for a cell working under flooding conditions while an excessive amount of PTFE content can lead to serious flooding in the catalyst layer (32).

In this work, liquid water transport through the porous structure of the GDL is experimentally studied by measuring the liquid water breakthrough pressure. The breakthrough pressure is defined as the pressure at which liquid water passes through the GDL and emerges from the surface. The liquid water breakthrough pressure is measured for different GDL thicknesses and different PTFE contents within the GDL. The effect of GDL thickness on liquid water transport through the GDL is also studied by reconstructing the pore-network of the GDL based on the GDL microstructural properties. Moreover, the effect of MPL and GDL compression on liquid water breakthrough pressure is investigated.

## 3.3 Experimental setup

### 3.3.1 Water breakthrough experiment

Liquid water breakthrough pressures through the GDL samples were measured with an ex-situ setup, as shown schematically in Figure 4.3. Water was injected to the surface of the GDL through a  $250\mu\text{m}$  diameter (Upchurch-U111) stainless steel capillary that has been attached to a 1/16inch FEP tube coming from a syringe pump. A differential pressure transducer (Omega, PX163\_120D5V) recorded the liquid water pressure at a sampling frequency of 50Hz. Prior to measuring the liquid water pressure in the experiments, the pressure transducer has been calibrated with a water column for accurate precision. The GDL samples were cut into pieces of  $2\text{cm} \times 1\text{cm}$  and sandwiched between two polycarbonate plates. Ten 1/8 inch screws tightened the whole setup. Teflon sheets with different thicknesses corresponding to the GDL thickness have been used to seal the whole assembly. Their thicknesses were chosen in such a way that the ratio of the GDL thickness to the Teflon sheet thickness was constant. A 5mm diameter through-all hole was machined on one polycarbonate plate (emergence side) to facilitate the water emergence.

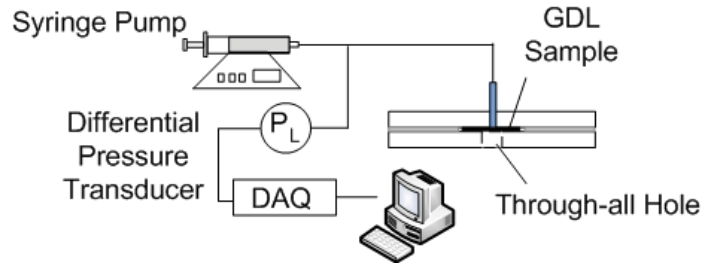


Figure 3.1: Experimental setup

In general, fluid intrusion into a porous media can cause three different flow behaviors depending on the viscosity and the flow rate of the fluids involved. Figure 3.2 shows these three flow regimes on a phase diagram that has been proposed by Lenormand

(69, 70). This chart, which is known as the Drainage Phase Diagram, is based on two nondimensional parameters of the capillary number,  $Ca$ , and the viscosity ratio,  $M$ :

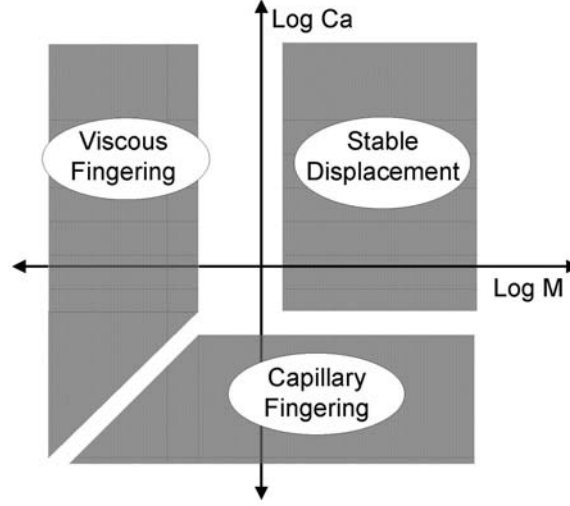


Figure 3.2: Drainage phase diagram

$$Ca = \frac{v\mu_{nw}}{\sigma} \quad (3.1)$$

$$M = \frac{\mu_{nw}}{\mu_w} \quad (3.2)$$

where  $v$  is the nonwetting fluid velocity,  $\mu_w$  and  $\mu_{nw}$  are the wetting and nonwetting fluid viscosities, and  $\sigma$  is the surface tension.

Viscous fingering occurs at low viscosity ratios and has been characterized as irregular conduits or fingers of the intruding fluid through the porous structure. The transition between capillary fingering to stable displacement may cause flooding, but the transition between stable displacement and viscous fingering rarely occurs in a fuel cell (71).

Table 1 lists water flow rates used in this study. It also includes the capillary number, viscosity ratio and the Reynolds number associated with each flow rate. The Reynolds

number is obtained by using the superficial water velocity and a mean pore diameter of  $26\mu\text{m}$  for the GDL (1). The superficial water velocity is defined as the bulk velocity of water passing within the capillary cross sectional area. The low Reynolds numbers in Table 1 indicate that viscous effects are more dominant than inertia effects. Figure 3.3 shows the range of water flow rates in the current study overlaid on the drainage phase diagram.

Table 3.1: Water flow rate considered in this study

Intruded/displaced	Water Flow Rate ( $\mu\text{lh}^{-1}$ )	M	Ca	Re
Water/air	75	64	$6.81 \times 10^{-6}$	0.0095
Water/air	150	64	$1.36 \times 10^{-5}$	0.0191
Water/air	350	64	$3.17 \times 10^{-5}$	0.0444
Water/air	500	64	$4.54 \times 10^{-5}$	0.0635
Water/air	650	64	$5.90 \times 10^{-5}$	0.0826
Water/air	850	64	$7.71 \times 10^{-5}$	0.1080

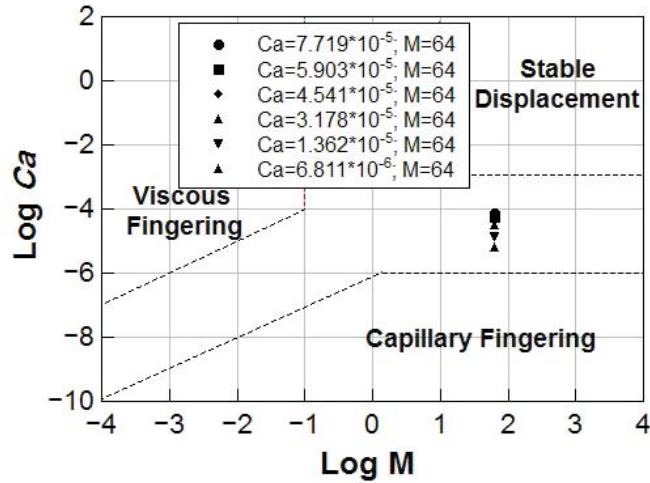


Figure 3.3: Experimental range shown on the drainage phase diagram. Dashed lines represent the hypothetical limits of flow regimes.



### 3.3.2 Sample preparation

Toray carbon papers with four different thicknesses and different PTFE contents have been used in this study. Table 2 lists the measured and calculated physical properties of GDL samples used. The carbon papers were treated with PTFE based on the procedure described in (38). According to this procedure, the untreated carbon papers were first dipped into the PTFE emulsion (60 wt.dispersion in H<sub>2</sub>O, ALDRICH) for 10h. The substrates were then put in a furnace at 120°C for 1h. The treating process was completed by increasing the furnace temperature to 360°C for 1h to make a uniform PTFE distribution through the GDL, as suggested in (38).

Table 3.2: Properties of GDL samples

Toray carbon paper type	Manufacturer specified thickness ( $\mu\text{m}$ )	Teflon sheet thickness ( $\mu\text{m}$ )	Nominal Teflon loading wt.%
TGP-030	110	50	$0, 10 \pm 0.9, 25 \pm 2, 37 \pm 3.1, 50 \pm 4.1$ wt. %
TGP-060	190	80	$0, 10 \pm 0.9, 25 \pm 2, 35 \pm 3, 55 \pm 4.3$ wt. %
TGP-090	280	130	$0, 10 \pm 0.9, 15 \pm 1.3, 35 \pm 3, 45 \pm 3.8$ wt. %
TGP-120	370	130+50	$0, 10 \pm 1, 15 \pm 1.2, 30 \pm 3.4$ wt. %

### 3.3.3 Contact angle measurement

Water droplet static contact angles on GDLs were measured with a house-made setup designed for this purpose (39). The procedure and theory are presented in Ref. (40). To measure the static droplet contact angles on GDL surfaces, droplets with diameters between 1mm to 3mm were introduced on the GDL surface. A CCD camera (PULNIX TM-1325CL) equipped with a long distance microscope (Infinity K2/S) was used to take images of the droplets. A light source was aligned with a series of concave lenses to provide a uniform background light based on the Köhler illumination method. The images of ten droplets were captured for each GDL sample. The images were

then analyzed with a computer code that was developed based on the Young-Laplace equation to give the droplet contact angles.

## 3.4 Results and discussion

### 3.4.1 Contact angle

The liquid water droplet contact angle on a solid surface describes the wetting ability of the surface by liquid. The contact angle depends on the interfacial energy along the three phase boundary.

Figure 3.4 shows the contact angles measured on different GDL samples. It can be observed from the figure that the contact angle remarkably changes by applying some amount of PTFE to an untreated GDL. However, the contact angle seems to be almost identical for different amounts of PTFE within the GDL. The figure also suggests that the GDL thickness does not have any particular impact on the droplet contact angle. This is in agreement with the findings reported by Whitesides and Laibinis that the droplet behavior on a solid surface is mostly governed by the wetting properties of the top few monolayers (48).

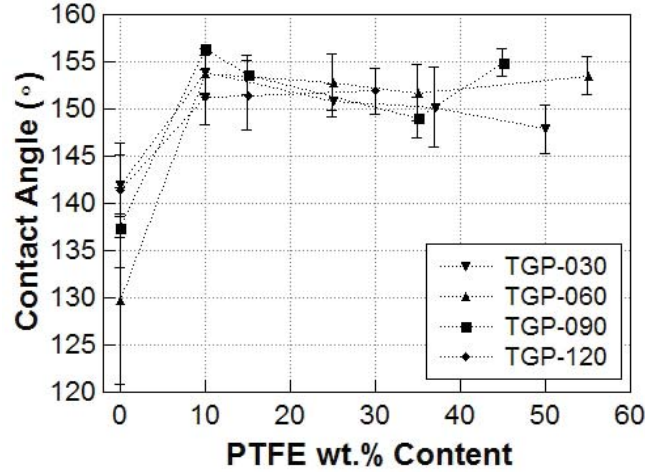


Figure 3.4: Droplets contact angles on GDL samples

### 3.4.2 Liquid water breakthrough pressure

Liquid water can pass through the GDL pores when its pressure exceeds the capillary pressure of the GDL (35). This capillary pressure is a function of pore size and can be described by the Young-Laplace equation:

$$P_c = P_g - P_l = \frac{2\sigma_{\text{water}} \cos \theta}{r_{\text{pore}}} \quad (3.3)$$

where  $P_g$  and  $P_l$  are the gas and liquid phase pressure, respectively,  $\sigma_{\text{water}}$  is the water surface tension,  $r_{\text{pore}}$  is the pore radius, and  $\theta$  is the water contact angle on the GDL. In an operating fuel cell, water is produced in the catalyst layer and accumulates behind the GDL. Water accumulation is accompanied with a pressure increase until its pressure reaches the capillary pressure of the GDL. At this pressure, water can intrude into the GDL, but it still needs to have a pressure greater than the GDL capillary pressure to be able to travel through the GDL. For water pressure greater than the GDL capillary pressure, the water flow rate through the GDL can be calculated based on Darcy's law:

$$Q = \frac{kA}{\mu} \frac{\Delta P}{\delta} \quad (3.4)$$

where  $Q$  is the water flow rate,  $k$  is the permeability,  $A$  is the cross-sectional area of the flow,  $\Delta P$  is the pressure drop through the porous media,  $\mu$  is the water viscosity, and  $\delta$  is the length that water transports through the GDL.

Figure 3.5 shows a liquid water pressure profile during the water injection at  $500\mu\ell/\text{h}$  to the surface of a 10wt.% PTFE treated TGP-120 sample. The figure shows that the pressure increases linearly since the water injection has initiated at point A. The pressure increases until it reaches 5300Pa at point B and then slightly drops down to the value of point C. It is speculated that the pressure increase from point A to

point B corresponds to water compression behind the GDL, within the capillary tube. It is also speculated that liquid water initially penetrates into the front pores of the GDL. However, low water flow rates and small length scales involved result in low Reynolds numbers. This makes viscous damping significant and meniscus does not continuously transport within the GDL (71). Consequently, pressure increases from point C up to point D where the pressure reaches the maximum value of 6270Pa. At this pressure, water was observed to emerge from the surface of the GDL and form a droplet on its surface. This peak pressure is referred to as the breakthrough pressure. The droplet emergence was followed with an immediate pressure drop to 4600Pa at point E. Figure 3.5 shows that the pressure does not drop into its initial value as it had at the beginning of the experiment. This may be due to the portion of the liquid water that has not been emerged. The remaining liquid water in the GDL forms columns with the water on the surface of the GDL (72). This causes a perpetual liquid water pressure even after droplet emergence from the surface.

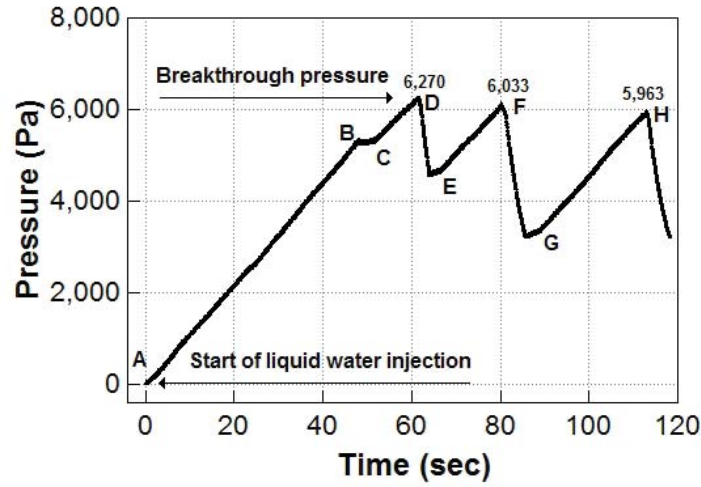


Figure 3.5: Liquid water pressure profile, water flow rate  $500\mu\text{lh}^{-1}$ , TGP-120, 10 wt.PTFE

The pressure profile has been further investigated by linear fitting between the points

marked on the figure. The calculated slopes and their corresponding coefficient of determination,  $R^2$ , are given in Table 3. The negative slope between points B and C may reflect an initial liquid water intrusion into the GDL. Furthermore, the increasing pressure slope between intervals C-D, E-F, and G-H may indicate an increasing GDL saturation over the time. This can lead to saturation of the GDL during the operation of a PEM fuel cell that ultimately ceases its performance.

Table 3.3: Linear fitting of the pressure profile between points marked on Figure 5, Pressure =  $a \times \text{time} + b$

Interval	Slope (a) ( $\text{Pa s}^{-1}$ )	Intercept (b)(Pa)	$R^2$
A-B	111.05	-42.91	0.9997
B-C	-12.74	5912.97	0.19
C-D	92.8	551.03	0.9964
E-F	102.15	-2111.53	0.9983
G-H	108.69	-6298.9	0.9991

### Effect of GDL thickness on the breakthrough pressure

GDL thickness has been reported to directly affect the overall performance of PEM fuel cells (32, 52). It also affects the water balance during the operation of the cell (73). Many efforts have been done to model liquid water transport through the porous structure of the GDL. In an early study, Benziger et al. (2) proposed that GDL can be modeled as a single layer of parallel microchannels that have different diameters. According to this model, water transports through the largest pore and with minimal pressure. This model also argues that a hydrophilic GDL makes no resistance to the liquid flow and any applied pressure can drive the liquid through the GDL. According to this model, the GDL thickness has no impact on the breakthrough pressure.

GDL can also be modeled as a network of non-uniformly distributed pores that are connected by throats (3, 74, 75). In this method, referred to as the pore-network model, it is assumed that the liquid and gas phases are stored in the pores and the volume occupied by throats is zero. Pores are assumed to have no resistance to the flow while throats resist the liquid water transport. This model suggests that the GDL thickness affects the breakthrough pressure.

In the current study, the liquid water breakthrough pressure is measured for GDLs with different thicknesses. Figure 3.6 shows the measured breakthrough pressure for untreated and Nafion loaded GDLs. The results for Nafion loaded GDLs will be discussed in Section 3.4.2. Each data point on this figure represents the mean value of three replicates and the error bars represent the calculated standard deviation. The breakthrough pressure for the untreated GDL is linearly fitted and is shown with a black line on the plot. It can be observed from the figure that the breakthrough pressure increases with the GDL thickness. This is because liquid water has to pass through a longer path in thicker GDLs.

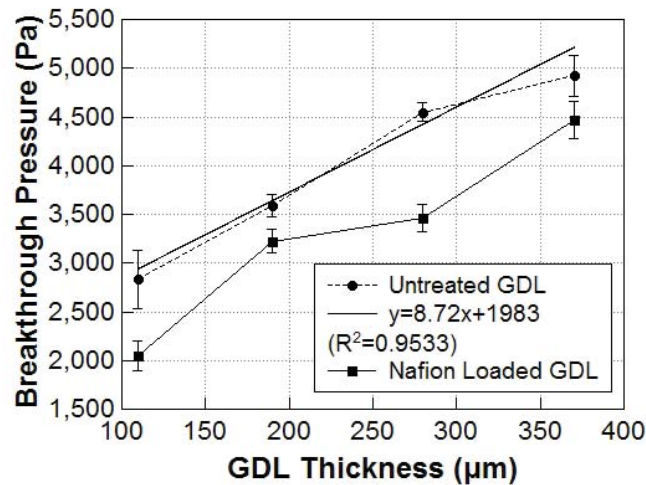


Figure 3.6: Liquid water breakthrough pressure for untreated and Nafion loaded GDLs. Water flow rate was  $500\mu\ell\text{ h}^{-1}$ .

The water transport path through the GDL can be modeled by reconstructing a pore-network of GDL. Mortazavi and Tajiri (1) studied GDL microstructural properties by analyzing SEM images of Toray carbon papers. Microstructural properties such as GDL mean pore size and pore diameter distribution have been obtained in their work. In the current study, the pore diameter distribution that has been reported in Ref. (1) is utilized to investigate the effect of GDL thickness on liquid water transport through the GDL. Liquid water follows a path with minimum capillary pressure through the GDL. This path corresponds to the largest adjacent pores that are connected by throats. To investigate the effect of GDL thickness on liquid water transport through the GDL, a random matrix that describes the random distribution of GDL pores was generated. Each array was then compared to the pore size distribution to build the matrix of GDL pore diameters. The water transport path through the GDL was defined by choosing a route that has the largest adjacent pores in the matrix. In each route, the smallest pore defines the maximum pressure that liquid water needs to have to be able to pass through the GDL. Figure 3.7 shows the smallest pore diameter in the water transport path through the GDL. It can be observed from the figure that the minimum pore diameter in water transport path decreases as the GDL thickness increases. This can be justified by the direct relationship between the GDL thickness and the number of pores that liquid water needs to pass, as shown in the inset of Figure 3.7. As GDL thickness increases, liquid water needs to pass through a greater number of pores to be able to reach the other side of the GDL. Therefore, the possibility of having smaller pores within the water transport path increases. It can be concluded from this figure that an increased GDL thickness has a two-fold impact on the liquid water breakthrough pressure. First, it increases the number of pores that liquid water needs to move through the GDL. Second, an increased number of pores in a thicker GDL makes the encounter of smaller pores within the water path



more probable. Both of these cause an increased breakthrough pressure in thicker GDLs.

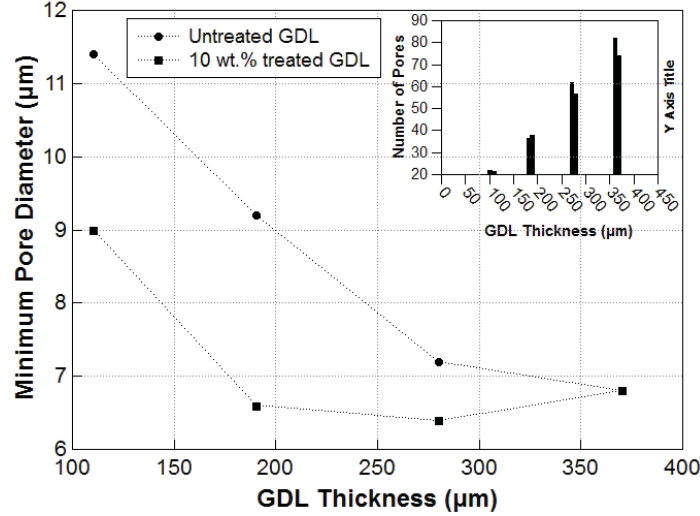


Figure 3.7: Minimum pore diameter calculated with reconstructed pore-network of GDL. GDL pore diameter distribution reported in Ref. (1) has been utilized.

### Effect of PTFE/Nafion content on the breakthrough pressure

Many works have studied the effect of the PTFE content within the GDL on the overall performance of the cell (32, 33, 56, 76–78). The common conclusion drawn from all these works suggests that the cell performance improves by adding some amount of PTFE to a raw GDL. The effect of the PTFE content on liquid water transport through the GDL has been also studied in some works (26, 27, 79). However, no common conclusion about the role of PTFE on this transport phenomenon has been obtained. While some studies conclude that water transport through the GDL decreases as the PTFE content within the GDL increases (33, 80), other studies confirm that the wetting characteristic of an untreated GDL only changes with some slight amount of PTFE (45, 49). These studies conclude that the wetting characteristic of GDLs are almost similar for different amounts of PTFE contents.

The effect of the PTFE content within the GDL on the liquid water breakthrough pressure is studied in the current work with the results shown in Figure 3.8. Each data point is the mean value of three replicates and the error bars represent the corresponding standard deviation. The figure shows that the breakthrough pressure significantly increases with the first addition of PTFE to an untreated GDL. However, the breakthrough pressure is observed to have minimal variation for higher amounts of PTFE. A similar trend was observed for contact angle variation shown in Figure 3.4. Such observations can be interpreted as the PTFE agglomeration having only limited effects on static and dynamic behavior of liquid water within the GDL. The limited effect of the PTFE content on liquid water behavior can be explained with the heterogeneous distribution of PTFE particles through the GDL. Rofaiel et al. (55) studied heterogeneous through-plane PTFE distribution in GDLs by using SEM energy dispersive X-ray spectrometry (EDS) and noticed that for carbon paper GDLs, PTFE particles mostly concentrate within the GDL and near the two surfaces. This causes a limited concentration of PTFE particles on the GDL surface with minimal impact on the contact angle for higher amounts of PTFE content.

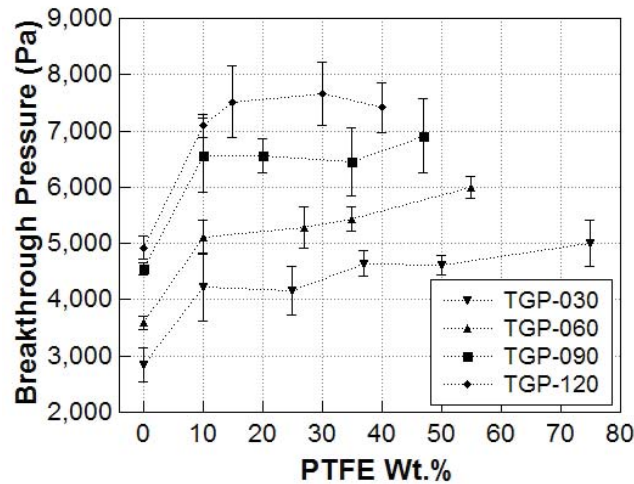


Figure 3.8: Breakthrough pressure measured for different GDLs

Figure 3.9 shows the ratio of the breakthrough pressure of PTFE treated GDLs ( $P_b$ ) to the breakthrough pressure of untreated GDLs ( $P_{(0)}$ ). The figure also includes the pressure ratios reported by Benziger et al. (2) and Tamayol and Bahrami (3). Tamayol and Bahrami (3) proposed the following pressure ratio correlation:

$$\frac{P_b}{P_{(0)}} = -0.38e^{-0.105w} + 1.38 \quad (3.5)$$

where  $w$  is the PTFE content in the GDL.

It can be observed from Figure 3.9 that the correlation given in Eqn. 3.5 does not properly match with the findings of the current study. Therefore, a new correlation was developed that can better describe the pressure ratios obtained in this study:

$$\frac{P_b}{P_{(0)}} = -0.48e^{-0.55w} + 1.48 \quad (3.6)$$

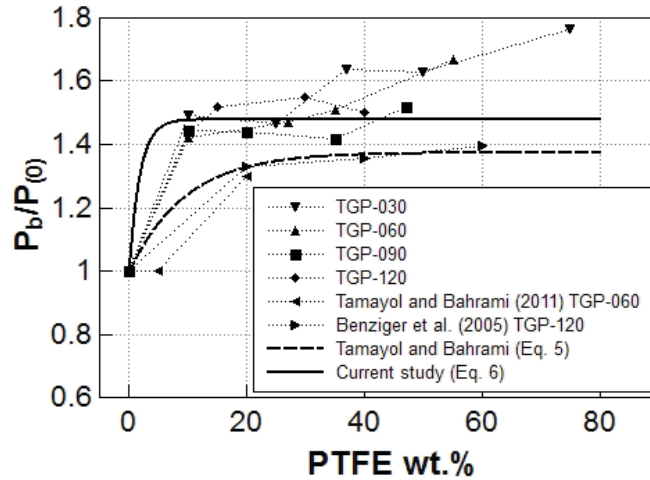


Figure 3.9: The ratio of the breakthrough pressure of treated GDLs ( $P_b$ ) to the breakthrough pressure of untreated GDL ( $P_0$ ). Water flow rate was  $500\mu\text{lh}^{-1}$ . The plot also includes the results presented in (2) and (3).

Liquid water behavior through hydrophilic GDL is also interesting. Therefore, static

and dynamic behavior of water within hydrophilic GDL is investigated in the current work. The hydrophilic GDL was obtained by treating GDL with Nafion. It has been reported that Nafion films are initially hydrophobic but show hydrophilic behavior as they absorb water (81). GDLs were loaded with Nafion based on the procedure described for PTFE loading in Section 3.3.2. Therefore, it is expected that Nafion particles penetrate into the GDL substrate and also form a layer on its surface. In this study, 17wt.% Nafion loaded GDL was used as a hydrophilic GDL.

Static contact angle measurements revealed a contact angle of  $145^{\circ} \pm 3^{\circ}$  for Nafion loaded GDLs. This contact angle was slightly greater than those droplet contact angles that have been measured on untreated GDLs. The contact angle observation in the current study can be justified by the hydrophobic nature of the Nafion film that covers the surface of the GDL. In the contact angle measurement experiment, water droplets were introduced to the surface of the sample. The droplets pinned to the GDL surface without being absorbed into it. Therefore, Nafion film showed its hydrophobic characteristic and the contact angle became greater than those angles that have been measured for untreated GDL.

The breakthrough pressure measured for Nafion loaded GDLs are shown in Figure 3.6. It can be observed that treating GDLs with Nafion decreases the breakthrough pressure compared to untreated GDLs. This can be explained by the hydrophilic characteristic of Nafion particles as they absorb water during the water injection process. The hydrophilic property of the GDL facilitates water transport through the GDL. Therefore, droplets can emerge at lower pressures compared to untreated GDLs.

## Effect of GDL compression on the breakthrough pressure

GDL compression is an important design parameter that can directly affect the performance of the fuel cell (82). It has been reported that the GDL porosity and permeability decreases by increasing the GDL compression (46, 83). The GDL compression is therefore considered to impact the liquid water transport through the porous GDL. Bazylak et al. (84) used fluorescence microscopy to study water path through the GDL and observed that liquid water tends to flow into the compressed regions of the GDL under the land. It was reported that the compressed regions of the GDL provide preferential pathways of water transport and breakthrough. Such preferential pathways and breakthrough locations correspond to the breakup of fibers and deterioration of the hydrophobic coating.

In this study, liquid water breakthrough pressure for GDLs at different compressions have been measured for TGP-090. Different GDL compressions were achieved by using Teflon sheets with different thicknesses of  $50\mu\text{m}$ ,  $80\mu\text{m}$ ,  $130\mu\text{m}$  and  $270\mu\text{m}$  around the GDL sample. It was assumed that Teflon sheets do not deform across their plane and the GDL thickness after compression becomes equal to the thickness of the Teflon sheet. Table 3.4 lists the measured breakthrough pressure for different normalized GDL thicknesses. The normalized GDL thickness was defined as:

$$\text{Normalized GDL thickness} = \frac{\text{GDL thickness after compression}}{\text{GDL thickness before compression}} \quad (3.7)$$

The GDL compression increases as the normalized GDL thickness decreases. Table 3.4 shows that the liquid water breakthrough pressure increases as GDLs become more compressed. This originates from decreased GDL porosity in higher compressions (46). Except for the normalized thickness of 0.96 that corresponds to the thickest Teflon sheet, the other three data points represent the mean value of two replicates

with uncertainties showing the standard deviation. For normalized GDL thickness of 0.96, droplet emergence was observed only in one run out of five total tests. Instead, water was observed to spread on the back side of the GDL without being emerged from the GDL surface in the other four runs. This observation suggests that a minimal GDL compression is desirable to facilitate water breakthrough.

Table 3.4: Breakthrough pressure for different GDL compressions. Water was injected at  $500\mu\ell\text{h}^{-1}$ . GDL becomes more compressed as normalized GDL thickness decreases.

Toray carbon paper type	GDL thickness ( $\mu\text{m}$ )	Teflon sheet thickness ( $\mu\text{m}$ )	Normalized GDL thickness	Breakthrough pressure (Pa)
TGP-090	280	50	0.18	$4481 \pm 24$
TGP-090	280	80	0.29	$4395 \pm 24$
TGP-090	280	130	0.46	$4239 \pm 73$
TGP-090	280	270	0.96	3670

### **Effect of MPL on the breakthrough pressure**

GDLs are usually coated with MPLs for an improved cell performance at high current densities (76, 85–87). MPLs are known to have significant effect on water balance within the cell, because they are in direct contact with the catalyst layer. In this study, liquid water breakthrough pressure of MPL coated GDLs is measured for different water flow rates. MPL coated GDLs with the GDL substrate of TGP-060 were used in two different configurations. In one configuration, the samples were used with the MPL side in contact with the water injection capillary. Water was introduced to the surface of the MPL and its emergence from the surface of the GDL was studied. In the other configuration, the samples were put in the opposite direction with water being introduced to the surface of the GDL. Although the latter configuration is not the case for PEM fuel cells, the breakthrough pressure results can be used to characterize water transport in the electrode of unitized regenerative fuel cells. This type of fuel cells combines the functionality of a fuel cell and an electrolyzer (38).

Figure 3.10 shows the measured breakthrough pressures for both of the configurations described previously. The figure also shows the breakthrough pressure for 7wt.% PTFE and untreated GDL. Each data point is the mean value of three replicates and the error bars represent the calculated standard deviation. The figure shows that the breakthrough pressure for the MPL coated GDL is greater than that for the GDL without MPL. This is because MPL acts as an additional barrier that resists water transport through the whole media. The other observation of this figure suggests that the breakthrough pressure of MPL coated GDLs depends on the configuration of MPL and GDL. The water breakthrough from the GDL surface is observed to occur at a higher pressure rather than the water breakthrough from the MPL surface.

To further investigate the effect of MPL/GDL configuration on liquid water transport,

liquid water pressure profiles for both configurations were studied, as shown in Figure 3.11. It can be observed from the figure that water pressure monotonically increases when water is being injected to the surface of the MPL. However, the pressure profile for the other MPL/GDL configuration shows a small pressure drop 22 seconds after the initiation of water injection. This small pressure drop splits the pressure profile into two separate steps. It is speculated that each step corresponds to the water transport in either layer of GDL or MPL. The first step, with the pressure increasing up to 2700Pa, represents water transport through the GDL. Similarly, the second step, with the pressure increasing from 2700Pa to 6100Pa, represents water transport through the MPL.

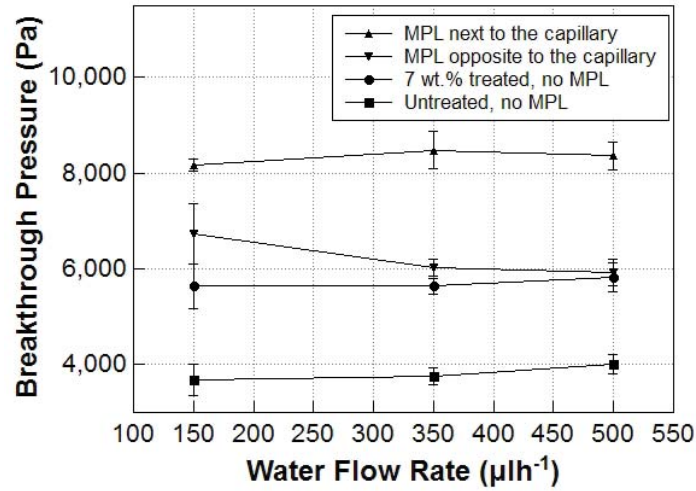


Figure 3.10: Water breakthrough pressure for different GDLs, GDL substrate TGP-060



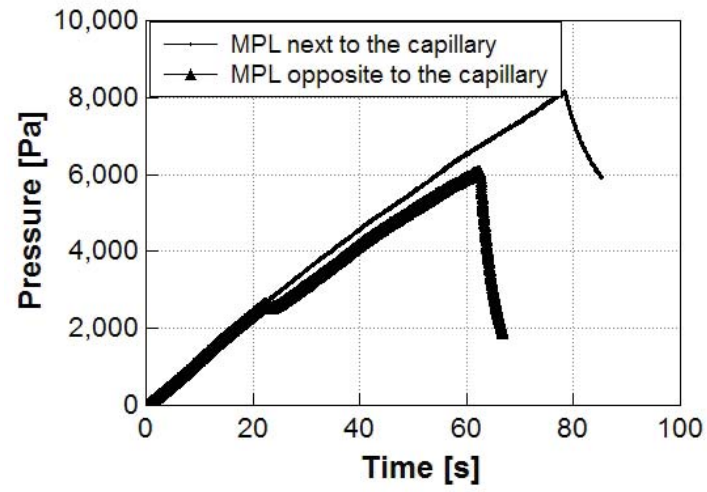


Figure 3.11: Comparison of pressure profiles for different MPL/GDL configurations at  $500\mu\ell/h$  water flow rate

### Effect of water flow rate on the breakthrough pressure

The liquid water breakthrough pressures that have been presented until now have been obtained at water flow rate of  $500\mu\ell/\text{h}$  that corresponds to the capillary number  $4.54 \times 10^{-5}$ . Because flow behavior in porous media depends on the capillary number, which itself is a function of fluid velocity (Equation 1), it may be assumed that the breakthrough pressure varies with the water flow rate. Therefore, the effect of the water flow rate on the breakthrough pressure has been studied by injecting water at different flow rates between  $75\mu\ell/\text{h}$  and  $850\mu\ell/\text{h}$ . Such flow rates correspond to capillary numbers  $6.81 \times 10^{-6}$  and  $7.71 \times 10^{-5}$ , respectively. Figure 3.12 shows the pressure profiles that have been recorded at different water flow rates. It can be observed from the figure that the breakthrough pressure shows minimal variation with water flow rate. However, water flow rate affects the pressure profile slope and the time interval that water needs to travel through the GDL to emerge from its surface. A higher water flow rate provides a higher superficial water velocity through the GDL and decreases water transport time through the GDL.

Figure 3.12 also shows that the pressure profile oscillates with a greater amplitude at lower capillary numbers. This increased oscillatory pattern of the pressure profile at lower capillary numbers originates from the low flow rate that is not capable of providing enough volume of water to keep a continuous meniscus transport (71). Therefore, water percolation through the GDL subsides. Water accumulates until the pressure exceeds the capillary pressure of the pore and can pass through the pore. As the capillary number increases, the flow regime shifts to the stable displacement and pressure oscillation decreases.

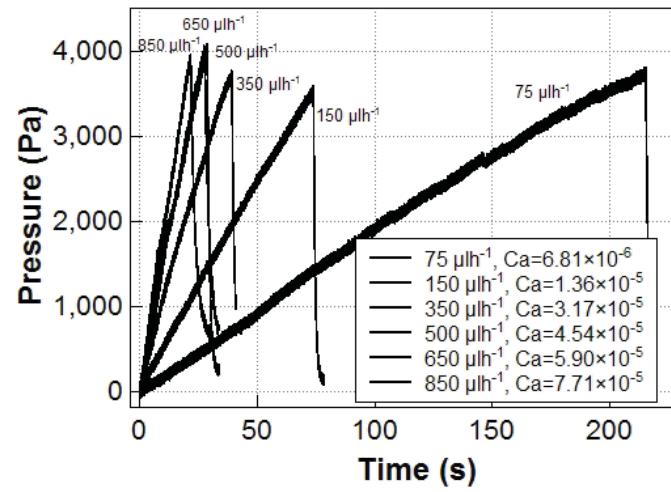


Figure 3.12: Liquid water pressure profile for different water flow rates, GDL sample untreated TGP-060

### 3.5 Conclusion

Liquid water transport through the porous structure of the GDL was studied by measuring the liquid water breakthrough pressure for different GDL conditions such as GDL thickness, PTFE content within the GDL, GDL compression, and the addition of MPL to the GDL. GDL pore size distribution reported in Ref. (1) has been utilized to reconstruct the pore-network of GDL. The following conclusions can be drawn from this study:

1. GDL thickness does not affect the droplet contact angle. This is because the droplet behavior on a solid surface is mostly governed by the wetting properties of the top few monolayers.
2. GDL thickness has a two-fold impact on the liquid water breakthrough pressure. It increases the number of pores liquid water needs to pass through the GDL to emerge from its surface. Consequently, the greater number of pores increases the probability of having smaller pores within the water transport path.
3. Applying some amount of PTFE to an untreated GDL increases the breakthrough pressure. However, the breakthrough pressure does not vary with different amounts of the PTFE within the GDL. This observation is similar to the variation of the droplet contact angle on the GDL surface.
4. It was observed that treating a GDL with Nafion increases the droplet contact angle compared to an untreated GDL. However, Nafion treatment of GDLs was observed to decrease the water breakthrough pressure. Such observations were justified according to the different characteristics of Nafion film for dry and wet conditions.

5. GDL compression was observed to increase the breakthrough pressure. This is because GDL porosity decreases as the GDL becomes more compressed.
6. The MPL coating of GDLs were observed to increase the liquid water breakthrough pressure through the GDL. It was also observed that different configurations of MPL and GDL result in different breakthrough pressures. The breakthrough pressure when MPL was in contact with the capillary tube was greater than the breakthrough pressure when GDL was in contact with the capillary tube.

## Chapter 4

# Effect of the PTFE Content in the Gas Diffusion Layer on Water Transport in Polymer Electrolyte Fuel Cells (PEFCs)

1

### 4.1 Abstract

The dynamic behavior of a liquid water droplet emerging and detaching from the surface of the gas diffusion layer (GDL) is investigated. The droplet growth and detachment are studied for different polytetrafluoroethylene (PTFE) contents within the GDL and for different superficial gas velocities flowing in the gas channel. To simulate the droplet behavior in the cathode and anode of an operating polymer electrolyte fuel cell, separate experiments

---

<sup>1</sup>The contents of this chapter has been published by Journal of Power Sources, 2014, Vol. 245, 236-244

are conducted with air and hydrogen being supplied in the gas channel, respectively. Both the superficial gas velocity and the PTFE content within the GDL are found to impact the droplet detachment diameter. Increasing the superficial gas velocity increases the drag force applied on the droplet sitting on the GDL surface. It is observed that the droplet detaches at a smaller diameter for higher superficial gas velocities. The droplets also detach at smaller diameters from GDLs with a higher amount of PTFE. Such observation is justified according to two different points of view: (1) heterogeneous through-plane PTFE distribution through the GDL and (2) reduced GDL surface roughness caused by PTFE loading.

## 4.2 Introduction

Polymer electrolyte fuel cells (PEFCs) are considered to be promising power sources for automotive, residential and stationary applications (59). They benefit from high efficiency as well as a high volumetric power density without emitting greenhouse gases as they operate. However, there are some issues that need to be solved before this type of energy system can be commercially released. One of the most challenging issues for researchers is water management in PEFCs. As electrochemical reactions occur in PEFC, hydrogen fuel is converted into useful power with water and heat as byproducts. Some portion of this produced water may be helpful in increasing the cell performance by hydrating the membrane and improving its proton conductivity. Some other portion of the water produced in the cathode may be transported into the anode by back diffusion or evaporate into the gas channel. Any excess amount of liquid water fills open pores in the gas diffusion layer (GDL). Increasing the amount of liquid water within the GDL can ultimately saturate the GDL. This will block the transport of reactants to the catalyst layer. This phenomenon is known as flooding and is reported to significantly decrease the performance of the cell (13, 34, 52).

Flooding mostly happens at high current densities when the water production rate is considerable. It may also occur at low current densities under certain conditions such as low temperature and low reactant flow rates. The accumulated liquid water within the GDL emerges from the GDL surface in the form of droplets. Liquid water removal from the GDL surface follows two different modes depending on the water production rate as well as the superficial gas velocity (5). The superficial gas velocity is defined as the bulk velocity of gas flowing within the channel cross sectional area. For a high superficial gas velocity, the shear force from the core gas flow causes the droplets to detach from the GDL surface. When the superficial gas velocity is moderate, the droplets grow in size until they touch the hydrophilic channel walls and spread over them. In this case, the capillary flow drains the liquid water through the corners and forms an annular film flow. When the water production rate is high and/or the superficial gas velocity is low, the corner flow is not capable of draining all of the liquid water from the gas channel. In this case, the liquid film grows in size and ultimately clogs the gas channel. This eventually stops the cell from producing electricity.

It is a common practice to treat GDLs with a hydrophobic agent such as polytetrafluoroethylene (PTFE) for better liquid water transport within the GDL. Many works have targeted the effect of GDL treatment on the cell performance (32, 33, 56, 76–78) as well as its effect on the liquid water behavior within the cell (26, 27, 79). Although all these works agree on improved cell performance with the addition of some amount of PTFE to the raw GDL, a common conclusion about the role of PTFE in the GDL on liquid water transport has not been reached. Some works suggest that increasing the PTFE content in the GDL lowers the liquid water transport rate through the GDL (33, 80). Some other works confirm that a GDL with a slight amount of PTFE content shows significantly lower water wetting compared to an untreated GDL but that adding more PTFE does not affect water wetting on the GDL surface (45, 49).



Although applying PTFE in the GDL mainly affects the water behavior within the cell, its impacts on other parameters should also be considered for an appropriate cell design. It has been found that increasing the PTFE content within the GDL has some drawbacks such as decreased electrical conductivity (78, 88), thermal conductivity (89), permeability (33, 78) and porosity (57, 78, 86).

Within the last few decades, different experimental approaches have been taken to study the liquid water transport and distribution in PEFCs. Methods such as neutron imaging (30, 90), gas chromatography (GC) (91, 92) and X-ray techniques (93, 94) have enabled the in-situ observation of the liquid water distribution within PEFC. The application of these in-situ observation methods is complex and expensive. Furthermore, these methods are either limited in spatial and temporal resolution (neutron radiography) or not applicable to situations with an abundant amount of liquid water (GC). Direct optical visualization, on the other hand, is most likely the simplest and the least expensive method to monitor liquid water behavior in PEFC. Depending on the optical setup used, it can also benefit from high spatial and temporal resolution. Although many studies on direct optical visualization have been conducted (5, 13, 26–28, 47), there have been very few published reports studying droplet growth and detachment on the GDL surface with different wettabilities.

Theodorakakos et al. (29) made a direct visualization experimental setup and recorded the droplet’s side view behavior upon detachment. They measured the dynamic contact angle of the droplet and could correlate the droplet detachment diameter with the air velocity. It was found that for any given droplet size, there is a critical value of superficial gas velocity above which the droplet can be detached from the surface of the GDL. Bazylak et al. (54) studied droplet growth and detachment from the GDL surface by using fluorescence microscopy and observed that the breakthrough location changes over time. This observation was followed by modeling the GDL as

an interconnected network of water pathways. The other observation reported in the same study (54) was the layer of residual water that detaching droplets leave on the GDL surface. This layer was considered to provide the pinning site for prospective droplets emerging from the GDL surface. Although this work was successful in defining the dynamic behavior of liquid water transport through the GDL, the influence of the surface energy on droplet behavior was not studied.

Kumbur et al. (47) used direct visualization and measured the contact angle hysteresis (the difference between the advancing and receding contact angles) as a parameter that determines the instability of the droplet under the influence of a shear gas flow. It was observed that the contact angle hysteresis increased with the PTFE content for any given superficial air velocity. Consequently, a droplet placed on the GDL surface of a high PTFE content tended to be more unstable and could be removed more easily. Very recently, Das et al. (72) studied droplet detachment from the GDL surface by measuring the sliding angle and noticed that liquid columns formed underneath the droplet and within the GDL pores, which assisted the droplet's adhesion to the GDL surface.

The illustrated literature review highlights the lack of in-depth studies of the droplet behavior on the GDL surface with different PTFE contents. In this work, the droplet growth and detachment from GDLs with different PTFE contents and under different superficial gas velocities are quantitatively studied. A scaled-up channel is designed to eliminate the wall effect. Although channel walls may affect the droplet growth and detachment mechanism, the droplet behavior under the influence of a core gas flow is the subject of study in this work.

## 4.3 Experimental setup

### 4.3.1 Apparatus design

An *ex-situ* direct visualization apparatus was designed and fabricated to study liquid water droplet emergence, growth and detachment on the GDL surface, as shown in Figure 1. The experimental apparatus includes a 100 mm long, 2.5 mm wide single gas channel machined on a 1 mm thick aluminum plate and sandwiched between two polycarbonate plates. Air or hydrogen was supplied within the gas channel through an inlet port machined on one of the polycarbonate plates. The inlet port was aligned with the gas channel at its entrance. The GDL sample was placed between polycarbonate plate 1 and the aluminum plate (Figure 1). Deionized liquid water was injected by a syringe pump on one side of the GDL (the side facing polycarbonate plate 1) through a capillary tube with an inside diameter of 250  $\mu\text{m}$  (U\_111, Upchurch). The droplet emergence, growth, and detachment on the other surface of the GDL were monitored through polycarbonate plate 2. Teflon sheets were used between the polycarbonate plates and the aluminum plate to prevent any possible gas leakage from the apparatus.

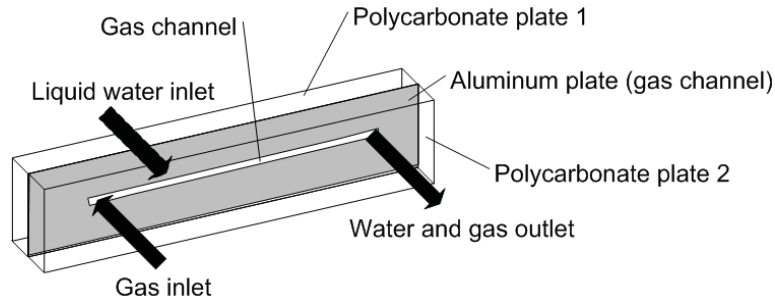


Figure 4.1: Experimental apparatus

Toray carbon papers (TGP\_060) with a manufacturer-specified thickness and porosity of 190  $\mu\text{m}$  and 76, respectively, were used as the GDL. Toray carbon papers

were loaded with PTFE based on the procedure presented in (38). This procedure is described as follows. The substrates were dipped in PTFE emulsion (60 wt. dispersion in  $H_2O$ , ALDRICH) for ten hours, and then they were dried at 120°C for one hour. According to (38), to make a uniform distribution of PTFE within the GDL substrates, the substrates were sintered at 360°C for one hour. The PTFE weight percent loaded on the GDL was controlled by the PTFE concentration in the emulsion.

To study the aging effect on the GDL surface energy, the GDL samples were aged in two steps. In the first step, the GDL samples were dipped in deionized water at 60°C for twenty-four hours. For the second step, the GDL samples were removed from the deionized water and put in the furnace at 60°C for four hours.

Figure 2 shows the amount of PTFE content in the GDL as well as the loaded GDL areal mass based on the PTFE concentration in the emulsion. The PTFE content in the GDL was calculated by comparing the GDL mass before and after the PTFE treatment. Samples with nominal PTFE loadings of 10 wt., 25 wt., 35 wt. and 55 wt. were tested in this study. Table 4.1 summarizes the measured and calculated physical properties of the samples.

Table 4.1: GDL properties for different PTFE loading

Nominal Teflon Loading	Static Contact Angle Measured (Fresh)	Static Contact Angle Measured (Aged)	Areal Mass $mg\ cm^{-2}$	Calculated Teflon Loading
0 wt.	$129.7^\circ \pm 8.84^\circ$	NA	$9 \pm 0.2$	NA
10 wt.	$153.7^\circ \pm 1.57^\circ$	$147.3^\circ \pm 1.49^\circ$	$10 \pm 0.3$	11 wt.
25 wt.	$152.8^\circ \pm 3.1^\circ$	$148^\circ \pm 3.27^\circ$	$11.5 \pm 0.3$	27 wt.
35 wt.	$151.7^\circ \pm 3^\circ$	$147.3^\circ \pm 3.27^\circ$	$12 \pm 0.5$	33 wt.
55 wt.	$153.5^\circ \pm 1.7^\circ$	$146.9^\circ \pm 2.49^\circ$	$14.5 \pm 0.7$	55 wt.

For a better clarification of the droplet behavior on the GDL surface in the cathode

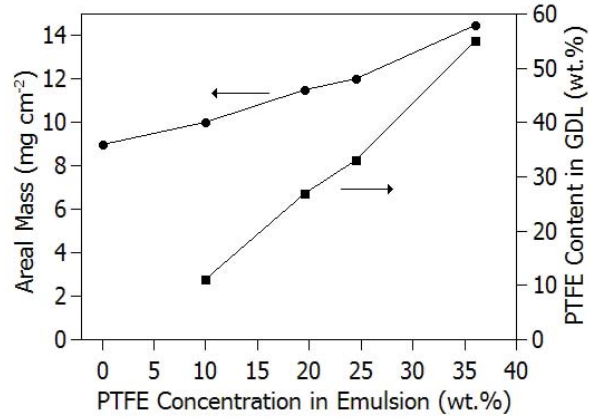


Figure 4.2: GDL areal mass and PTFE content based on PTFE concentration in emulsion

and anode of an actual fuel cell, separate experiments were conducted with air and hydrogen being supplied in the channel, respectively. Two different range rotameters (Omega, FL\_3802C and FL\_3804ST) were used to supply the desired volumetric gas flow rate at low (max.  $1200 \text{ ml min}^{-1}$  for air and  $4200 \text{ ml min}^{-1}$  for hydrogen) and high (max.  $4500 \text{ ml min}^{-1}$  for air and  $16000 \text{ ml min}^{-1}$  for hydrogen) ranges. All experiments were run in atmospheric pressure and at room temperature. The GDL surface temperature was measured as  $59^{\circ}\text{C} \pm 1^{\circ}\text{C}$  using a hand-held infrared thermometer (Optex). This relatively high temperature came from two light sources used during the experiments. Table 4.2 lists the conditions of each run in the series of experiments. Three runs were conducted for each case to ensure repeatability. To provide the same condition for each run, the GDLs were dried by purging nitrogen at  $3000 \text{ ml min}^{-1}$  for 20 minutes while the two light sources were kept on. The schematic of the experimental setup consisting of the experimental apparatus, gas cylinder, rotameter, syringe pump and high speed camera controlled by a PC is shown in Figure 3.

Table 4.2: Experiment conditions

Run	Nominal PTFE wt.	Gas	Flow Rate $\text{ml min}^{-1}$	Superficial Gas Velocity $\text{m s}^{-1}$	Reynolds Number	Water Injection Rate $\mu\text{l h}^{-1}$	Video Frame Rate (fps)
A1	0	Air	1666	11.1	1009	350	200
A2	10	Air	1666	11.1	1009	350	200
A3	25	Air	1666	11.1	1009	350	200
A4	35	Air	1666	11.1	1009	350	200
A5	55	Air	1666	11.1	1009	350	200
A6	0	Air	2222	14.8	1345	350	50
A7	25	Air	555	3.7	336	350	200
A8	25	Air	1111	7.4	672	350	200
A9	25	Air	2222	14.8	1345	350	150
H1	10	Hyd.	6000	40	504	350	150
H2	25	Hyd.	6000	40	504	350	150
H3	35	Hyd.	6000	40	504	350	150
H4	55	Hyd.	6000	40	504	350	150
H5	25	Hyd.	3000	20	252	350	150
H6	25	Hyd.	4000	26.6	335	350	150
H7	25	Hyd.	5000	33.3	419	350	150
H8	25	Hyd.	7000	46.6	587	350	150
H9	25	Hyd.	8000	53.5	672	350	150
H10	35	Hyd.	3000	20	252	350	150
H11	35	Hyd.	4000	26.6	335	350	150
H12	35	Hyd.	5000	33.3	419	350	150
H13	35	Hyd.	7000	46.6	587	350	150
H14	35	Hyd.	8000	53.5	672	350	150

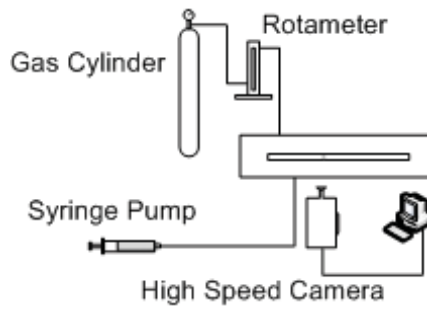


Figure 4.3: Schematic of experimental setup

### 4.3.2 High speed imaging

The droplet growth and detachment on the GDL surface in the gas channel was recorded using a high speed camera (50KD2B2, Mega Speed) controlled with a PC. A Navitron TV Zoom Lens 7000 18\_180 mm was attached to the high speed camera that provided a spatial resolution of  $10 \mu\text{m pixel}^{-1}$ . The visualizing window had a resolution of  $640 \times 480$  pixels with approximately 250 pixels for the channel width. This ensured a proper resolution for image analysis. Image analysis was performed by the Mega Speed AVI Player software provided by the camera manufacturer. Two 300-W tungsten lamps (Lowel Omni) were used as the light source to provide proper illumination.

### 4.3.3 Contact angle measurement

The static contact angles on fresh and aged GDLs were measured using a setup already made for this purpose (39). The procedure and theory can be found in (40). The contact angle measurement setup consisted of an illumination source that provided a beam of light with equal intensity, a series of lenses to converge the beam, a labjack (Thorlabs L200) enabling X\_Y\_Z alignment of the sample and a long distance microscope (Infinity K2/S) coupled to a CCD camera (PULNIX TM-1325CL). Ten droplets with diameters in the range of 1 – 3 mm were placed on the GDL surfaces, and images were captured. The images were then analyzed with a computer code developed based on the Young-Laplace equation. The mean value of the contact angle for the ten images was considered the contact angle of the droplets on each GDL surface.

#### 4.3.4 Flow condition

The surface area of the capillary tube, ( $4.908 \times 10^{-4} \text{ cm}^2$ ), used to inject liquid water on the GDL surface can be considered the water production area in an operating fuel cell. The water production rate during the oxygen reduction reaction can be obtained by Faraday's second law of electrolysis:

$$\dot{n}_{H_2O} = \frac{iA_{act}}{2F} \quad (4.1)$$

where  $\dot{n}_{H_2O}$  is the molar rate of water produced,  $i$  is the current density,  $A_{act}$  is the active area, and  $F$  is Faraday's constant. Assuming all water produced is in the liquid phase, the liquid water production rate for a current density of  $2 \text{ A cm}^{-2}$  and an active area of  $4.908 \times 10^{-4} \text{ cm}^2$  is  $0.33 \mu\ell \text{ h}^{-1}$ . To be able to run the experiment in a reasonable amount of time and without secondary effects such as evaporation, a water flow rate of  $350 \mu\ell \text{ h}^{-1}$  was chosen, as in (95).

Air and hydrogen were supplied at different ranges, as given in Table 2. These flows result in Reynolds numbers ranging from 336 to 1345 for air and from 252 to 672 for hydrogen.

### 4.4 Results and discussion

#### 4.4.1 Contact angle

The liquid contact angle is a measure of the wetting ability of a solid surface by liquid and depends on the interfacial energy along the three phase boundary. In water management with application in PEFC, the contact angle is an important parameter characterizing many dominant properties. The surface adhesion force, drag force, capillary pressure, and even the shape of a droplet sitting on the GDL surface are



some of the properties that the contact angle affects. The surface adhesion force, which is the consequence of the molecular interaction between a liquid and a solid, makes the droplet adhere to the solid surface. This force holds the droplet on the GDL surface by resisting the drag force from the core gas flow. It has been shown that the contact angle hysteresis is a key parameter in defining the adhesion force and instability of a droplet under the influence of a shear gas flow (47, 96). Increasing the gas flow rate increases the dynamic contact angle hysteresis and moves the droplet towards an unstable condition (47). The contact angle of a droplet on a PTFE-treated GDL depends on parameters such as the porosity, macroscopic roughness of fibers ridges, microscopic roughness of the individual fibers, and chemical heterogeneity of the carbon and PTFE surface in the GDL (45). In this study, the static contact angle was measured and used as the parameter defining the surface energy of GDLs.

Sessile droplets on treated and untreated GDLs are shown in Figure 4. The GDLs were aged by dipping them in deionized water at 60°C for twenty-four hours and then drying them in a furnace at 60°C for four hours. Figure 5 shows the contact angles of the droplets on fresh treated, aged treated, and fresh untreated GDLs. The error bars shown represent the standard deviation of the measured contact angles. While adding some amount of PTFE to an untreated GDL significantly increases the contact angle, it can be observed that the droplets show similar contact angles on GDLs with different PTFE contents. A similar observation was reported by Benziger et al. (2) for TGP-H-120 Toray carbon paper. Lim and Wang (56) calculated the contact angle based on a capillary meniscus height measurement and observed that the contact angle does not change significantly by adding Teflon from 10 wt. to 40 wt. PTFE. Fairweather et al. (49) used the pore size distribution obtained from MIP to estimate the effective contact angle distributions on untreated and treated GDLs. It was observed that the contact angle increases by applying 5 wt. PTFE to a raw

GDL and that any further addition of PTFE does not have any effect on the contact angle. Because the contact angle does not change with the PTFE content in the GDL, it is suspected that most of the PTFE particles penetrate through the GDL and agglomerate within the pores rather than on the GDL surface. Furthermore, the comparable contact angles of treated fresh GDLs ( $152^\circ$ ) and treated aged GDLs ( $147^\circ$ ) support the possibility of higher PTFE agglomeration within the GDL rather than on its surface. However, there should be some PTFE particles sitting on the surface of the GDL because the contact angle is significantly different between an untreated GDL and a 10 wt. PTFE-treated GDL. PTFE particles are small enough ( $50 - 500 \text{ nm}$ ) to be able to pass through GDL pores ( $10 - 30 \text{ }\mu\text{m}$ ) and accumulate on the inner layers of the GDL. The smaller standard deviations of the contact angles on the treated GDLs shown in Figure 5 represent more uniform contact angles on treated GDLs compared to untreated ones. The PTFE particles fill the open pores on the GDL surface and make a smooth surface with a shorter contact line between the droplet and fibers.

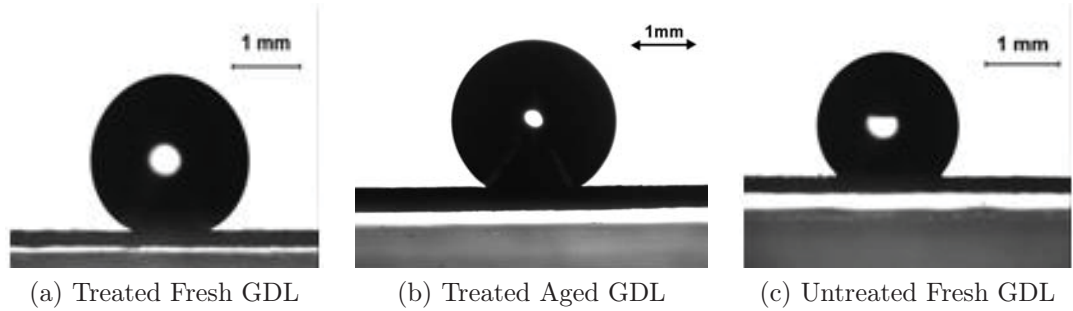


Figure 4.4: Contact angle measurement (a) 10 wt. PTFE treated fresh GDL, contact angle =  $153.7^\circ \pm 1.57^\circ$  (b) 10 wt. PTFE treated aged GDL, contact angle =  $147.3^\circ \pm 1.49^\circ$  (c) untreated fresh GDL, contact angle =  $129.7^\circ \pm 8.84^\circ$

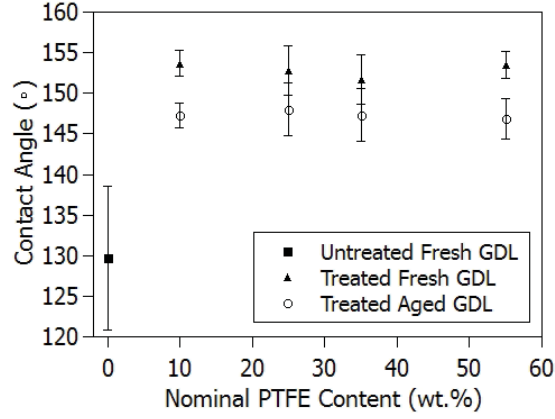


Figure 4.5: Droplet contact angle on treated and untreated GDLs

#### 4.4.2 Droplet growth

Liquid water finds the path with the least transport resistance through the GDL and emerges from preferential locations, forming droplets (84). The emerged droplet grows in size until it becomes large enough to detach from the GDL surface. However, a low superficial gas velocity is not capable of detaching the droplet. Figure 6 shows the droplet growth on untreated and treated GDLs with different PTFE contents. The spreading factor, defined as the ratio of the droplet diameter  $d$  to the droplet detachment diameter  $d_d$ , is shown at different times. The spreading factor is only shown for the first 100 ms for the sake of comparison. Figure 6 shows that as the PTFE content in the GDL increases, the slope of the spreading factor curve increases. This means that for GDLs with a higher amount of PTFE droplets need less time to reach the size at which they detach. Figure 6 also shows that for 35 wt. and 55 wt. PTFE, detachment occurs within 100 ms, while a longer time is required for droplets to detach from GDLs with a lower amount of PTFE.

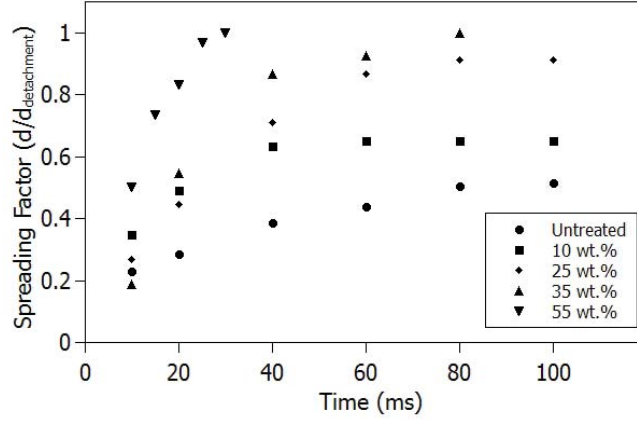


Figure 4.6: Droplet growth rate under superficial air velocity of  $11.1 \text{ m s}^{-1}$  on treated and untreated GDLs

#### 4.4.3 Droplet detachment diameter

Zhang et al. (5) defined two modes of water removal from a GDL surface, droplet detachment by shear force and capillary wicking of liquid water into more hydrophilic channel walls. Droplet detachment is the characteristic of a high superficial gas velocity, while capillary wicking occurs at lower gas flow rates. The droplet detachment from GDLs with different wettabilities is the subject of study in the present work. Droplet detachment can be studied by considering all of the forces applied on a droplet under a shear gas flow. Considering the droplet free body diagram as shown in Figure 7, these forces are (i) the gravitational force ( $F_G$ ), (ii) the surface adhesion force ( $F_S$ ) and (iii) the shear drag force from core gas flow ( $F_D$ ).

The Bond number describes the ratio of the gravitational force to the surface tension force and is defined as:

$$Bo = \frac{\Delta \rho g d_d^2}{\sigma} \quad (4.2)$$

where  $\Delta \rho$  is the density difference between the liquid and the gas,  $g$  is the gravitational

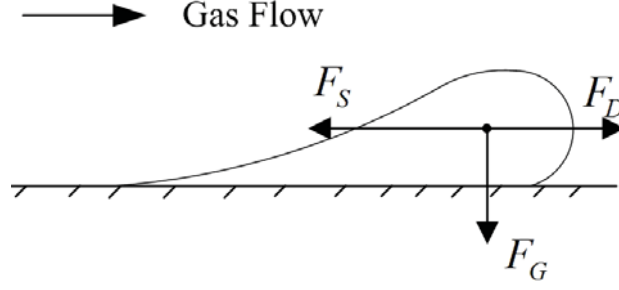


Figure 4.7: Forces applied on a droplet in general configuration

acceleration,  $d_d$  is the droplet detachment diameter and  $\sigma$  the interfacial surface tension. The maximum Bond number calculated in this study was 0.1, which indicates that the force of gravity is small compared to the surface tension and can be neglected (97). The surface adhesion force keeps the droplet on the surface, while the drag force applied from the core gas flow tries to detach the droplet from the surface. Droplet detachment occurs when the drag force overcomes the surface adhesion force.

The droplet detachment diameter is an important parameter in fuel cell gas channel design. A gas channel smaller than the droplet size will be clogged by the droplet upon detachment. An over-sized channel, on the other hand, will increase the parasitic power required to supply the reactants at the same superficial velocity to run the cell. The former stops the cell from producing energy, and the latter lowers the overall energy efficiency.

Comparing the hydrogen and air superficial velocities upon droplet detachment shows that a higher hydrogen velocity is required to detach a droplet from the GDL surface. This behavior can be justified by hydrogen's lower density compared to air. The drag force is a function of the gas velocity and the gas density. Because hydrogen density is lower than air density, a higher superficial hydrogen velocity will be required to provide enough drag force to detach a droplet. The drag force applied from a core gas flow on a droplet can be calculated by:

$$F_D = \frac{1}{2}\rho C_D A_P V^2 \quad (4.3)$$

where  $\rho$  is the gas density,  $C_D$  is the drag coefficient,  $A_P$  is the projected area, and  $V$  is the superficial gas velocity.

It was also observed that droplets leave residual liquid water particles as they detach from the GDL surface. It has been reported that these residual water particles become the pinning site for future droplets and are followed by slug formation after a while (54).

The location of the droplet's emergence was also studied in this work. It was observed that the first few droplets emerged and detached at a constant location. However, prospective droplets showed a tendency to appear from different locations, as shown in Figure 8. This suggests an interconnected network of water pathways within the GDL, as was reported by Bazylak et al. (54).

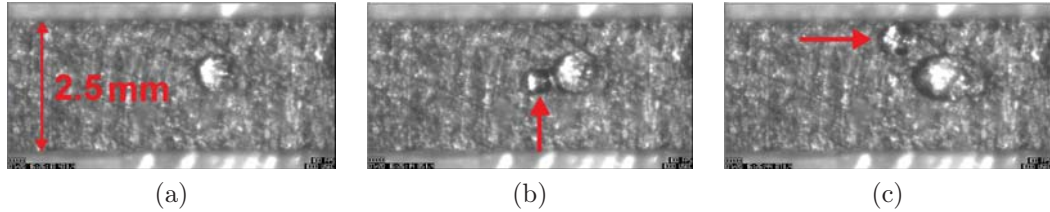


Figure 4.8: Multiple droplets emerging at different breakthrough locations on 10 wt. PTFE GDL surface; (a) breakthrough location for first few droplets (b, c) droplets emerging at different locations after a while

### Effects of the PTFE content on the droplet detachment diameter in the cathode and anode

Figure 9 shows the droplet detachment diameter on GDLs with different PTFE contents and under a superficial air velocity of  $11.1 \text{ m s}^{-1}$ . Each data point represents

the mean diameter of the first ten detaching droplets for three separate runs. As the figure shows, the droplet detachment diameter decreases as the PTFE content within the GDL increases. As shown in Figure 5, the droplet contact angles on the PTFE-treated GDLs are almost uniform and do not change with the PTFE content. The fact that the PTFE content within the GDL affects the droplet detachment diameter without having any contribution to the droplet surface contact angle can be an indication of the existence of a heterogeneous through-plane parameter affecting the liquid water transport within the GDL.

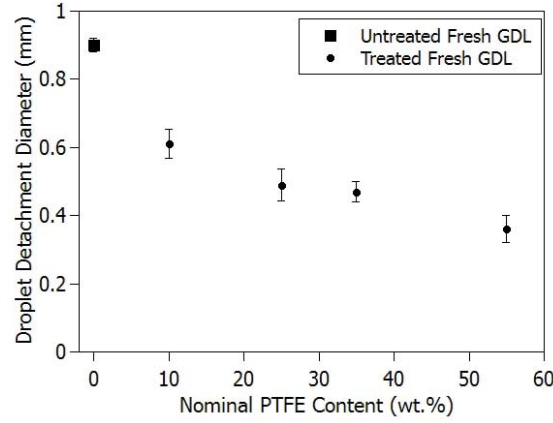


Figure 4.9: Droplet detachment diameter under  $11.1 \text{ m s}^{-1}$  superficial air velocity and at different PTFE wt.for treated GDL. Sliding diameter is considered for untreated GDL (runs A1-A5 in Table 5.1).

A smaller detachment diameter on GDLs with a higher PTFE content can be justified by PTFE accumulation within the GDL. It has been reported that the PTFE distribution through the GDL is not uniform and varies through the GDL thickness. Fishman and Bazylak (57) used high resolution microscale visualization and measured the through-plane porosity of PTFE-treated GDLs. Studying the GDL through-plane porosity, a higher local porosity in the center of the GDL and a lower local porosity near the surface were observed. This observation was attributed to

a higher PTFE concentration near the surface and a lower PTFE concentration in the core region of the GDL. In another study, Rofaiel et al. (55) used scanning electron microscopy (SEM) energy dispersive X-ray to measure the through-plane PTFE distribution within the GDL. They reported a higher PTFE concentration near the surfaces and a lower PTFE concentration in the core region of the GDL. Both studies agree on the heterogeneous through-plane PTFE distribution within the GDL. This uneven profile of the PTFE distribution can be a reason for the different droplet detachment diameters for different PTFE contents. Agglomerated PTFE particles through the GDL increase the internal contact angle  $\theta$  and decrease the pore radius  $r_{pore}$  of the GDL. Such changes result in an increase in the capillary pressure required to intrude liquid water into the pores:

$$P_c = \frac{2\sigma_{\text{water}} \cos \theta}{r_{\text{pore}}} \quad (4.4)$$

Liquid water can pass through the pores only when its pressure exceeds the capillary pressure, and for a continuous flow to happen, its pressure should remain higher than the capillary pressure (35). Carbon layers with high amounts of PTFE content within the GDL resist liquid water transport by acting as a barrier. Low pressure liquid water is not capable of passing through this barrier and accumulates behind the GDL with increasing pressure. The liquid water pressure increases until it reaches the capillary pressure and can pass through the pores. As liquid water passes through the pores, its pressure suddenly drops, and the barrier again blocks water transport through the GDL. The liquid water passing through the GDL appears in the form of droplets on the GDL surface. On the other hand, because the barrier within the GDL has blocked water transport through the GDL, no water column exists underneath the droplet to assist its adhesion (72). All of these consequences result in easier droplet



detachment from the surface of the GDL.

A smaller droplet detachment diameter for GDLs with a higher amount of PTFE may also be justified based on the surface roughness. It has been reported that the droplet behavior on a GDL surface is mostly controlled by the wetting characteristic of the top few monolayers (48). A higher PTFE concentration has been reported to reduce the surface roughness (57), and because droplets show less of a tendency to detach from rough surfaces (54), it can be concluded that droplets can detach more easily from GDLs with a higher amount of PTFE.

The droplet behavior on untreated GDL surface was also studied in this work. For a treated GDL, droplets could detach from the GDL surface as discussed earlier. However, for an untreated GDL, it was observed that droplets do not detach from the surface. Instead, the emerged droplets were removed by sliding on the GDL surface to the end of the gas channel, where they were discharged through the outlet port. The droplet sliding diameter on an untreated GDL is shown in Figure 9. Figure 10 shows a droplet sliding on an untreated GDL without being detached. Fairweather et al. (49) measured the capillary pressure for untreated and treated GDLs and found that liquid water intrudes more easily into an untreated GDL, while adding a slight amount of PTFE to the GDL makes it easier to remove water and harder for the water to intrude.

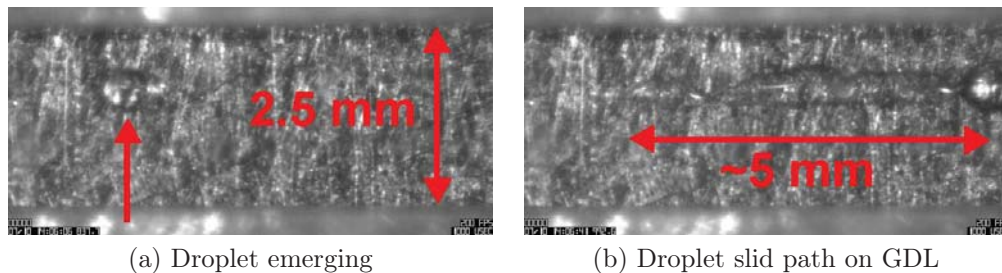


Figure 4.10: Droplet sliding on untreated GDL without detaching

The effect of GDL aging on the droplet detachment diameter was not studied in this work. However, although aging was observed to decrease the droplet contact angles (Figure 5), it was assumed that it does not have any effect on the droplet detachment diameter. The reason for this assumption can be explained by the uniform contact angles of droplets on treated aged GDLs. Droplets make similar contact angles on treated aged GDLs with different amounts of PTFE content. Because identical behavior was observed for treated fresh GDLs, it may be assumed that aging has no impact on the droplet detachment diameter.

Our results in this work show that increasing the PTFE content in the GDL enhances droplet detachment by reducing the growth time and the droplet diameter upon detachment. However, the way that the PTFE content affects other parameters should be carefully considered for an appropriate cell design. An optimum PTFE content in the GDL should be defined by considering all of the parameters affecting the cell performance. For instance, in terms of the cell performance, Velayutham et al. (98) reported that the optimum PTFE content is approximately 20 wt.. Any further amount of PTFE within the GDL increases the electrical resistance, and a lesser amount of PTFE results in water flooding within the cell. Each of these consequences can reduce the cell's performance and should be avoided.

Figure 11 shows the droplet detachment diameter under a superficial hydrogen velocity of  $40 \text{ m s}^{-1}$  and as a function of the PTFE content in the GDL. The general trend indicates that the droplet detachment diameter decreases as the PTFE content increases. However, the comparable detachment diameters for 25 wt. and 35 wt. suggest that the detachment diameter is not a strong function of the PTFE content within the GDL. A similar observation can be detected in Figure 9 when air is supplied in the gas channel.

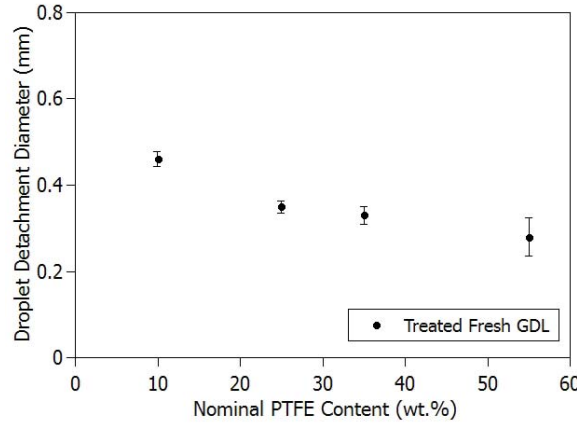


Figure 4.11: Droplet detachment diameter under  $40 \text{ m s}^{-1}$  superficial hydrogen velocity with different PTFE wt. (runs H1-H4 in Table 5.1)

### Effect of the superficial gas velocity on the droplet detachment diameter in the cathode and anode

The superficial gas velocity plays an important role in droplet detachment from the GDL surface. For a low superficial gas velocity, the drag force applied from the core gas flow (Eq. 4.3) cannot overcome the adhesion force. In this case, the droplet increases in size and forms slug. A high superficial gas velocity, on the other hand, leads to low reactant utilization, increased parasitic losses, and possibly membrane dehydration. Therefore, knowing the appropriate range of the superficial gas velocity can lead to an appropriate cell design in terms of liquid water drainage and the overall cell efficiency. Figure 12 shows the droplet detachment diameter for different superficial air velocities. As the superficial air velocity increases, the droplets detach at smaller diameters on the treated GDL surface. For an untreated GDL, increasing the superficial air velocity decreases the droplet sliding diameter. It was observed that for low superficial air velocities ( $3.7 \text{ m s}^{-1}$  and  $7.4 \text{ m s}^{-1}$ ), droplets were not sliding on untreated GDLs. Instead, they grew in size and turned into slugs.

Figure 4.13 shows the droplet detachment diameter as a function of the superficial hy-

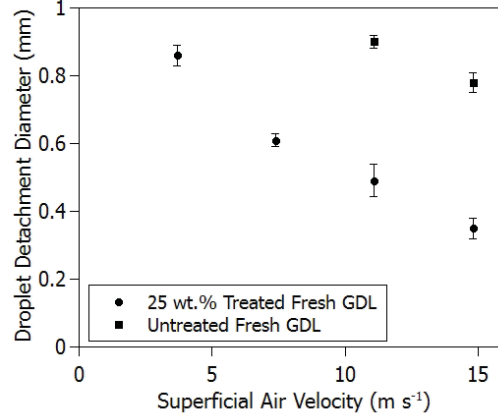


Figure 4.12: Droplet detachment diameter under different superficial air velocities and 25 wt.PTFE treated and untreated GDL (runs A1, A3, A6-A8 and A9)

drogen velocity. The general trend is that the droplet detachment diameter decreases as the superficial hydrogen velocity increases. The droplet detachment diameter for two different PTFE contents (25 wt. and 35 wt.) are plotted in this figure. For a low to moderate superficial hydrogen velocity ( $20 \text{ m s}^{-1}$  -  $33.3 \text{ m s}^{-1}$ ), the droplet detachment diameter is lower for 35 wt., while for a higher superficial hydrogen velocity ( $40 \text{ m s}^{-1}$  -  $53.3 \text{ m s}^{-1}$ ), the droplets detach at comparable diameters from the GDLs. This behavior indicates that for a high superficial gas velocity, the PTFE content in a GDL is not the governing parameter in droplet detachment.

In reality, the hydrogen velocity in the anode tends to be low because pure hydrogen is used and utilization is very high. Therefore, once droplets form in the anode gas channel, it is extremely difficult to remove such droplets by the drag force.

#### **Comparing the sensitivity of the PTFE content in a GDL and the superficial gas velocity on the droplet detachment diameter**

The droplet growth and detachment from a treated fresh GDL under the influence of a shear gas flow is studied. Although increasing both the PTFE content in the

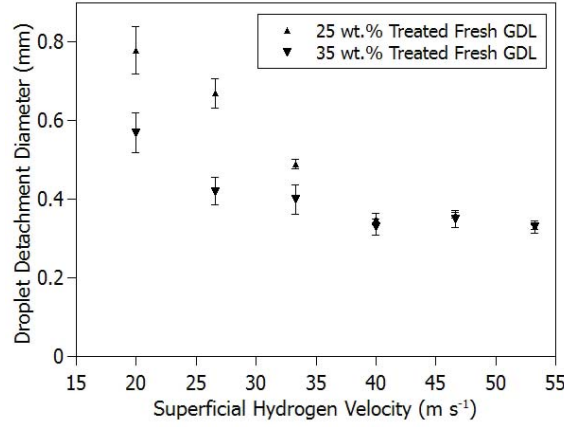


Figure 4.13: Droplet detachment diameter for different hydrogen superficial velocity in gas channel (runs H2, H3, H5-H14)

GDL and the superficial gas velocity in the gas channel were observed to decrease the droplet detachment diameter, the latter was found to have more of an impact on the size of the droplet upon detachment. As the superficial air velocity increased from  $3.7 \text{ m s}^{-1}$  to  $14.8 \text{ m s}^{-1}$ , the droplet detachment diameter decreased from 0.86 mm to 0.35 mm for a 25 wt. treated GDL (Figure 12). However, for a constant superficial air velocity of  $11.1 \text{ m s}^{-1}$ , increasing the PTFE content within the GDL from 10 wt. to 55 wt. resulted in a droplet detachment diameter reduction from 0.61 mm to 0.36 mm (Figure 9). These results show that between the PTFE content within the GDL and the superficial gas velocity flowing in gas channel, the superficial gas velocity is a sensitive parameter that affects the droplet detachment diameter. The droplet growth and removal from untreated GDL is also investigated. Despite treated GDLs where droplets could detach from the GDL surfaces, the droplet removal from an untreated GDL surface was in the form of droplet sliding. For a high superficial air velocity, the core gas flow was capable of sliding the droplet on the GDL surface, while for a low air flow rate, the droplets increased in size and turned into slugs (Figure 12).

## 4.5 Conclusion

The water droplet emergence, growth, and detachment on GDLs with different PTFE contents are studied under different superficial gas velocities. To simulate droplet behavior in the anode and cathode of an operating PEFC, hydrogen and air were supplied, respectively, within the gas channel. The following conclusions can be drawn from this study:

1. Applying PTFE on a raw GDL increases the contact angle significantly, but the contact angle does not change for different PTFE contents. Furthermore, droplets show much more uniform contact angles on treated GDLs compared to untreated ones. As GDLs are loaded with PTFE, PTFE particles fill the GDL pores and make the GDL surfaces more uniform with shorter contact lines between the droplet and fibers.
2. Droplets show slightly lower contact angles on treated aged GDLs compared to fresh ones. This is an indication of PTFE degradation from the GDL surface. However, because the average contact angle measured on treated fresh GDLs ( $\sim 152^\circ$ ) and treated aged GDLs ( $\sim 148^\circ$ ) are almost similar, it is assumed that GDL aging does not have any effect on the droplet detachment diameter.
3. The droplet detachment diameter decreases as the PTFE content in the GDL increases. A high PTFE content within the GDL increases the capillary pressure liquid water needs to exceed to be able to pass through the GDL pores. The increased liquid water pressure provides the liquid a path through the pores, but as liquid water passes through the GDL, its pressure instantly drops. This results in small droplets emerging from the GDL surface without water columns underneath to assist adhesion.

A smaller droplet detachment diameter can also be obtained by a smoother GDL surface. Droplets tend to detach easily from less rough surfaces. As PTFE treating makes GDL surfaces smoother, droplets can be detached from GDLs with a higher amount of PTFE at a smaller diameter.

4. The superficial gas velocity significantly affects the droplet detachment diameter. Increasing the superficial gas velocity increases the drag force applied on the droplet. Therefore, a smaller droplet diameter is required to overcome the adhesion force keeping the droplet on the GDL surface.
5. It was observed that droplets detach at higher superficial velocities for hydrogen than for air. Hydrogen's lower density is the main reason for this effect.
6. It was observed that droplet detachment does not occur on an untreated GDL. Instead, the droplets slide on its surface all the way to the end of the gas channel. This results from the lower contact angle (higher surface energy) of the droplets on untreated GDLs.
7. For a high superficial hydrogen velocity ( $40 \text{ m s}^{-1}$  -  $53.3 \text{ m s}^{-1}$ ), the PTFE content in the GDL is not the governing parameter in defining the droplet detachment diameter. Similar detachment diameters were recorded for GDLs with two different amounts of PTFE.

# Chapter 5

## Two-phase flow pressure drop in flow channels of proton exchange membrane fuel cells-a review

1

### 5.1 abstract

Water management in proton exchange membrane (PEM) fuel cells has stimulated an extensive research on different aspects of water transport phenomena. As a PEM fuel cell operates, power is produced with water and heat as inevitable byproducts. The water produced during the operation of a PEM fuel cell results in a liquid-gas two-phase flow in flow channels. A successful PEM fuel cell design requires a comprehensive knowledge about different properties of liquid-gas two-phase flow. One such property, that has a dominant impact on the performance of a PEM fuel cell,

---

<sup>1</sup>The contents of this chapter has been submitted to Renewable and Sustainable Energy Review



is the two-phase flow pressure drop within the flow channels. This paper reviews the two-phase flow pressure drop correlations that have been developed for the application of PEM fuel cell. It also reviews the effect of different working conditions on the two-phase flow pressure drop in PEM fuel cell flow channels.

## 5.2 Introduction

A proton exchange membrane (PEM) fuel cell is considered to be an efficient and pollutant free energy system that can generate power for various applications (59, 99). The electrochemical reactions within the electrodes utilize hydrogen and oxygen to generate electricity with heat and water as the byproducts. Reliable fuel cell performance, however, hinges upon a uniform and continuous supply of reactants across the electrodes. The water produced during the operation of the cell can fill open pores of the gas diffusion layer (GDL) and block the transport of the reactants to the catalyst layers. This phenomenon is referred to as GDL flooding and has been reported to extensively deteriorate the performance of the cell (33, 34, 52). Accumulated liquid water within the GDL emerges from its surface at some preferential locations (54). The liquid water that emerged from the surface of the GDL can be removed by different mechanisms, depending on the gas flow rate and water production rate (5). When the water removal rate is less than the water production rate, a water lens may form within the gas channel. The growth of this lens can ultimately clog the gas channel and block the transport of the reactants to the catalyst layer. This phenomenon is referred to as channel flooding and similar to GDL flooding, it can lower the overall performance of the cell (13, 68, 100). A uniform and continuous supply of reactants across the electrodes can be achieved by acquiring an accurate understanding about the liquid water behavior within the GDL and gas channel.

The accumulation of liquid water within the gas channel follows with the formation of a two-phase flow during the operation of the cell. Channel flooding becomes even more discernible at low temperatures and/or high current densities in which water accumulation increases because of water condensation and water production, respectively.

The transport of an elongated water slug within the gas channel may be influenced by three forces of gravity, surface tension, and shear force of the core gas flow. Bond number,  $Bo = (\rho_f - \rho_g)gD^2/\sigma$ , describes the ratio of the gravity force to the surface tension effect. The small characteristic length scale associated with the PEM fuel cell suggests that gravity's impact on the two-phase flow is insignificant while surface tension has a dominant impact. Moreover, the small characteristic length scales suggest that capillary forces are important to the behavior of liquid surfaces.

Different methods of studying the two-phase flow in gas channels can be categorized as direct and indirect techniques. Direct techniques include monitoring the liquid-gas flow within the gas channel either through a transparent cell (5, 13, 26–28, 47, 60), neutron imaging (30, 90), X-ray microtomography (93, 94), or gas chromatography (91, 92). Bazylak comprehensively reviewed different methods of visualizing liquid water in PEM fuel cell flow fields (24).

The indirect study of the liquid-gas two phase flow in PEM fuel cells can be accomplished by measuring the parameters that are the immediate result of the liquid water accumulation. One such parameter can be the two-phase flow pressure drop along the gas channel as the accumulated water resists the gas flow and causes an increase in the pressure drop. Thus, the two-phase flow pressure drop can be considered as an in-situ diagnostic tool that can reveal information about the amount of liquid water accumulated within the gas channel. While a low pressure drop along the flow channel is desired because of the lower compressor power to supply reactant gases, a mini-

imum pressure drop along the gas channel should be maintained to ensure condensate removal from the flow channels. Different aspects of liquid-gas two-phase flow in gas flow channels of PEM fuel cells have been reviewed by Anderson et al. (101).

In this paper, the two-phase flow pressure drop in the PEM fuel cell flow channels is reviewed. This is achieved first by reviewing the two-phase flow patterns and two-phase flow pressure drop models proposed for general applications. The study is then followed by focusing on the two-phase flow pressure drop with the application of PEM fuel cells. In Section 5.3, different patterns of two phase flows are introduced. The models developed to predict the two-phase flow pressure drop are presented in Section 5.4. Section 5.5 focuses on the two-phase flow pressure drop in PEM fuel cells. In section 5.6 the models that have been proposed for predicting the two-phase flow pressure drop in PEM fuel cell flow channels are reviewed. The overall conclusions drawn from this study are presented in section 5.7. It should be added that only literature with experimental approaches are reviewed in this paper and studies with computational approaches are not included.

## Nomenclature

$Bo$	Bond number
$Bo^*$	Modified Bond number
$C$	Parameter in Lockhart-Martinelli correlation
$D$	Channel diameter
$D_h$	Hydraulic diameter
$Fr$	Froude number
$f$	Fanning friction factor
$g$	gravitational acceleration
$G$	Mass flux ( $\frac{kg}{m^2s}$ )
$j_f$	Superficial liquid velocity
$j_g$	Superficial gas velocity
$N_{conf}$	Confinement number
$P$	pressure
$Re$	Reynolds number
$Re_f$	Reynolds number based on superficial liquid velocity, $Re_f = G(1 - x)D_h/\mu_f$
$v$	specific volume
$We$	Weber number
$x$	mass flow quality
$X$	Lockhart-Martinelli parameter
Greek symbols	
$\alpha$	void fraction
$\rho$	density
$\beta$	channel aspect ratio ( $\beta < 1$ )
$\sigma$	surface tension
$\phi$	two-phase flow frictional multiplier, channel inclination angle
$\mu$	dynamic viscosity

Subscript

A	acceleration
F	frictional
G	gravitational
TP	two-phase
f	saturated liquid
g	saturated vapor
z	stream wise coordinate
fg	difference between saturated vapor and saturated liquid
fo	liquid only
go	vapor only
tt	turbulent liquid-turbulent vapor
tv	turbulent liquid-laminar vapor
vt	laminar liquid-turbulent vapor
vv	laminar liquid-laminar vapor

## 5.3 Two-Phase Flow

Liquid-gas two phase flow is a common type of flow in many industrial applications such as heat exchangers, condensers, chemical processing plants, air conditioners, and fuel cells. Two phase flow occurs in different patterns depending on the liquid to gas ratio, the superficial velocity of each phase, the surface characteristics of the channel, and the channel geometry. The superficial fluid velocity is defined as the bulk velocity of the fluid flowing within the channel cross-sectional area. In this section, different two phase flow patterns introduced in literature are reviewed. All of the flow patterns observed both in general application and PEM fuel cell will be introduced. The section starts with presenting the channel classification considered in this paper. The classification has been proposed by Kandlikar (102) and can be considered to be a sound reference for categorizing small flow channels with engineering applications. After reviewing different patterns of two-phase flow, liquid water transport mechanisms through and on the surface of the GDL will be introduced.

### 5.3.1 Channel classification

Two-phase flow occurs in many engineering applications with different length scales. The length scale of a channel defines the forces that can affect the transport mechanism. For instance, the two phase flow in small channels of a compact heat exchanger is significantly affected by the surface characteristics, while the effects of surface characteristics on the two-phase flow passing through a large pipe of a chemical processing plant is almost negligible. An accurate study of the two-phase flow can only be accomplished by assorting flows based on their channel size. Kandlikar (102) has proposed a channel classification that can be used both for single phase and two-phase flows. The proposed classification is based on the channel hydraulic diameter and spans from

sub-microns to millimeters. According to the classification proposed, channels with hydraulic diameters greater than 3mm are referred to as conventional channels. Fuel cell gas channels are categorized as minichannels with hydraulic diameters between  $200\mu\text{m}$  and 3mm. The classification considers channels with hydraulic diameters between  $10\mu\text{m}$  and  $200\mu\text{m}$  as microchannels. However, microchannels fall below the length scale of PEM fuel cell gas channels.

### 5.3.2 Two-phase flow patterns

Different patterns of two-phase flow in minichannels have been well categorized by Triplett et al. (4). They supplied water and air through circular and semi-triangular (with one corner smoothed) minichannels of Pyrex with different hydraulic diameters between 1.09mm and 1.49mm. According to their classification, the two phase flow in minichannels can transport in five different patterns, bubbly flow, slug flow, churn flow, slug-annular flow, and annular flow, as shown in Figure 1. Bubbly flow contains randomly dispersed bubbles with diameters smaller than the channel diameter. Slug flow includes elongated bubbles and occurs at a lower superficial liquid velocity compared to bubbly flow. Bubbles can elongate by increasing the superficial gas velocity and/or decreasing the superficial liquid velocity. Churn flow is characterized by unstable bubbles or wavy annular flow and transits into slug-annular flow at lower liquid flow rates. The slug-annular flow can be described as wavy-annular flow with individual waves that do not block the channel. Finally, a dramatic increase in the superficial gas velocity eliminates the wavy form of the slug-annular flow and results in annular flow within the gas channel.

Two-phase flow patterns have been extensively studied in other literature (103–117). Two-phase flow patterns are not limited to the patterns that have been defined by Triplett et al. (4) in minichannels. For instance in conventional channels, Wambs-

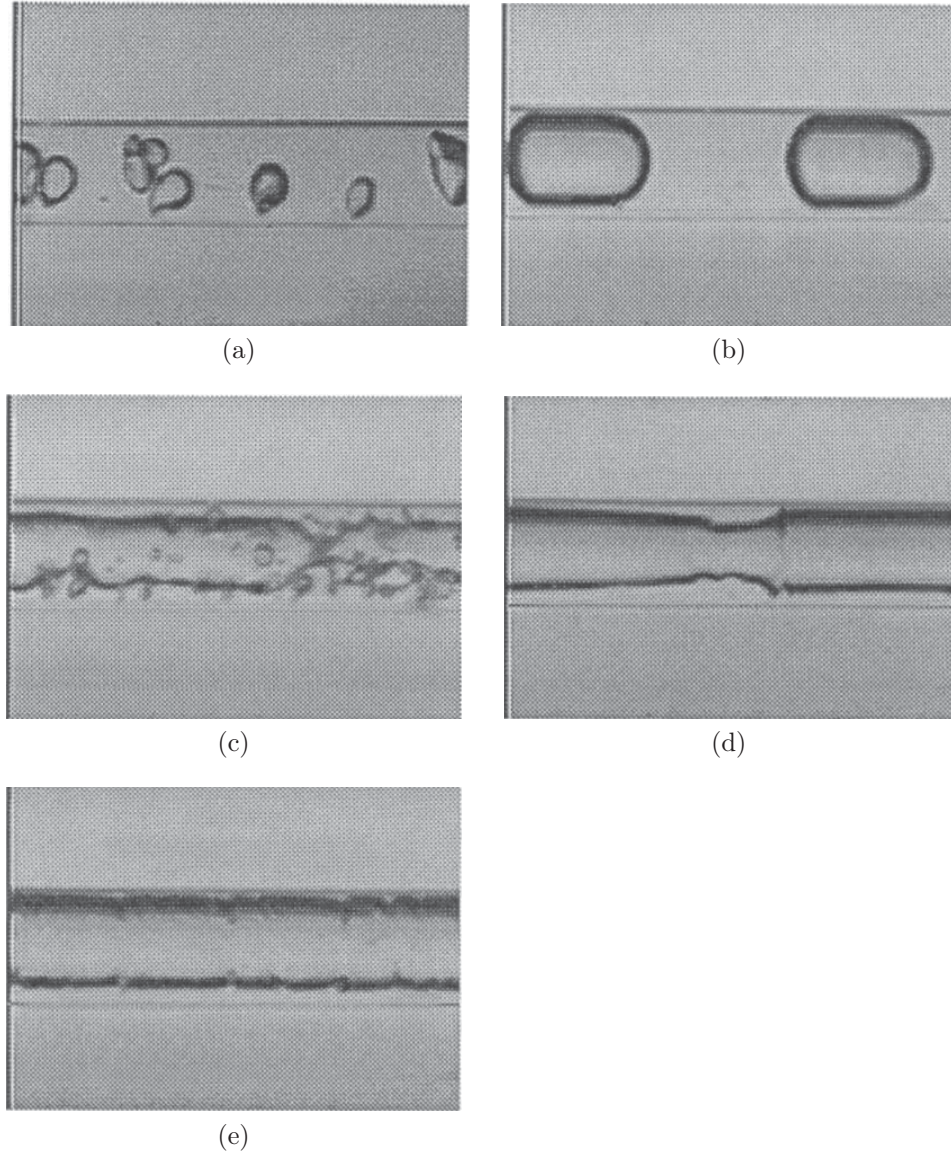


Figure 5.1: Two phase flow patterns reported by Triplett et al. (4). a) Bubbly flow  $j_f = 3.021\text{m/s}$ ,  $j_g = 0.083\text{m/s}$  b) Slug flow  $j_f = 0.213\text{m/s}$ ,  $j_g = 0.154\text{m/s}$  c) Churn flow  $j_f = 1.205\text{m/s}$ ,  $j_g = 4.631\text{m/s}$  d) Slug-annular flow  $j_f = 0.043\text{m/s}$ ,  $j_g = 4.040\text{m/s}$  e) Annular flow  $j_f = 0.082\text{m/s}$ ,  $j_g = 73.30\text{m/s}$

ganss et al. (111) has defined stratified flow pattern as having a smooth liquid and gas interface. In this pattern of two-phase flow, liquid flows on the bottom of the channel because of the gravity. However, it should be mentioned that the two-phase



flow patterns introduced by Triplett et al. (4) are the main flow patterns that can be observed in mini-channels.

Zhao and Bi (118) reported that each pattern of two-phase flow has its own pressure drop profile signature. The bubbly flow, for instance, has minimal pressure drop with the least pressure oscillation. Annular flow, on the other hand, is reported to have the maximum pressure drop with moderate pressure oscillation. The high pressure drop in annular flow originates from the high gas flow rate. Finally, the maximum pressure oscillation is mentioned to occur in churn flow.

Not all of the flow patterns that have been introduced by Triplett et al. (119) occur in PEM fuel cell flow channels. For instance, the low superficial liquid velocity in PEM fuel cell gas channels does not allow the formation of bubbly flow. Similarly, the formation of churn flow is impossible as it requires a high liquid to gas ratio. Water transport in the gas channels of PEM fuel cells has been studied and categorized by Zhang et al. (5). They studied water transport in gas flow channels of a transparent PEM fuel cell and observed that flow patterns change with superficial gas velocity and the liquid water production rate. For a low water production rate and a low gas flow rate, water can spread over hydrophilic channels and drain via channel corners. When the water production rate is moderate and corner flow is not sufficient to remove liquid water with a comparable rate, corner flow may change into annular film flow within the gas channel. The instability of thick water films may turn the annular film flow into slug flow which eventually clogs the channel and shuts off the cell. Figure 2 shows the three flow patterns of corner flow, annular film flow, and slug flow reported by Zhang et al. (5) Other than these, another pattern of two-phase flow has also been classified which is the characteristic of high gas flow rates. For sufficiently high gas flow rates, the shear force of the core gas flow can detach water droplets from the GDL surface to form mist flow.

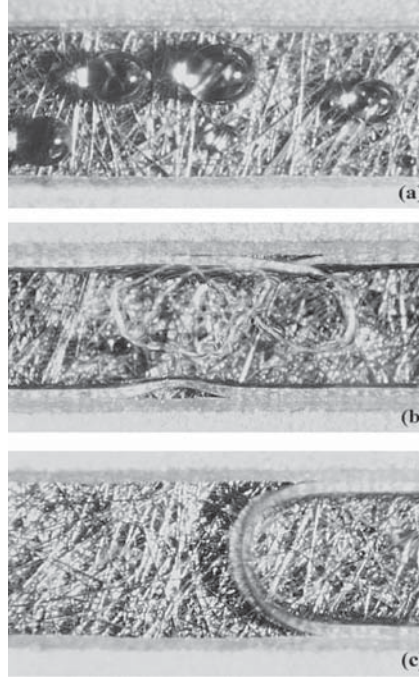


Figure 5.2: Two phase flow patterns observed in PEM flow channels reported by Zhang et al. (5). a) corner flow with emergence of droplets b) annular film flow c) slug flow

The two phase flow map at different liquid and gas flow ranges has been investigated in many studies (4, 6, 7, 12, 13, 15, 18, 95, 103, 104, 106, 118). Lu et al. (6) presented a flow pattern map for flow ranges of PEM fuel cells, as shown in Figure 3. The map contains different flow patterns that have been identified by Zhang et al. (5) The flow pattern map shown in Figure 3 can be used to determine the water transport mechanism at different water and air superficial velocities.

Among different two phase flow patterns that occur in PEM fuel cell flow channels, mist flow is reported to be the most efficient mode of liquid water removal from the gas channels (6). However, its high pressure drop requirements lowers the overall efficiency of the system. Despite mist flow that requires a high pressure drop, slug flow occurs at low pressure drop but this pattern of two-phase flow is not desirable as it can lead to performance degradation because of its low water removal rate (6).

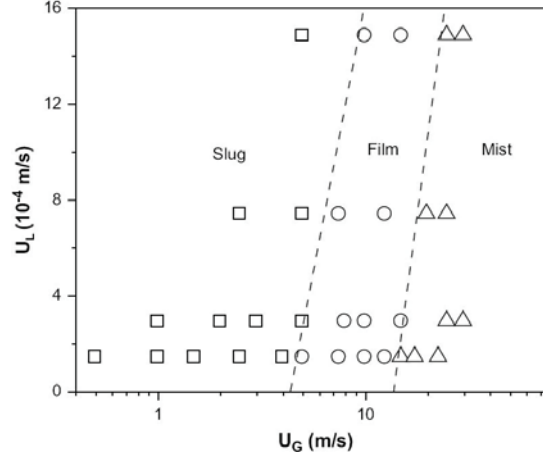


Figure 5.3: Two-phase flow pattern map reported by Lu et al. (6)

Moreover, slug flow may also lead to flow mal-distribution that is defined as the accumulation of excess water in one channel while other channels dry out because of excessive air flow rate (120). Flow mal-distribution has been reported to reduce the operating lifetime of a fuel cell (121). While mist flow and slug flow are not suitable modes of liquid water transport in PEM fuel cell flow channels, film flow has been reported to be a desirable mode of liquid water removal as it can be achieved at a moderate pressure drop and is capable of keeping an appropriate balance between the produced water and the removed water (6). Furthermore, film flow is reported to be a desirable liquid water transport mode in PEM fuel cells because water transports along the channel sidewalls instead of the GDL surface (122).

Because slug flow is the most common flow pattern in PEM fuel cells (6), more attention should be paid to eliminate the issues that arise with this pattern of flow. One such issue can be the flow mal-distribution with the direct consequences being current re-distribution, erratic current fluctuation, and pressure drop fluctuation within the cell. Flow mal-distribution in PEM fuel cell parallel gas channels has been extensively investigated (16, 120, 123, 124). The overall conclusion suggests that the equal pressure drop for multiple parallel gas channels does not necessarily ensure even

distribution of gas and liquid phases. This is because different combinations of liquid and gas flow rates can result in the same pressure drop.

### **5.3.3 Liquid water transport through the porous GDL**

In Section 5.3.2, different modes of liquid water transport in gas channels of the PEM fuel cell was reviewed. While researchers have acquired a solid knowledge about water transport mechanisms within the gas channels of the PEM fuel cell, water transport mechanisms through the porous structure of GDL is still under discussion. In this section, some major hypotheses about water transport mechanisms through the GDL will be introduced.

Nam and Kaviani (35) investigated the distribution of condensed water within the GDL and suggested that the liquid water transports from the catalyst layer to the gas channel in a branching type geometry. Based on their model, micro-droplets form in the condensation site of the catalyst layer and transport into the larger pores of the GDL, via capillary flow, to form macro-droplets. The capillary transport continues until a large droplet emerges from the surface of the GDL. This transport mechanism can be described as tree-like percolation and has been confirmed by Pasaogullari and Wang (34).

Benziger et al. (2) modeled GDL as a single solid layer which contains parallel microchannels with different diameters. Liquid water passes through the channel with the largest diameter to yield the minimum breakthrough pressure.

Litster et al. (36) employed fluorescence microscopy to visualize the water transport through the GDL. They postulated that water transport is mostly dominated by fingering and channeling and does not necessarily follow the capillary tree model suggested in (34, 35). Bazylak et al. (54) followed the same visualization technique and observed that droplets emerge from the surface of the GDL at preferential lo-

cations. These locations were reported to randomly change over time. According to their observation, the GDL was described as a network of pores that is characterized by dynamic interconnections of water pathways.

Tamayol and Bahrami (3) modeled the GDL as a network of pores connected by throats. The throats resist the water transport through the GDL while pores do not apply any resistance. The GDL model proposed by Tamayol and Bahrami (3) confirms the transport behavior observed by Bazylak (54).

Different models of liquid water transport through the GDL were reviewed. The tortuous structure of the GDL may justify the possibility of each of these mechanisms. The results reported in an in-situ study done with synchrotron X-ray radiography (125) confirms the dynamic transport model proposed by Litster (36) and Bazylak (24) as well as the branching-type geometry proposed by Pasaogullari and Wang (34) and Nam and Kaviany (35).

## 5.4 Two-Phase Flow Pressure Drop Models

The single-phase pressure drop of fluids is well understood and can be predicted over a wide range of operating conditions. The liquid-gas two-phase flow pressure drop, however, is not well identified and has been studied only for a limited range of operating conditions relevant to particular areas of interest. The physics behind this type of transport phenomena is very complicated to be modeled with simplified mathematical expressions. Therefore, the majority of published works try to improve the already known expressions by correlating the experimental results.

The two-phase flow pressure drop is the sum of frictional, gravitational and accelerational pressure drop:

$$\Delta P_{\text{TP}} = \Delta P_{\text{TP,F}} + \Delta P_{\text{TP,G}} + \Delta P_{\text{TP,A}} \quad (5.1)$$

The acceleration pressure gradient is expressed as:

$$-\left(\frac{dP}{dz}\right)_{\text{A}} = G^2 \frac{d}{dz} \left[ \frac{v_{\text{g}} x^2}{\alpha} + \frac{v_{\text{f}} (1-x)^2}{(1-\alpha)} \right] \quad (5.2)$$

where mass flow quality,  $x$ , is defined as:

$$x = \frac{G_{\text{g}}}{G_{\text{g}} + G_{\text{f}}} \quad (5.3)$$

The void fraction  $\alpha$  is the gas hold-up in the liquid stream and can be measured by different methods, such as constant electric current method (126), quick closing valve (103), and even image analysis (105, 106). Zivi (127) expressed void fraction as a function of mass flow quality,  $x$ , and liquid and gas density:

$$\alpha = \left[ 1 + \left( \frac{1-x}{x} \right) \left( \frac{\rho_{\text{g}}}{\rho_{\text{f}}} \right)^{2/3} \right]^{-1} \quad (5.4)$$

It has been shown that for low liquid and gas superficial velocities, the acceleration pressure drop incorporates a small fraction of the overall two-phase flow pressure drop (119), while the acceleration pressure drop becomes significant at high superficial velocities (119, 128).

For an inclined channel with the inclination angle of  $\phi$ , the gravitational pressure gradient can be expressed as:

$$-\left(\frac{dP}{dz}\right)_{\text{G}} = [\alpha \rho_{\text{g}} + (1-\alpha) \rho_{\text{f}}] g \sin \phi \quad (5.5)$$

For a horizontal channel, this angle will equal zero and the overall gravitational pressure gradient will be zero. Gravitational pressure gradient has a significant contribu-

tion to the overall pressure drop in macro-channels and becomes even more dominant in low mass velocities. For mini/micro channels, however, the dominant impact of surface tension diminishes the gravitational effects.

The two-phase flow frictional pressure drop is generally predicted based on two different approaches, depending on how each phase of fluid is treated. In one approach, the two-phase mixture is considered as a pseudo single phase fluid with properties such as viscosity and density weighted to the quality. This model is known as the homogeneous equilibrium model (also referred to as the viscosity model) and has been proven to give a more accurate prediction at higher mass qualities (7, 20, 110). In the other method, the two-phase pressure drop corresponds to the single-phase pressure drop multiplied by a two-phase flow frictional multiplier,  $\phi$ . This method is known as the separated flow model and was originally introduced by Lockhart and Martinelli in 1949 (129).

Much research has been done to compare the experimentally measured frictional two-phase flow pressure drops with those predicted by homogeneous and/or separated flow models. Table 5.1 lists some studies doing such comparisons.

Table 5.1: Literature comparing the predicted and measured two-phase flow pressure drops

Author	Channel geometry <sup>2</sup>	Channel material	$D_h$ (mm)	Fluids	Mass flux $\text{kgm}^{-2}\text{s}^{-1}$
Bao (1994) (130)	C, UV, H	Glass and copper	glass (0.74-3.07) copper (1.98)	Air-water glycerin water mixture	water 7-2400 air 0.18-60
Chang (1996) (131)	C, H	Copper	1.2, 1.6	pure R-32, R-125, R-134A and their mixture	3980-9370
Yan (1998) (132)	C, H	Not Specified	2	R-134A	50-200
Wang (2000) (115)	C, H	Copper	3.17	Air-water	50-700
Wang (2001) (133)	C, H	Not Specified	3-9	R-22, R-407C, R-410A	50-700
Zhao (2001) (118)	T, UV	Lucite	0.886-2.886	Air-water	water 10-10,000 Air 0.12-120
Chen (2001) (134)	C, H	Copper	Air-water (1.02-7.02)	Air-water	Air-water (50-3000)
Zhang (2001) (135)	C, H	Aluminum, copper	R-410A (3.17-9) Al (2.13)	R-410A R-134A, R-22, R-404A	R-410A (50-600) 200-1000
Kawahara (2002) (105)	C, H	Fused silica	Copper (3.25, 6.25) 0.1	de-ionized water-nitrogen	water 20-4000 nitrogen 0.12-72
Yu (2002) (136)	C, H	stainless steel	2.98	water, ethylene glycol and mixture	50-200
Bandarra Filho (2004) (137)	C, H	Copper	6.24-8.92	R-134A	70-1100
Greco (2004) (138)	C, H	Stainless steel	6	R-22, R-507	250-286
Wongsa-ngam (2004) (139)	C, H	Copper	8.12	R-134A	400-800
Choi (2005) (140)	C, H	stainless steel	1.5, 3	R-410A, R-407C	300-600
Wongwises (2006) (103)	C, H, inclined (30°, 60°)	acrylic glass	8	Air-water	water 69-6020 Air 0.026-78.6
Pehlivan (2006) (141)	C, H	borosilicate glass	0.8-3	Air-water	Water 20-1000 Air 12-120
Chen (2007) (142)	R, H	Transparent acrylic resin	3-5	Air-water	100-700
Mauro (2007) (143)	C, H	Stainless steel	6	R-22, R-134A R-410A, R-417A R-404A, R-507A R-407C	190-1150
Lee (2008) (144)	C, H	Teflon, Glass polyurethane	1.62-2.16	Air-water	water 6-154
Saisorn (2008) (104)	C, H	Fused silica	0.53	Air-water	Air 0.05-0.65 Water 5-3040 Air 0.44-19.2

C: circular, R: rectangular, T: triangular, UV: upward vertical, H: horizontal



Table 5.1: Literature comparing the predicted and measured two-phase flow pressure drops, continue

Author	Channel geometry <sup>3</sup>	Channel material	$D_h$ (mm)	Fluids	Mass flux $\text{kgm}^{-2}\text{s}^{-1}$
Choi (2008) (128)	C, H	Stainless steel	1.5, 3	R-410A	300-600
Tran (2000) (145)	C, R, H	Brass (R-134A, R-12) Stainless steel (R-113)	C (2.46, 2.92) R (2.39)	R-134A, R-12, R-113	R-134A 33-502 R-12 44-832 R-113 50-400
da Silva Lima (2009) (146)	C, H	stainless steel	14	R-717 (ammonia)	50-160
Hu (2009) (147)	C, H	Not specified	2, 4.18	R-410A, oil	200-620
Kaew-On (2009) (148)	R, H	Aluminum	3.48	R-410A	200-400
Quiben (2009) (149)	C, flattened, H	copper	C (8-13.84) Flattened (3.71-5.35)	R-22, R-410A	150-500
Choi (2011) (114)	R, H	Photosensitive glass	0.143-0.49	water-nitrogen gas	Liquid 66-1000 Gas 0.07-80
Venkatesan (2011) (113)	C, H	Silica glass	0.6-3.4	Air-water	Water 10-3000 Gas 0.01-60
Wu (2011) (150)	C, H	stainless steel	1.42	$CO_2$	300-600
Saisorn (2011) (151)	C, H	Fused silica	0.15, 0.53	Air-water	Not specified

C: circular, R: rectangular, T: triangular, UV: upward vertical, H: horizontal

### 5.4.1 Homogeneous Equilibrium Model

In the homogeneous equilibrium model the two-phase mixture is treated as a pseudo single-phase fluid and the properties are mean weighted relative to each liquid and gas content. Because it is assumed that the liquid and gas phases are moving at the same speed, this model has also been named the zero slip model. According to the homogeneous method, the two-phase flow pressure drop can be calculated by:

$$\left(\frac{dP}{dz}\right)_{\text{TP}} = \frac{2f_{\text{TP}}G^2}{D_h\rho_{\text{TP}}} \quad (5.6)$$

where the two-phase friction factor,  $f_{\text{TP}}$ , depends on the two-phase flow Reynolds number,  $Re_{\text{TP}}$ :

$$f_{\text{TP}} = \begin{cases} \frac{16}{Re_{\text{TP}}} & \text{for } Re_{\text{TP}} < 2000 \\ 0.079Re_{\text{TP}}^{-0.25} & \text{for } 2000 \leq Re_{\text{TP}} < 20,000 \\ 0.046Re_{\text{TP}}^{-0.2} & \text{for } Re_{\text{TP}} \geq 20,000 \end{cases} \quad (5.7)$$

The two-phase Reynolds number is calculated based on the two-phase mixture viscosity,  $\mu_{\text{TP}}$ :

$$Re_{\text{TP}} = \frac{Gd_h}{\mu_{\text{TP}}} \quad (5.8)$$

Different models of two-phase viscosity have been introduced (152–158) and are well discussed and compared (159–162). Table 5.2 lists some of the two-phase viscosity models that have been introduced.

Table 5.2: Two-phase viscosity model

Author	Equation
McAdams et al.(152)	$\frac{1}{\mu_{TP}} = \frac{x}{\mu_g} + \frac{1-x}{\mu_f}$
Akers et al.(153)	$\mu_{TP} = \frac{\mu_f}{[(1-x) + x(\frac{v_g}{v_f})^{0.5}]}$
Cicchitti et al. (154)	$\mu_{TP} = x\mu_g + (1-x)\mu_f$
Owens (155)	$\mu_{TP} = \mu_f$
Dukler et al.(156)	$\mu_{TP} = \frac{xv_g\mu_g + (1-x)v_f\mu_f}{xv_g + (1-x)v_f}$
Beattie and Walley (157)	$\mu_{TP} = \beta\mu_g + (1-\beta)(1+2.5\beta)\mu_f$
	$\beta = \frac{\rho_f x}{\rho_f x + \rho_g(1-x)}$ (here $\beta$ is not the aspect ratio)
Lin et al. (158)	$\mu_{TP} = \frac{\mu_f\mu_g}{\mu_g + x^{1.4}(\mu_f - \mu_g)}$

In Equation 5.6,  $\rho_{TP}$  is the density of the pseudo fluid and is given by:

$$\rho_{TP} = \left(\frac{x}{\rho_g} + \frac{1-x}{\rho_f}\right)^{-1} \quad (5.9)$$

For rectangular channels and for laminar flow, the two-phase friction factor,  $f_{TP}$ , can also be obtained by (163):

$$f_{TP}Re_{TP} = 24[1 - 1.3553\beta + 1.9467\beta^2 - 1.7012\beta^3 + 0.9564\beta^4 - 0.2537\beta^5] \quad (5.10)$$

where  $\beta$  is the aspect ratio of the channel and is defined as the ratio of the width to the height of the channel.

The accuracy of the homogeneous flow model in predicting the two-phase flow pressure drop was examined by Triplett et al (119). It has been reported that although the homogeneous flow model can appropriately predict the pressure drop for bubbly and slug flows, it results in significant deviation from the actual pressure drop in slug-annular and annular flow patterns. Even at a low Reynolds number, such as 70, the homogeneous flow model was observed to over-predict the pressure drop.

#### 5.4.2 Separated Flow Model

In the separated flow model, the two-phase flow pressure drop is predicted based on the pressure drop of one phase multiplied by the two-phase frictional multiplier:

$$\left(\frac{dP}{dz}\right)_{\text{TP}} = \phi_{\text{f}}^2 \left(\frac{dP}{dz}\right)_{\text{f}} \quad (5.11)$$

where  $\phi_{\text{f}}^2$  is the two-phase frictional multiplier based on liquid and has been reported to depend on the flow pattern (164). The Martinelli parameter,  $X$ , is defined as:

$$X = \left[ \left(\frac{dP}{dz}\right)_{\text{f}} / \left(\frac{dP}{dz}\right)_{\text{g}} \right]^{\frac{1}{2}} \quad (5.12)$$

This model was followed by Chisholm (19) by introducing the Chisholm parameter,  $C$ . The Chisholm parameter is used to define the frictional multiplier:

$$\phi_{\text{f}}^2 = \frac{\left(\frac{dP}{dz}\right)_{\text{TP}}}{\left(\frac{dP}{dz}\right)_{\text{f}}} = 1 + \frac{C}{X} + \frac{1}{X^2} \quad (5.13)$$

The original concept of the Chisholm correlation (Eq. 5.13) came from the fact that the two-phase flow pressure drop is equal to the sum of the pressure drop for each of the phases of liquid and gas and the interaction between these two phases:

$$\left(-\frac{dp}{dz}\right)_{\text{TP}} = \left(-\frac{dp}{dz}\right)_{\text{f}} + \left(-\frac{dp}{dz}\right)_{\text{g}} + C \left[ \left(-\frac{dp}{dz}\right)_{\text{f}} \left(-\frac{dp}{dz}\right)_{\text{g}} \right]^{\frac{1}{2}} \quad (5.14)$$

The Chisholm parameter,  $C$ , is a measure of the interaction between two phases, and similar to the frictional multiplier, it has been reported to depend on the flow regime (164). Table 5.3 lists the values of the Chisholm parameters depending on the flow regimes of liquid and gas phases (19).

Table 5.3: Values of Chisholm parameter (19)

Two-phase flow characteristics	Chisholm's parameter $C$
Laminar liquid-laminar gas	5
Turbulent liquid-laminar gas	10
Laminar liquid-turbulent gas	12
Turbulent liquid-turbulent gas	21

Many studies have investigated the two-phase flow pressure drop for different applications based on the separated flow model. Table 5.4 lists some of the proposed pressure drop correlations based on the separated flow model.

Friedel (165) used 25,000 data points of pressure drops in horizontal pipes with diameters greater than 44mm and correlated  $\phi_{\text{f}}^2$  with gravity, surface tension, and total mass flux using Froude and Weber numbers, as given in Table 5.4.

Müller-Steinhagen and Heck (166) proposed a new correlation for the two-phase flow frictional pressure drop by considering 9300 data points for different fluids passing through the channels with diameters ranging from 4mm to 392mm. Their correlation has been known as a reliable frictional pressure drop model that provides minimal

deviation from the actual pressure drop compared to other existing correlations (106, 159, 167, 168).

Most of the early studies done on the two-phase flow pressure drop were based on the pressure drop measured in channels with large hydraulic diameters. The correlations proposed in those studies proved to yield an inferior prediction of pressure drop in recently developed micro-scale devices. As the channel size decreases from conventional channel to mini-/micro-channels, the surface tension effects become more dominant and the gravity becomes less important. Most of the studies focusing on the two-phase flow pressure drop in mini/micro channels concentrate on a specific application such as compact heat exchangers, refrigeration systems, or microtube condensers.

Lowry and Kawaji (112) were among the first researchers who studied the two-phase flow pressure drop in minichannels. They investigated the variation of  $\phi^2$  with dimensionless gas velocity and concluded that although the two-phase frictional multiplier strongly depends on dimensionless gas velocity, it is relatively independent of superficial liquid velocity and channel size.

Jung and Radermacher (169) ran a considerable number of experiments with both pure and mixed refrigerants flowing within stainless steel tubes with a diameter of 9.1mm and developed a simple correlation for predicting the two-phase flow pressure drop based on Martinelli's parameter. In their correlation, the two-phase frictional multiplier depends on quality and reduced pressure, as given in Table 5.4.

Ide and Matsumura (110) studied the effects of channel geometry on the two-phase flow pressure drop in rectangular channels. They used channels with different aspect ratios, hydraulic diameters, and inclination angles and found that the Lockhart-Martinelli method does not accurately predict the experimental results with low liquid superficial velocities and high inclination angles. They used the separated flow model and proposed a correlation that predicts the frictional pressure drop as a function

of channel aspect ratio, inclination angle, Reynolds number, and void fraction. The pressure drop correlation that they proposed is given in Table 5.4.

Many efforts have been made to modify the Chisholm parameter to make the predicted pressure drop closer to the actual value measured experimentally. Mishima and Hibiki (170) studied two-phase flow of air and water in round capillary tubes with diameters ranging from 1mm to 4mm. They noticed that the Chisholm parameter should also be a function of channel diameter, rather than just the two-phase flow pattern. They studied the variation of the two-phase flow multiplier as a function of the Lockhart-Martinelli parameter for different diameters and observed that the Chisholm parameter decreases with the tube diameter. This led them to propose a modified Chisholm parameter that takes into account the diameter of the channel. For circular channels, the Chisholm parameter was proposed to be calculated by:

$$C = 21(1 - e^{-0.333D}) \quad (5.15)$$

where  $D$  is the channel diameter in meters. For rectangular channels, the Chisholm parameter was recommended to be obtained by the following equation:

$$C = 21(1 - e^{-0.319D_h}) \quad (5.16)$$

where  $D_h$  is the hydraulic diameter.

Table 5.4: Two-phase frictional pressure gradient correlation

Author	Equation	Setup
Lockhart and Martinelli (129)	$\left(\frac{dP}{dz}\right)_{\text{TP,F}} = \left(\frac{dP}{dz}\right)_f \phi_f^2, \phi_f^2 = 1 + \frac{C}{X} + \frac{1}{X^2}$	$D = 1.49 - 25.83\text{mm}$
	$X^2 = \frac{\left(\frac{dP}{dz}\right)_f}{\left(\frac{dP}{dz}\right)_g}, C_{\text{vv}}, C_{\text{tv}}, C_{\text{vt}}, \text{ and } C_{\text{tt}} \text{ as given in Table 5.3}$	water, oils, hydrocarbon
Friedel (165)	$\left(\frac{dP}{dz}\right)_{\text{TP,F}} = \left(\frac{dP}{dz}\right)_f \phi_f^2$	$D > 4\text{mm}$
	$\phi_f^2 = (1-x)^2 + x^2 \left(\frac{v_g}{v_f}\right) \left(\frac{f_{\text{go}}}{f_{\text{fo}}}\right) + 3.24x^{0.78} (1-x)^{0.224} \left(\frac{v_g}{v_f}\right)^{0.91} \left(\frac{\mu_g}{\mu_f}\right)^{0.19} \left(1 - \frac{\mu_g}{\mu_f}\right)^{0.7} Fr_{\text{TP}}^{-0.045} We_{\text{TP}}^{-0.035}$	air-water, air-oil, R12
	$Fr_{\text{TP}} = \frac{G^2}{gD_h\rho_h^2}, We_{\text{TP}} = \frac{G^2D_h}{\sigma\rho_h}, \rho_h = \frac{1}{xv_g + (1-x)v_f}$	
Müller-Steinhagen and Heck (166)	$\left(\frac{dP}{dz}\right)_{\text{TP,F}} = \left[\left(\frac{dP}{dz}\right)_f + 2\left[\left(\frac{dP}{dz}\right)_g - \left(\frac{dP}{dz}\right)_f\right]x\right](1-x)^{1/3} + \left(\frac{dP}{dz}\right)_g x^3$	$D = 4 - 392\text{mm}$
		air-water, hydrocarbons refrigerants
Jung and Radermacher (169)	$\left(\frac{dP}{dz}\right)_{\text{TP,F}} = \left(\frac{dP}{dz}\right)_f \phi_f^2, \phi_f^2 = 12.82X_{\text{tt}}^{-1.47}(1-x)^{1.8}$	$D = 9.1\text{mm}$
	$X_{\text{tt}} = \left(\frac{\mu_f}{\mu_g}\right)^{0.1} \left(\frac{1-x}{x}\right)^{0.9} \left(\frac{\rho_g}{\rho_f}\right)^{0.5}$	pure and mixed refrigerants
Ide and Matsumura (110)	$\phi_f = C(\theta)Re_{\text{to}}^{-m}\chi_{\text{tt}} \left[\frac{(\beta+1)(\beta+\alpha)}{[\beta+2(1-\alpha)]^2}\right]^{-0.625} \left[\frac{\alpha}{(1-\alpha)^2}\right]^{1.5}$	$D = 7.3 - 21.4\text{mm}$
	$\chi_{\text{tt}}$ is the Lockhart-Martinelli parameter for turbulent liquid and gas flow turbulent	air-water
	$m = 0.3, C(\theta) = 0.57 + 2.07 \times 10^{-2}\theta - 1.818 \times 10^{-4}\theta^2$	$D_h > 10\text{mm}$
	$m = 1.0, C(\theta) = 170 + 11.18\theta - 9.63 \times 10^{-2}\theta^2$	$D_h < 10\text{mm}$



Table 5.4, continue: Two-phase frictional pressure gradient correlation, Continue

Author	Equation	Setup
Wambsganss et al. (171)	$\left(\frac{dP}{dz}\right)_{\text{TP,F}} = \left(\frac{dP}{dz}\right)_f \phi_f^2, \phi_f^2 = 1 + \frac{C}{X} + \frac{1}{X^2}$ $C = f(X, Re_{fo}) = aX^b, a = -2.44 + 0.00939Re_{fo}, b = -0.938 + 0.000432Re_{fo}$	$D_h = 5.44\text{mm}$ air-water
Wang et al. (164)	<p>For <math>G \geq 200\text{kg}/\text{m}^2\text{s}</math>, <math>\left(\frac{dP}{dz}\right)_{\text{TP,F}} = \left(\frac{dP}{dz}\right)_g \phi_g^2, \phi_g^2 = 1 + 9.4X^{0.62} + 0.564X^{2.45}</math></p> <p>For <math>G &lt; 200\text{kg}/\text{m}^2\text{s}</math>, <math>\left(\frac{dP}{dz}\right)_f = \left(\frac{dP}{dz}\right)_f \phi_f^2, \phi_f^2 = 1 + \frac{C}{X} + \frac{1}{X^2}</math></p> $C = 4.566 \times 10^{-6} X^{0.128} Re_{fo}^{0.938} \left(\frac{v_f}{v_g}\right)^{2.15} \left(\frac{\mu_f}{\mu_g}\right)^{5.1}$	$D = 6.5\text{mm}$ R22, R134a, R407C
Zhang and Webb (135)	$\phi_f^2 = (1-x)^2 + 2.87x^2 \left(\frac{P}{P_c}\right)^{-1} + 1.68x^{0.8} (1-x)^{0.25} \left(\frac{P}{P_c}\right)^{-1.64}$	$D_h = 2.13\text{mm}$ R-134a, R22, R404a
Mishima and Hibiki (170)	$\left(\frac{dP}{dz}\right)_{\text{TP,F}} = \left(\frac{dP}{dz}\right)_f \phi_f^2, \phi_f^2 = 1 + \frac{C}{X} + \frac{1}{X^2}$ <p>For rectangular channel, <math>C = 21[1 - \exp(-319D_h)]</math></p> <p>For circular tube, <math>C = 21[1 - \exp(-333D)]</math></p>	$D = 1.05 - 4.08\text{mm}$
Yang and Webb (172)	$\left(\frac{dP}{dz}\right)_{\text{TP,F}} = -0.87Re_{eq}^{0.12} f_{fo} \frac{G_{eq}^2 v_f}{D_h}, Re_{eq} = \frac{G_{eq} D_h}{\mu_f}, G_{eq} = G \left[ (1-x) + x \left(\frac{\rho_f}{\rho_g}\right)^{0.5} \right]$	$D_h = 1.56 - 2.64\text{mm}$ R12
Yan and Lin (132)	$\left(\frac{dP}{dz}\right)_{\text{TP,F}} = -0.22Re_{eq}^{-0.1} \frac{G_{eq}^2 v_f}{D_h}$	$D = 2\text{mm}$ R134a

Table 5.4, continue: Two-phase frictional pressure gradient correlation, Continue

Author	Equation	Setup
Tran et al. (145)	$\left(\frac{dP}{dz}\right)_{\text{TP,F}} = \left(\frac{dP}{dz}\right)_f \phi_f^2, N_{\text{conf}} = \sqrt{\frac{\sigma}{g(\rho_f - \rho_g)D^2}}$ $\phi_f^2 = 1 + \left[4.3 \frac{(dP/dz)_{\text{go}}}{(dP/dz)_{\text{fo}}} - 1\right] [N_{\text{conf}} x^{0.875} (1-x)^{0.875} + x^{1.75}]$	$D = 2.4 - 2.92\text{mm}$  refrigerants
Chen et al. (134)	$\left(\frac{dP}{dz}\right)_{\text{TP,F}} = \left(\frac{dP}{dz}\right)_{f,\text{Friedel}} \Omega, Bo^* = g(\rho_f - \rho_g) \frac{(D_h/2)^2}{\sigma}$ $\text{for } Bo^* < 2.5, \Omega = \frac{0.0333 Re_{\text{fo}}^{0.45}}{Re_g^{0.09} (1 + 0.4 \exp(-Bo^*))}$ $\text{For } Bo^* \geq 2.5, \Omega = \frac{We_{\text{TP}}^{0.2}}{(2.5 + 0.06 Bo^*)}$	$D = 1.02 - 9\text{mm}$  air-water, R410A, ammonia
Lee and Lee (173)	$\left(\frac{dP}{dz}\right)_{\text{TP,F}} = \left(\frac{dP}{dz}\right)_f \phi_f^2, \phi_f^2 = 1 + \frac{C}{X} + \frac{1}{X^2}, \psi = \frac{\mu_f j_f}{\sigma}, \lambda = \frac{\mu_f^2}{\rho_f \sigma D_h}$ $C = A \lambda^q \psi^r Re_{\text{fo}}^s$ $\text{For laminar liquid-laminar gas flow } A = 6.833 \times 10^{-8}, q = -1.317, R = 0.719, S = 0.557$ $\text{For laminar liquid-turbulent gas flow } A = 6.185 \times 10^{-2}, q = 0, R = 0, S = 0.726$	$D_h = 0.78 - 6.67\text{mm}$  air-water
Saisorn and Wongwises (106)	$\left(\frac{dP}{dz}\right)_{\text{TP,F}} = \left(\frac{dP}{dz}\right)_f \phi_f^2, \phi_f^2 = 1 + \frac{C}{X} + \frac{1}{X^2}, \psi = \frac{\mu_f j_f}{\sigma}, \lambda = \frac{\mu_f^2}{\rho_f \sigma D_h}$ $C = 7.599 \times 10^{-3} \lambda^{-0.631} \psi^{0.005} Re_{\text{fo}}^{-0.008}$	$D = 0.15 - 0.53\text{mm}$  air-water
Yu et al. (136)	$\left(\frac{dP}{dz}\right)_{\text{TP,F}} = \left(\frac{dP}{dz}\right)_f \phi_f^2, \phi_f^2 = \left[18.65 \left(\frac{v_f}{v_g}\right)^{0.5} \left(\frac{1-x}{x}\right) \frac{Re_g^{0.1}}{Re_f^{0.5}}\right]^{-1.9}$	$D = 2.98\text{mm}$  water and ethylene glycol

Table 5.4, continue: Two-phase frictional pressure gradient correlation, Continue

Author	Equation	Setup
Hwang and Kim (174)	$\left(\frac{dP}{dz}\right)_{\text{TP,F}} = \left(\frac{dP}{dz}\right)_f \phi_f^2, \phi_f^2 = 1 + \frac{C}{X} + \frac{1}{X^2}, C = 0.227 Re_{fo}^{0.452} X^{-0.32} N_{\text{conf}}^{-0.82}$	$D = 0.244 - 0.792\text{mm}$
		R134a
Sun and Mishima (167)	For $Re_f < 2000$ and $Re_g < 2000$ $\left(\frac{dP}{dz}\right)_{\text{TP,F}} = \left(\frac{dP}{dz}\right)_f \phi_f^2 = 1 + \frac{C}{X} + \frac{1}{X^2}$ $C = 26 \left(1 + \frac{Re_f}{1000}\right) \left[1 - \exp\left(\frac{-0.153}{0.27 N_{\text{conf}} + 0.8}\right)\right]$ For $Re_f \geq 2000$ or $Re_g \geq 2000$ $\left(\frac{dP}{dz}\right)_{\text{TP,F}} = \left(\frac{dP}{dz}\right)_f \phi_f^2 = 1 + \frac{C}{X} + \frac{1}{X^2}, C = 1.79 \left(\frac{Re_g}{Re_f}\right)^{0.4} \left(\frac{1-x}{x}\right)^{0.5}$	$D_h = 0.506 - 12\text{mm}$ air-water, refrigerants
Li and Wu (175)	$\left(\frac{dP}{dz}\right)_{\text{TP,F}} = \left(\frac{dP}{dz}\right)_f \phi_f^2 = 1 + \frac{C}{X} + \frac{1}{X^2}, Bo = \frac{g(\rho_f - \rho_g) D_h^2}{\sigma}$ For $Bo \leq 1.5$ , $C = 11.9 Bo^{0.45}$ For $1.5 < Bo \leq 11$ , $C = 109.4 (Bo Re_f^{0.5})^{-0.56}$	$D_h = 0.148 - 3.25\text{mm}$ re- frigerants, ammonia refrigerants, ammonia
Li and Wu (176)	For $Bo < 0.1$ $\left(\frac{dP}{dz}\right)_{\text{TP,F}} = \left(\frac{dP}{dz}\right)_f \phi_f^2, \phi_f^2 = 1 + \frac{C}{X} + \frac{1}{X^2}, C = 5.60 Bo^{0.28}$ For $Bo \geq 0.1$ and $Bo Re_f^{0.5} \leq 200$ $\left(\frac{dP}{dz}\right)_{\text{TP,F}} = \left(\frac{dP}{dz}\right)_f \phi_{fo}^2, \phi_f^2 = (1-x)^2 + 2.87 x^2 P_R^{-1} + 1.54 Bo^{0.19} \left(\frac{\rho_f - \rho_g}{\rho_H}\right)^{0.81}$	$D_h = 0.148 - 3.25\text{mm}$ refrigerants, ammonia

Table 5.4, continue: Two-phase frictional pressure gradient correlation, Continue

Author	Equation	Setup
Zhang et al. (177)	$\left(\frac{dP}{dz}\right)_{\text{TP,F}} = \left(\frac{dP}{dz}\right)_{\text{f}} \phi_{\text{f}}^2, \phi_{\text{f}}^2 = 1 + \frac{C}{X} + \frac{1}{X^2}, C = 21[1 - \exp(-0.142/N_{\text{conf}})]$	$D_{\text{h}} = 0.07 - 6.25\text{mm}$  air-water, refrigerants, ammonia
Lee and Mudawar (160)	$\phi_{\text{f}}^2 = 1 + \frac{C}{X} + \frac{1}{X^2}$  For laminar liquid-laminar gas flow, $C = 2.16Re_{\text{fo}}^{0.047}We_{\text{fo}}^{0.60}$ For laminar liquid-turbulent gas flow, $C = 1.45Re_{\text{fo}}^{0.25}We_{\text{fo}}^{0.23}$	$D_{\text{h}} = 348\mu\text{m}$  R134a

The Chisholm parameter was further improved by Lee and Lee (173) when they measured the two-phase flow pressure drop of water and air in horizontal rectangular channels with hydraulic diameters ranging from 0.78mm to 6.6mm. The modified Chisholm parameter they proposed was a function of flow conditions and fluid properties:

$$C = A\lambda^q\psi^r Re_f^s \quad (5.17)$$

$$\lambda = \frac{\mu_f^2}{\rho_f \sigma D_h}, \quad \psi = \frac{\mu_f(U_g + U_f)}{\sigma}, \quad Re_f = \frac{\rho_f U_f D_h}{\mu_f} \quad (5.18)$$

with  $A$ ,  $q$ ,  $r$ , and  $s$  given in Table 5.4. They claimed that their proposed correlation covers a wider range of Lockhart Martinelli parameters and Reynolds numbers based on superficial liquid velocity,  $Re_{fo}$ , compared to the correlation that has been proposed by Wambsganss et al. (171)

Saisorn and Wongwises (106) performed a similar study to Lee and Lee (173) but in smaller circular channels with diameters between 0.15mm and 0.53mm. They proposed a modified Chisholm parameter based on data regression analysis on 285 data points:

$$C = 7.599 \times 10^{-3} \lambda^{-0.631} \psi^{0.005} Re_f^{-0.008} \quad (5.19)$$

Because the exponent of the Reynolds number in their proposed correlation was small, they argued that the  $C$  parameter does not strongly depend on the superficial liquid velocity.

Sun and Mishima (167) compared different correlations and models that predict the two-phase flow frictional pressure drop (129, 135, 145, 160, 165, 166, 170, 173, 178). They used data points for different fluids passing through channels with hydraulic diameters ranging from 0.506mm to 12mm. Among the different models they eval-

uated, the Lockhart-Martinelli method (129), Mishima and Hibiki correlation (170), and Lee and Mudawar correlation (160) were found to give the best pressure drop predictions. For the turbulent region, the Müller-Steinhagen and Heck correlation (166) was found to provide the best prediction of the two-phase flow frictional pressure drop. They also proposed modified Chisholm parameters for both laminar and turbulent flows. For laminar flow, they noticed that the Chisholm parameter depends on the Laplace number as well as the Reynolds number:

$$C = 26 \left( 1 + \frac{Re_f}{1000} \right) \left[ 1 - \exp \left( \frac{-0.153}{0.27 \times La + 0.8} \right) \right] \quad (5.20)$$

where  $La$  is the Laplace number and is defined as:

$$La = \frac{\left( \frac{\sigma}{g(\rho_f - \rho_g)} \right)^{0.5}}{D} \quad (5.21)$$

For turbulent flow, they proposed a modified Lockhart-Martinelli correlation as well as a modified Chisholm parameter as a function of  $Re_f$ ,  $Re_g$ , and quality,  $x$ :

$$\phi_f^2 = 1 + \frac{C}{X^{1.19}} + \frac{1}{X^2} \quad (5.22)$$

$$C = 1.79 \left( \frac{Re_g}{Re_f} \right)^{0.4} \left( \frac{1-x}{x} \right)^{0.5} \quad (5.23)$$

So far, the two-phase flow pressure drop is reviewed for general applications. The literature review presented here indicates that most of the efforts done in predicting the two-phase pressure drop based on the separated flow model has been achieved by modifying the Chisholm parameter for a better fit of the results. The applications of the two-phase flow spans a wide range of working conditions. An accurate knowledge

of the two-phase flow pressure drop can be obtained by identifying the working condition of each particular application separately. In Section 5.5, the two-phase flow pressure drop is studied for PEM fuel cell applications. The section reviews the effect of different working conditions of a PEM fuel cell on the two-phase flow pressure drop within the channels.

## 5.5 Pressure Drop with PEM Fuel Cell Application

In this section, the two-phase flow pressure drop in PEM fuel cell flow channels is reviewed. The two-phase flow in PEM fuel cells has some unique characteristics, such as small length scales, a special liquid water introduction mechanism into the gas channel, and different surface energies of the channel walls. The small length scale of PEM fuel cell gas channels diminishes the effects of gravity on the two-phase flow and makes the surface tension effects more dominant. This is different from macro-scale channels where gravity has a dominant effect on the two-phase flow. Furthermore, in PEM fuel cells, liquid water is continuously produced in the catalyst layer and is introduced into the gas channel through the porous GDL. The water emergence from the surface of the GDL within the gas channel occurs at preferential locations. This water introduction mechanism is different from what happens in conventional channels where the two phases are usually introduced and mixed at the inlet of the channel. Moreover, the two-phase flow in PEM fuel cells occurs in channels with GDL as one of the walls and graphite or metal as the other three walls. This yields different surface characteristics of the walls that bind the two-phase flow in PEM fuel cells. Also the channel corners may affect the water transport mechanism if the Concus-Finn condition is met (179). Finally, the non-uniform GDL intrusion into the gas channels may affect the two-phase flow pressure drop in PEM fuel cell gas

channels. Because the cell compression is not uniform in the plane of the flow field, the GDL intrusion into the gas channel will not be also uniform. The GDL intrusion near the edges of the flow field is greater than the GDL intrusion in the central region of the cell. This leads to a higher pressure drop in the side channels compared to the interior channels and therefore results in a nonuniform pressure drop over the flow channels.

In this section, the effect of different PEM fuel cell working conditions on the two-phase flow pressure drop in fuel cell gas channels is reviewed. Pressure drop hysteresis, defined as the pressure drop while the gas flow rate is increased and then decreased, is also discussed. The section ends with reviewing the models that have been proposed for predicting the two-phase flow pressure drop in PEM fuel cell gas channels. Table 5.5 lists the literature that has studied the two-phase flow pressure drop in PEM fuel cell gas channels.



Table 5.5: Literatures studying the pressure drop in PEM fuel cells

Author	Area of Focus	Experiment Type	Major Conclusion
Rodatz (180)	Fuel cell stack operation	in situ	The pressure drop is observed to decrease with the cell's current density.
Barbir (181)	The flooding and drying phenomenon in PEM fuel cell	in situ	Flooding or drying can be diagnosed by monitoring the pressure drop and resistance simultaneously.
Trabold (122)	Liquid water accumulation	in situ	Pressure drop has been employed as a diagnostic tool to study the water accumulation. While the pressure drop was observed to significantly increase in the cathode, it has been observed that it slightly changes in the anode.
Allen (182)	The role of capillary on two phase flow	ex situ	Pressure drop is used to describe flow patterns.
English (20)	Two phase flow pressure drop in PEM fuel cell	ex situ	A pressure drop correlation based on LM method is proposed.
Ma (183)	Liquid water accumulation in cathode	in situ	The pressure drop results can be used to determine the proper gas velocity required to remove liquid water.
Yamada (184)	The location and magnitude of electrode flooding	in situ	The pressure drop measured during flow field switch from parallel to interdigitated indicates the level of GDL flooding.
Ge (79)	Water formation and transport in anode	in situ	Anode pressure drop is used to evaluate water transport between anode and cathode during the operation of the cell.
Liu (8)	Liquid water accumulation	in situ	The existence of water is found to be the main reason of pressure drop in the flow channels.
Liu (185)	Design flow channels with effective water removal	in situ	Pressure drop is used to design flow channels with effective water removal.
Zhang (15)	Two-phase flow in parallel gas channels of PEM fuel cell	ex situ	A negative slope in pressure drop vs. superficial gas velocity indicates a flow pattern change from a non-uniform to an uniform pattern.
Ito (186)	Water saturation in GDL	in situ	The differential pressure drop between the inlet and outlet of an interdigitated cell can be used to estimate the level of water saturation within the GDL.
Zhang (16)	Two phase flow in parallel square minichannels at different orientation	ex situ	Pressure drop increases with the inclination angle.

Table 5.5, continue: Literatures studying the pressure drop in PEM fuel cells

Reference	Area of Focus	Experiment Type	Major Conclusion
Kandlikar (187)	GDL intrusion due to the cell compression	ex situ	The GDL intrusion should be considered.
Hussaini (13)	Cathode flooding of an operating cell working at different relative humidities, current densities, and flow stoichiometries	in situ	Two phase flow pressure drop is utilized as a diagnostic tool that describes the amount of liquid water in gas channel.
Lu (6)	Two phase flow in gas channels for different air and water flow rates	ex situ	A large fluctuation in the pressure drop is noted for the slug flow, moderate oscillation for film flow and minimal fluctuation for mist flow.
Yu (188)	Two-phase flow pressure drop profiles for different flow patterns in anode	ex situ	The pressure drop results indicate that the annular purge is more appropriate for removing liquid water in anode.
Hsieh (189)	Cathode pressure drop of PEM fuel cell with four different flow fields	in situ	The interdigitated flow channel yields the highest pressure drop compared to serpentine, parallel and mesh configuration.
Grimm (7)	Two phase flow in channel bounded with GDL	ex situ	Correlations were proposed for slug, film and mist flow.
Kandlikar (124)	The flow maldistribution in individual channels along the entrance region	in situ/ex situ	A new technique is proposed to calculate instantaneous flow in each channel based on the measured pressure drop.
Akhtar (10)	Water transport mechanism in different channel geometries	ex situ	The pressure drop is used to define the optimum channel geometry in terms of liquid water removal.
Chen (123)	Two phase flow in PEM fuel cell parallel channels with porous media insert	ex situ	The porous insert causes a four-fold pressure drop compared to hollow channels.
Chen (190)	liquid water removal characteristics in parallel channels	ex situ	The dominant frequency of the pressure drop may be used as a diagnostic tool for water removal.
Anderson (11)	The effects of flow stoichiometry, GDL properties, and the initial water balance in gas channel on the two-phase flow pressure drop hysteresis	ex situ	Two phase flow pressure drop hysteresis disappears at stoichiometries of 5 and higher. Initial water balance affects the hysteresis pattern.
Anderson (191)	Two-phase flow pressure drop hysteresis for different temperatures, air stoichiometries, and GDL	ex situ	The pressure drop hysteresis becomes less significant at higher temperatures.
Dillet (192)	The water droplet appearance and transport in the gas channel	in situ	Clogging and unclogging can be detected by monitoring the pressure drop and cell voltage simultaneously.

Table 5.5, continue: Literatures studying the pressure drop in PEM fuel cells

Reference	Area of Focus	Experiment Type	Major Conclusion
Spernjak (193)	Water accumulation in different flow field	in situ	Monitoring the pressure drop, current density, and water volume simultaneously can be used to identify three stages of water evolution.
Lu (12)	Effect of channel surface wettability, cross-sectional geometry and orientation on the two-phase flow in parallel gas channels	ex situ	Sinusoidal channel results in lower pressure drop than rectangular and trapezoidal. Hydrophilic channel surface has lower two phase flow multiplier at lower superficial gas velocity.
Blanco (14)	The use of a perforated stainless steel sheet as an additional layer in cathode to improve water transport at dry condition	in situ	Pressure drop is used to evaluate water transport between anode and cathode.
Colosqui (194)	Droplet growth, detachment, and transport	ex situ	Monitoring the pressure drop over time is used to describe drop and slug formation.
Zhang (18)	Two phase flow in gas channel with GDL as one of the walls	ex situ	A pressure drop correlation based on LM method is proposed.
Anderson (17)	Two phase flow pressure drop hysteresis at different air stoichiometry, temperature, and inclusion of MPL	in situ	The modified LM approach given in (18) can predict the two-phase flow pressure drop in an ascending approach.
Radhakrishnan (195)	The pressure drop in parallel and serpentine flow field for GDLs with different compressions	ex situ	While GDL compression does not change the pressure drop significantly in parallel flow field, it causes a significant pressure drop increase in serpentine flow field.
Jiao (196)	The effects of the start-up temperature and load condition on the cold start of PEM fuel cell	in situ	The ice blockage in flow channel and GDL leads to a significant pressure drop through cathode flow field.
Taccani (197)	The effect of flow field geometry of high temperature benzimidazole PEM fuel cell on the overall performance	in situ	The serpentine flow field results in higher pressure drop than the parallel flow field.
Bachman (198)	The effect of channel length on cell performance for serpentine flow field	in situ	Although longer gas channel exhibit larger pressure drop, it shows a more stable cell performance compared to shorter channels.

### 5.5.1 Two-phase flow pressure drop for different flow patterns in PEM fuel cell

Different from single-phase flow in which each flow rate results in a specific pressure drop, a particular two-phase pressure drop can be obtained from different combinations of liquid and gas flow rates. The two-phase pressure drop can be correlated to the flow pattern within the gas channel. Grimm et al. (7) studied the two-phase flow pressure drop in a simulated PEM fuel cell gas channel by providing air and water at different flow rates corresponding to slug flow, film flow and mist flow. Figure 4 shows the pressure drop they measured at different flow patterns. The two-phase flow pressure drop of slug flow contains large spikes that repeat with long time intervals. Each spike of the pressure drop profile represents the formation of a slug in the gas channel. As the slug forms, the channel cross section decreases and the pressure drop increases until the pressure can provide enough force to remove the slug from the channel. Increasing the air flow rate to film flow and ultimately mist flow makes the pressure drop spikes shorter. The minimal oscillation of the pressure drop profile can be observed in mist flow. This is due to the large gas to liquid ratio that makes the mist flow behave similarly to single-phase flow. Similar pressure drop profiles for these two-phase flow patterns have been reported in other studies (6, 18).

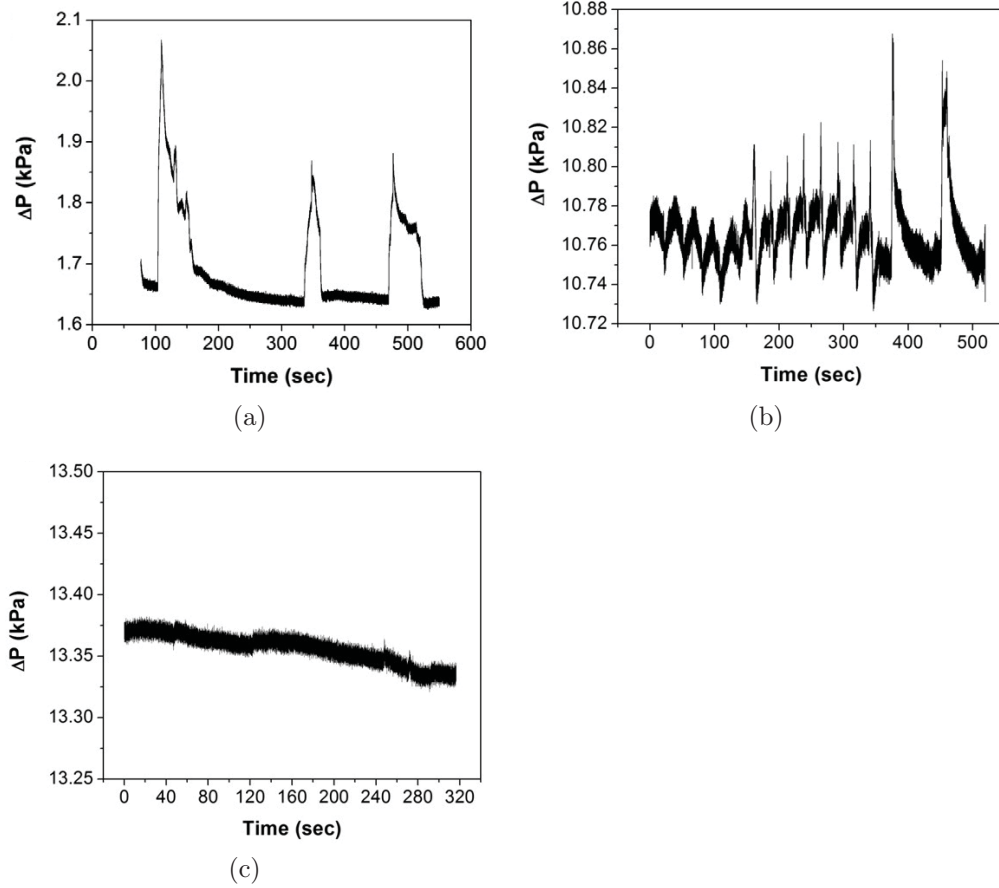


Figure 5.4: The two-phase flow pressure drop signature reported by Grimm et al. (7): (a) spikes in pressure drop signature due to slug formation for water flow rate of  $0.1\text{mlmin}^{-1}$  and air flow rate of 330 sccm, (b) fluctuation in pressure drop due to film flow for water flow rate of  $0.04\text{mlmin}^{-1}$  and air flow rate of 1981 sccm, (c) pressure drop signature for mist flow for water flow rate of  $0.02\text{mlmin}^{-1}$  and air flow rate of 2311 sccm.

### 5.5.2 Two-phase flow pressure drop and cell performance

The pressure drop can be considered as a diagnostic tool that describes the amount of accumulated liquid water within the gas channel. Liquid water can accumulate inside the gas channel when the water production rate is greater than the water removal rate. The accumulated liquid water blocks the transport of the reactants and consequently lowers the performance of the cell. The accumulated water in the gas channel also causes a pressure drop by resisting the gas flow. Liu et al. (8) used a transparent cell and studied the water flooding in gas channels by simultaneously monitoring the cell performance and the cathode and anode pressure drop, as shown in Figure 5. It can be observed from the figure that the cell performance degradation is accompanied by an increase in the cathode pressure drop. This observation has been reported to be an indication of the liquid water accumulating within the gas channels. Another remarkable observation of this study is the higher pressure drop of the cathode compared to the anode. The amount of water produced in the cathode is much greater than the water accumulated in the anode, either by water condensation in the humidified anode gas or back diffusion of water from the cathode to the anode. Dillet et al. (192) performed an in-situ test and measured the pressure drop and cell voltage in a single channel segmented fuel cell. They were able to define the channel clogging and unclogging sequences by analyzing the simultaneous records of the pressure drop and the cell voltage.

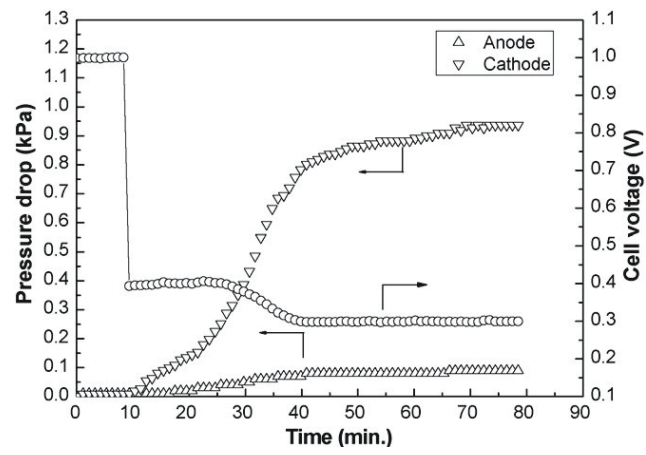


Figure 5.5: Cell performance and the cathode and anode pressure drop reported by Liu et al. (8) Parallel gas flow field fuel cell operating at 25°C and 69.6mlmin<sup>-1</sup> oxygen flow rate and 139.3mlmin<sup>-1</sup> hydrogen flow rate.

### 5.5.3 Effect of flow field geometry on the two-phase flow pressure drop

Flow field geometry has been known to have a significant impact on the mass transport of the reactants and products, as well as the pressure drop between the inlet and the outlet of the flow channels (9). An appropriate flow channel design has been mentioned to be the most successful strategy in addressing water flooding issues (68). Flow field geometry also impacts the current distribution and the cell performance (199). A comprehensive review of the flow field design has been done by Li and Sabir (199). The common flow field designs for PEM fuel cells include parallel channels, serpentine flow field, and interdigitated flow field (200–202). In a parallel flow field, straight parallel channels connect the inlet and outlet headers. Parallel flow fields may suffer from unequal liquid water distributions within the channels. In this situation, the low pressure drop cannot remove water slug from the gas channels (200, 201). This can lead to flow mal-distribution that will ultimately cause reactant starvation in some channels and excess reactants in other channels. The serpentine flow field is made of one or more long channels that pass through the whole bipolar plate via several bends. These bends cause a relatively high pressure drop that can facilitate water removal from the channels. Despite parallel and serpentine flow channels that connect the inlet header to the outlet header, an interdigitated flow field design includes channels that are connected into either inlet or outlet headers. In this type of flow field, reactants penetrate into the porous GDL and permeate through to reach the outlet channels. This induces a large pressure drop which facilitates water removal from the porous GDL. Although the improved water removal in an interdigitated flow field makes it an ideal type of flow field for high current densities, its high pressure drop characteristic results in an increased parasitic power within the system.



Spernjak et al. (193) studied the effect of the flow field design on the cell performance and the two-phase flow pressure drop in anode and cathode. While the serpentine flow field was reported to result in a higher limiting current density compared to a parallel and interdigitated flow field, it has been argued that serpentine flow field configuration exhibits a substantially higher pressure drop compared to parallel and interdigitated flow fields. Similar results have been reported by Tacconi and Zuliani (197) as they studied the effect of the flow field geometry on the overall performance of polybenzimidazole PEM fuel cells working at a higher temperature range ( $120^{\circ}\text{C} - 180^{\circ}\text{C}$ ).

Hsieh et al. (9) measured the pressure drop of PEM fuel cells with four different flow fields. The pressure drops have been measured in interdigitated, serpentine, parallel, and mesh flow fields with an active area of  $22.5\text{ mm} \times 22.5\text{ mm}$  when each cell was operating with 60sccm air flow rate. Figure 6 shows the pressure drop they measured during 180min operation of the cell. The figure shows that the maximum pressure drop occurs in the cell with an interdigitated flow field and the minimum pressure drop occurs in the mesh flow channel. The figure also shows that the pressure drop of the serpentine flow field is higher than the pressure drop of the parallel flow field. Other than the flow field design, channel geometry also impacts the performance of the cell as well as the liquid water transport mechanism. Owejan et al. (90) used neutron radiography to acquire liquid water distribution in operating fuel cells with different cross-sectional geometries. They used triangular and rectangular channels with the same cross-sectional areas and noticed that triangular channels retain less water compared to rectangular channels. The effects of the gas channel length, width, depth, and rib size on the two-phase flow pressure drop have also been the subject of several studies (10, 12, 198).

Akhtar et al. (10) studied the minimum pressure drop required to remove a conden-

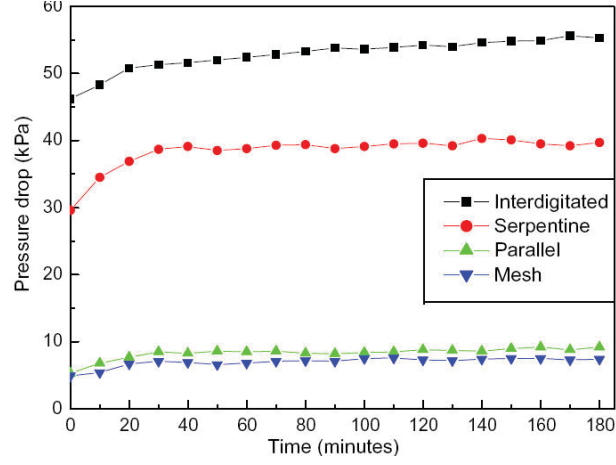


Figure 5.6: Pressure drop measured in different flow fields reported by Hsieh et al. (9)

sate from gas channels with different cross-sectional geometries, as shown in Figure 7. They found that the minimum pressure drop that can transport the droplet depends on the normalized droplet volume. The normalized droplet volume was defined as the channel filling droplet of 1mm in length. For small droplets with normalized volume less than 1, the pressure drop was observed to decrease as the normalized water droplet volume increased, as shown in Figure 8. The figure suggests that a small amount of liquid water (normalized volume of less than 1) can be efficiently removed in a wide channel (R1 and R3). For larger drops with a normalized droplet volume of greater than 1 (not shown), it was reported that the pressure drop remains nearly constant for different normalized volumes and for each cross section. However, the minimum pressure drop required to remove drops was reported to be maximum for cross section R4 and minimal for cross section R1.

Lu et al. (12) studied the effect of channel cross-sectional geometry on the two-phase flow properties in parallel gas channels. They tested three different cross-sectional geometries, rectangular, sinusoidal, and trapezoidal and observed that the sinusoidal channel causes the lowest two-phase flow frictional multiplier,  $\phi_g^2$ . They also compared

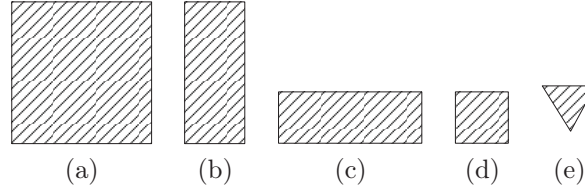


Figure 5.7: Cross-sectional geometries of the gas channels that were considered by Akhtar et al. (10) (a) R1, 1mm  $\times$  1mm, (b) R2, 0.5mm  $\times$  1mm, (c) R3, 1mm  $\times$  0.5mm, (d) R5, 0.5mm  $\times$  0.5mm, and (e) V1, 0.5mm and 53°

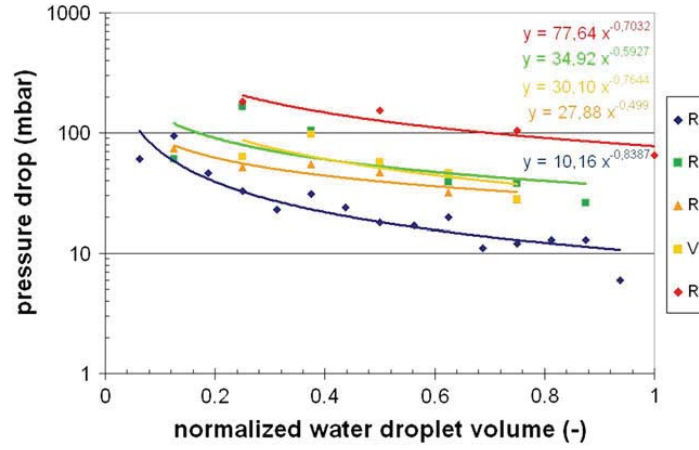


Figure 5.8: Minimum pressure drop required for drop removal reported by Akhtar et al. (10)

flow images for different channel geometries and noticed that the flow pattern in the sinusoidal channel is characterized by multiple small slugs rather than fewer long slugs as can be observed in rectangular and trapezoidal channels. Moreover, a more uniform water distribution was reported within sinusoidal channels compared to rectangular and trapezoidal channels.

The other geometrical parameter that also impacts the pressure drop is the channel length. Bachman et al. (198) measured the cell output and the pressure drop of parallel flow channels with different lengths of 5cm, 15cm, and 25cm. It has been reported that although longer channels suffer from a higher pressure drop, they can

improve the performance of the cell. The cell with a 5cm gas channel exhibited an erratic and unstable performance, while the cell with a 25cm gas channel had a stable output. The unsteady and high accumulation of water within the 5cm channel has been mentioned to be the main reason of its low and unstable performance.

Channel corner angle can also impact water transport within the gas channel. According to Concus-Finn criteria, if the droplet static contact angle,  $\theta$ , be smaller than  $\pi/2 - \alpha$ , where  $\alpha$  is the half-angle of the channel cross-sectional corner, liquid water can wick into the channel corner and transport along the corner within the gas channel. Rath and Kandlikar (2003) utilized the Concus-Finn condition to determine the corner angle at which a water droplet can fill the corner. The corner is made of 2 surfaces, the GDL and the surface channel, each with different surface energies. It has been reported that the GDL corners do not fill when the corner angle is less than  $52^\circ$ .

#### 5.5.4 Effect of gas stoichiometry on the two-phase flow pressure drop

The stoichiometry ratio describes the ratio of the supplied reactant flow to the reactant consumption rate. The concentration loss caused by water flooding can be avoided, in part, by increasing the stoichiometric ratio. Flow stoichiometry can also convectively remove water from the gas channel (17). While a high stoichiometry may be helpful in increasing the mass transport rate of reactants and avoiding the flooding, an excess stoichiometry, on the other hand, can cause some major disadvantages. Some common problems caused by high stoichiometries are membrane dehydration and decreased reactant utilization (32, 204). Ous and Arcoumanis (205) studied the effect of different air and hydrogen stoichiometries on the accumulation of water in the cathode and anode of a transparent PEM fuel cell. It has been reported that an increased air stoichiometry is capable of removing all of the liquid water from the cathode channels without causing membrane dehydration. However, elevated hydrogen stoichiometries were mentioned to be incapable of removing liquid water from inside the cell.

Lu et. al. (6) studied the two-phase flow in PEM fuel cell parallel flow channels for different air stoichiometries and noticed that air stoichiometries of less than 5 typically yield slug flow with large pressure drop fluctuation. Higher stoichiometries were reported to cause film flow with water film forming on hydrophilic channels. The pressure profile of film flow was characterized by smaller but more frequent fluctuations compared to slug flow. Further increase in the stoichiometry ratio was reported to result in mist flow with less water being accumulated within the flow channels and therefore minimal pressure oscillation.

Anderson et al. (11) studied the effect of the flow stoichiometry on the two-phase flow

pressure drop in a non-operating PEM fuel cell. Figure 9 shows the pressure drop they measured for different stoichiometries and for ascending and descending approaches. Ascending describes an increasing gas flow rate and descending describes a decreasing gas flow rate. Further discussion of the differences between ascending and descending results is given in section 5.5.8 where pressure drop hysteresis is reviewed. Figure 9 shows that increasing the stoichiometry ratio increases the pressure drop for each simulated current density. This originates from the pressure drop being proportional to the gas flow rate. A Similar trend in pressure drop has been reported by Lin and Nguyen (32) as they studied water flooding in PEM fuel cells for different GDLs and at different stoichiometries.

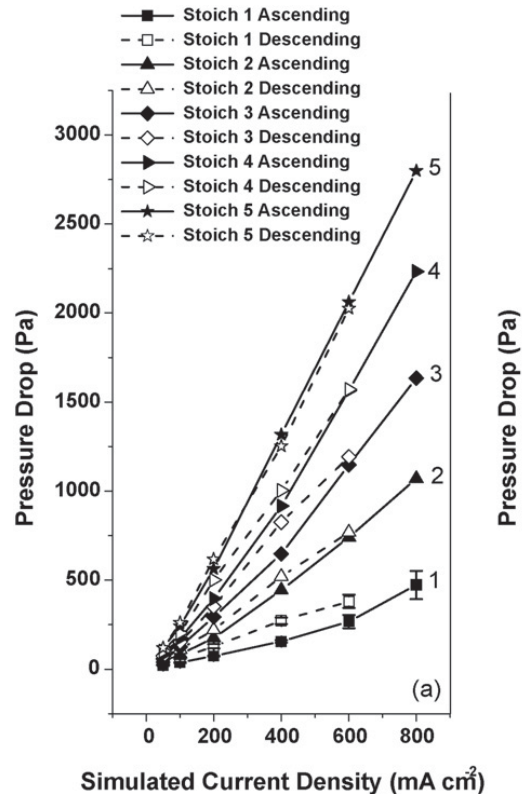


Figure 5.9: Effect of the gas stoichiometry on the pressure drop reported by Anderson et al. (11)

Hussaini and Wang (13) calculated the two-phase flow frictional multiplier,  $\phi$ , for

different flow stoichiometries and noticed that increasing the flow stoichiometry decreases the two-phase flow frictional multiplier. This can be interpreted as more water being removed from inside the gas channel as the stoichiometry increases.

### 5.5.5 Effect of wettability on the two-phase flow pressure drop

Liquid water behavior on a solid surface is characterized by the surface wettability. While water spreads on hydrophilic surfaces, which are defined as the surfaces with contact angles less than  $90^\circ$ , it beads up on hydrophobic surfaces that make contact angles of greater than  $90^\circ$ . Surface wettability also affects the water transport mechanism. For a hydrophilic channel with the Concus-Finn condition being satisfied (179), liquid water wicks into the corner and drains via capillary flow. However, for a hydrophobic channel, water pins on the surface and forms slugs. A similar behavior of water droplets can be observed on the GDL surface. A water droplet can be detached from the GDL surface only if the shear gas flow can provide the required drag force to exceed the surface adhesion force (5). The drag force applied on the droplet from the core gas flow depends on the projected area of the droplet and consequently depends on the droplet contact angle on the surface of the GDL.

Lu et al. (12) studied the effect of channel surface wettability on the two-phase flow in parallel gas channels. Figure 10 shows the two phase flow frictional multiplier,  $\phi_g^2$ , at different superficial liquid and gas velocities. The figure shows a lower  $\phi_g^2$  for a hydrophilic channel with lower water flow rate (left plot) and a higher  $\phi_g^2$  for a hydrophilic channel with higher water flow rate (right plot). The former was explained by the more uniform distribution of water within the gas channel, and the latter was explained by water film flow as the consequence of the Concus-Finn condition being met. Finally they concluded that although hydrophilic channels can cause certain water accumulation within the flow channels, they are still the superior channel surface treatment in terms of flow distribution compared to uncoated and hydrophobic channels.

GDL wettability has been reported to impact water condensation at low current den-



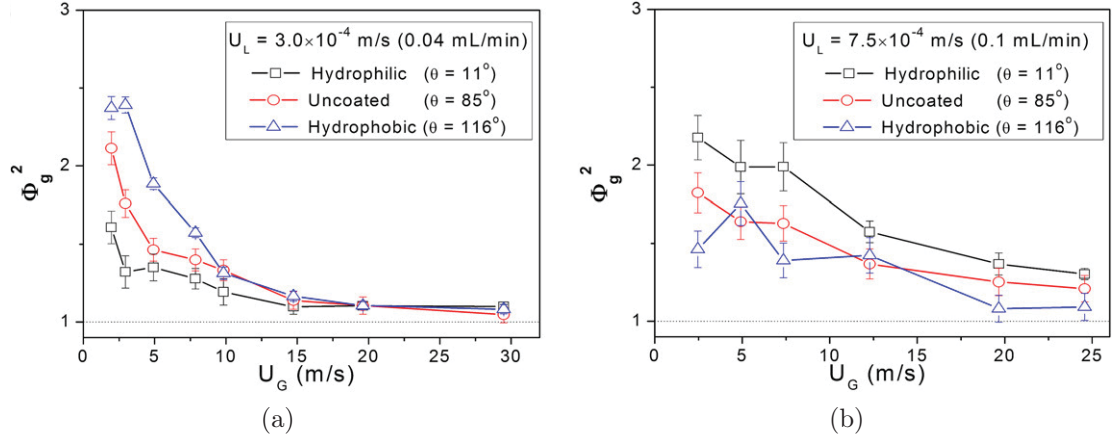


Figure 5.10: Effect of channel wall surface energy on the two-phase flow frictional multiplier reported by Lu et al. (12). (a)  $j_f = 3.0 \times 10^{-4} \text{ m/s}$ , (b)  $j_f = 7.5 \times 10^{-4} \text{ m/s}$ . The horizontal axis,  $U_G$ , is the superficial gas velocity.

sities. Ge and Wang (79) studied liquid water formation and transport in PEM fuel cells with hydrophobic and untreated GDL by comparing the pressure drop and the performance of the cell running at  $0.2 \text{ A cm}^{-2}$ . It has been reported that for a hydrophobic GDL, water is more prone to condense on the surface of the channel rather than inside the hydrophobic pores of the GDL. The accumulation of the condensed water on the surface of the hydrophobic GDL causes channel flooding with the anode pressure drop being increased. Channel flooding has reported to be eliminated by replacing the hydrophobic GDL with an untreated one. In contrast to the anode pressure drop for hydrophobic GDL, where the pressure continuously increased, the anode pressure drop for untreated GDL was reported to remain almost constant. This suggests a sharp difference between the water distribution at a low current density in the anode with hydrophobic GDL versus the anode with untreated GDL.

While Lu et al. (12) and Ge and Wang (79) reported that the surface characteristics of the GDL and channel walls can impact the pressure drop, Grimm et al. (7) has discussed that the channel surface characteristic does not affect the two-phase flow

pressure drop in PEM fuel cell flow channels. They studied the two-phase flow in the gas channels of a PEM fuel cell in an ex-situ setup that included GDL as one of the sidewalls. They used three channel treatments of hydrophobic, hydrophilic, and untreated, with contact angles of  $116^\circ$ ,  $11^\circ$ , and  $86^\circ$ , respectively, and recorded the pressure drop along the flow channels. The effect of channel surface energy on the pressure drop was mentioned to be negligible in their studies.

### 5.5.6 Effect of temperature on the two-phase flow pressure drop

One of the most important parameters that can significantly affect the water content within the PEM fuel cell flow channels is the temperature of the cell. The neutron imaging studies conducted by Hickner et al. (206), and Owejan et al. (207) and direct visualization experiments performed by Liu et al. (208) report that the water content in PEM fuel cell flow channels decreases as the temperature of the cell increases. An increased temperature has been reported to decrease the condensation of liquid water (208) and increase the convective water removal capacity of the gases supplied within the flow channels (17). Although an elevated cell temperature enhances the kinetics of the electrochemical reaction, which results in more water being produced during the operation of the cell, the enhanced water removal capacity of the reactant has a more dominant impact on water balance within the cell (208).

Ous and Arcoumanis (205) studied the accumulation of liquid water in serpentine flow channels of a transparent PEM fuel cell working at different temperatures between 30°C and 60°C. They noticed that a cell temperature of 60°C is capable of evaporating all of the liquid water in the channels and enhancing the performance of the cell. The images taken from flow channels showed that the amount of liquid water decreased as the temperature was increased. A temperature of 60°C was mentioned to result in minimal water content within the cell and an improved performance of the cell. However, an elevated cell temperature may not always be desirable as it may cause membrane dehydration during the operation of the cell (209, 210).

Liu et al. (8) studied the effect of temperature on the liquid water accumulation and two-phase flow pressure drop in an operating cell. They ran a transparent PEM fuel cell at temperatures between 25°C and 75°C and observed that the amount of

liquid water within parallel flow channels decreases by increasing the temperature. The two-phase flow pressure drop measurements in their study, as shown in Figure 11, revealed that while the two-phase flow pressure drop in the cathode decreases in elevated temperatures, the anode pressure drop shows no sign of variation. The latter has been justified by increased evaporation of the accumulated water while the former was explained based on the few amount of accumulated water within anode flow channels.

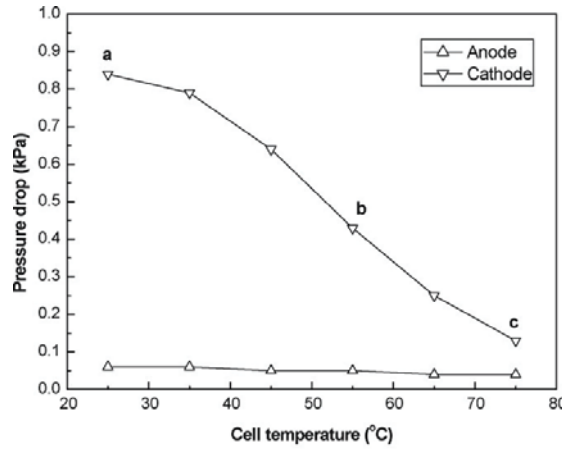


Figure 5.11: Effect of temperature on two-phase flow pressure drop reported by Liu et al. (8)

Yan et al. (211) measured the two-phase flow pressure drop in anode and cathode of a PEM fuel cell with a serpentine flow field that operated at different cell and humidification temperatures. It has been reported that for a constant cell temperature, increasing the cathode and/or anode humidification temperature increases the two-phase flow pressure drop in both electrode flow channels. Increasing the humidification temperature increases the water vapor in the reactants, and therefore, more water vapor will enter the cell flow channel to be condensed. Similar to the findings presented by Liu et al. (8), the variation of the cathode pressure drop was more dominant compared to the variation of the anode pressure drop.

Anderson et al. (17) studied the two-phase flow pressure drop in an operating PEM fuel cell at different temperatures by calculating the two-phase flow multiplier for ascending and descending gas supply. They reported that temperature has negligible impact on the two-phase flow frictional multiplier in the ascending approach. However, the two-phase flow multiplier was mentioned to be decreasing as the temperature was increased in the descending approach. Such observations have been explained by the amount of liquid water that accumulates in the gas channel in ascending and descending approaches. Because water accumulation is not significant in the ascending approach, increasing the temperature impacts the water content within the flow channels and therefore the frictional multiplier does not change with the temperature. However, the considerable amount of liquid water accumulated in the descending approach can evaporate at higher temperatures and therefore the frictional multiplier decreases as the temperature increases.

The temperature of the cell and the reactant temperature determine the relative humidity of the anode and cathode flow channels. Convective water removal from flow channels depends on the relative humidity. A reactant flow with a low relative humidity has more capability to remove liquid water via evaporation. Cathode flooding can be partially mitigated at lower relative humidities with an improved cell performance (56, 212, 213).

The effect of relative humidity on the cathode pressure drop has been studied by Hussaini and Wang (13) with the results shown in Figure 12. The general trend suggests that the frictional multiplier increases with the relative humidity. This is because of the reduced evaporation rate of the water produced at higher relative humidities. It can also be observed that the effect of the relative humidity on the pressure drop becomes more significant at lower current densities. For instance for 26% relative humidity,  $0.2\text{A cm}^{-2}$  current density, and flow stoichiometry of 4, the

frictional multiplier is 1. However, the frictional multiplier increases up to 3.5 for the same flow stoichiometry but for 66% relative humidity. This large variation in the frictional multiplier is because of the low air flow rate at a low current density which is not capable of removing the condensates either by convective evaporation or inertia effects.

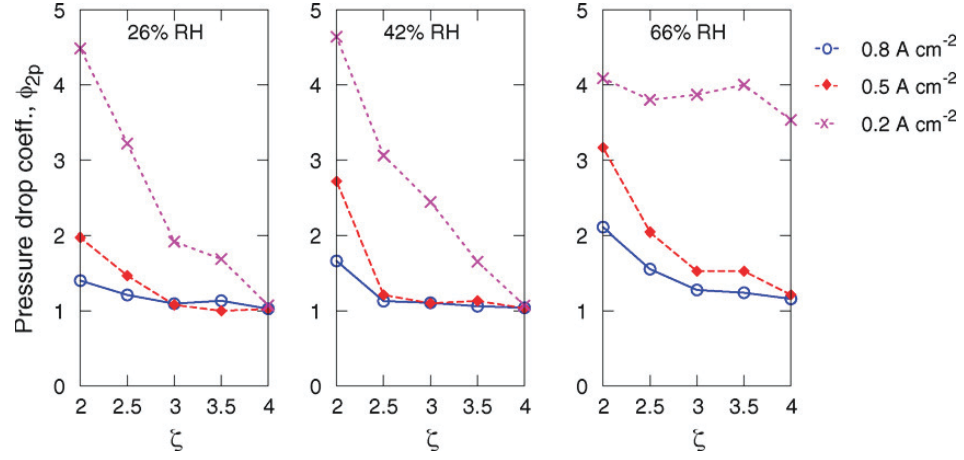


Figure 5.12: Effect of the relative humidity on the two-phase flow frictional multiplier reported by Hussaini and Wang (13)

### 5.5.7 Effect of MPL on the two-phase flow pressure drop

The micro-porous layer (MPL) that covers the surface of the GDL has a significant impact on transport phenomena in GDL-MPL assembly (214). MPL is typically carbon powder-bound with a hydrophobic agent such as PTFE and has different microstructural properties compared to GDL (41, 214). The smallest length scale of MPL compared to other PEM fuel cell components suggests that MPL has a significant impact on the mass transport overpotentials (215, 216). Different hypotheses have been proposed to describe the role of MPL on the water transport within the cell. Some studies argue that coating a GDL with an MPL facilitates water transport from the catalyst layer to the GDL because of the pore size gradient (35, 61, 62). Some studies report that cathode MPL enhances the back diffusion of water from the cathode to anode (27, 32, 63) and others conclude that the MPL has no impact on the back diffusion of water (64–67).

Blanco et al. (14) studied the effect of MPL in the cathode GDL on the pressure drop measured in the anode and cathode of an operating PEM fuel cell. They measured the two phase flow pressure drop for the anode and cathode when the cell was operating at 25% and 100% relative humidities. Separate experiments were run for the cathode GDL with and without MPL. Figure 13 shows the variation of cathode and anode pressure drops at different current densities. It can be observed that for current densities above  $1000\text{mA cm}^{-2}$ , the cathode pressure drop of GDL without MPL (25BA) is greater than the cathode pressure drop for a GDL with MPL (25BC). This has been attributed to a lower amount of accumulated water in the cathode flow channels when MPL was used. In contrast to the cathode in which a GDL without MPL resulted in a higher pressure drop, a GDL without MPL in the anode was observed to cause a lower pressure drop. Such observations can be considered the support of

the hypothesis suggesting that MPL impacts water crossover from the cathode to the anode.

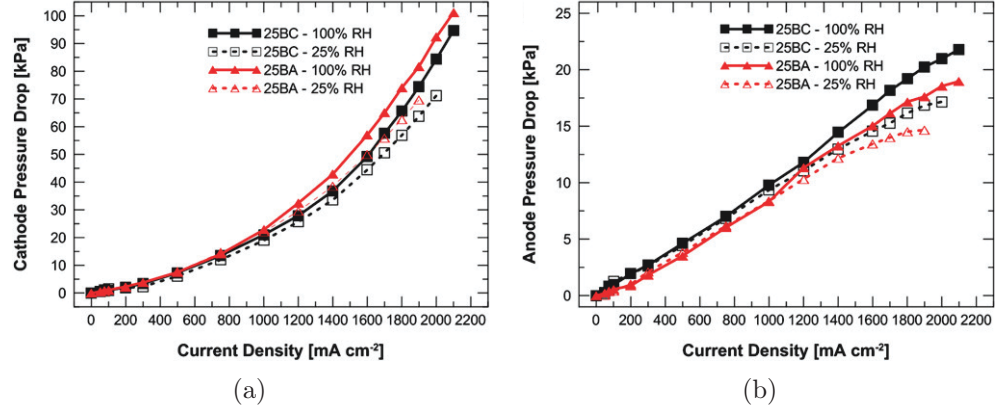


Figure 5.13: Effect of MPL on the (a) cathode and (b) anode pressure drop reported by Blanco et al. (14). 25BA refers to SGL 25BA (GDL without MPL) and 25BC refers to SGL 25BC (GDL with MPL).



### 5.5.8 Hysteresis effects in two-phase flow pressure drop

The two-phase flow pressure drop in PEM fuel cell flow channels can exhibit different values when the current density is increasing and then decreasing. This is referred to as pressure drop hysteresis and has been extensively studied by Wilkinson's research group (11, 15–18, 120, 191). They have studied the effects of different parameters on the two-phase flow pressure drop hysteresis by conducting both in-situ and ex-situ experiments. The parameters they studied include channel outlet configuration (vertical or straight-through) (15), the initial water balance condition in the gas channel (11, 15), channel inclination angle (16), flow stoichiometry (11, 17, 191), GDL characteristics (11, 191), temperature (17, 191) and inclusion of microporous layer (17).

Although, as a general trend, the pressure drop increases with the superficial gas velocity, it has been reported that the two-phase pressure drop in PEM fuel cell gas channels does not monotonically increase with superficial gas velocity (15, 16). Instead, the variation of pressure drop based on the gas flow rate exhibits a negative slope for a limited range of gas flow rates, as shown in Figure 14. Such negative slope is reported to correspond to a two-phase flow pattern change from non-uniform distribution to uniform distribution. The pressure drop hysteresis shown in Figure 14 corresponds to both the vertical and horizontal outlet configurations. The exit is vertical when it is perpendicular to the flow channel.

Figure 14 shows the pressure drop decreases at superficial gas velocities between  $0.2\text{ m s}^{-1}$  to  $1.4\text{ m s}^{-1}$  for vertical outlet configuration. Further increase in gas flow rate results in a pressure drop increase and the flow pattern shifts to an even flow distribution. The descending approach shows a lower pressure drop trajectory than the ascending approach. The descending pressure drop trajectory merges with as-

cending pressure drop trajectory at a superficial gas velocity of  $2\text{ m s}^{-1}$ . The figure exhibits a narrower pressure drop hysteresis region for a setup with a straight exit. Furthermore, the negative slope of the pressure drop, which has been known as a sign of transition from non-uniform flow into uniform flow, occurs at a lower pressure for the channel with a straight exit.

The hysteresis region is reported to shrink by increasing the superficial liquid velocity (15, 16). However, the transition pressure drop, defined as the pressure drop at which the flow pattern changes from non-uniform to uniform distribution, remains unchanged for different superficial liquid velocities (15, 16).

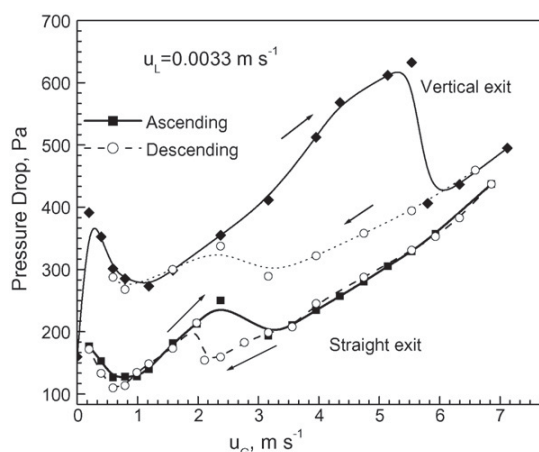


Figure 5.14: Pressure drop hysteresis at  $j_f = 0.0033\text{ ms}^{-1}$  reported by Zhang et al. (15)

Zhang et al. (16) studied the effect of channel inclination angle on the two-phase flow pressure drop hysteresis and observed that the pressure drop increases with the inclination angle, as shown in Figure 15. They tested both positive (upward) and negative (downward) angles and noticed that the pressure drop shows hysteresis effects for upward channels while the hysteresis disappears in downward channels.

In section 5.5.4, the effect of flow stoichiometry on two-phase pressure drop was discussed. The flow stoichiometry also affects the hysteresis zone (11, 17). As shown in

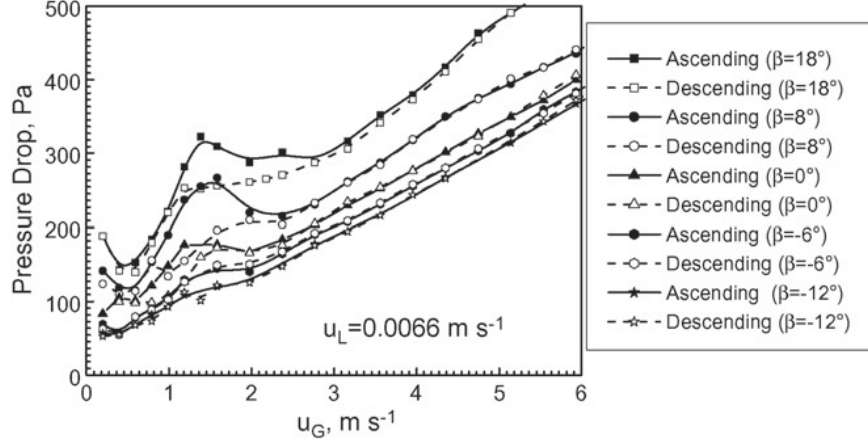


Figure 5.15: Effect of the channel inclination angle,  $\beta$ , on the two-phase flow pressure drop hysteresis reported by Zhang et al. (16)

Figure 9, increasing the stoichiometry narrows the hysteresis region of the pressure drop. The hysteresis region is large for low stoichiometries of 1 to 4. This is because the low gas flow is not capable of removing accumulated water, and therefore, there is a significant difference in the amount of water within the gas channel in ascending and descending approaches. The hysteresis seems to disappear for the flow stoichiometry of 5 in Figure 9. The stoichiometry ratio of 5 is high enough to remove the accumulated liquid water convectively and leave a comparable ascending and descending pressure drop.

MPL also seems to impact the pressure drop hysteresis. Ex-situ studies have shown that the inclusion of an MPL does not affect the descending pressure drop while it increases the ascending pressure drop (11). It has been argued that the GDL with MPL reduces the cross-sectional area of the channel, and therefore, the pressure drop increases. The inclusion of the MPL in GDL is also reported to increase the simulated current density at which the pressure drop hysteresis initiates (11). The in-situ studies, however, report no clear effect of the MPL on the pressure drop hysteresis except for current densities less than  $200 \text{ mA cm}^{-2}$  (17).

The other parameter that can affect the pressure drop hysteresis is the initial water balance in the gas channel. For an initially dry gas channel, the ascending pressure drop is lower than the descending pressure drop. However, the excess water in an initially flooded channel causes a higher ascending pressure drop compared to the descending pressure drop. Also, since some portion of water is removed during the ascending approach, the descending pressure drop will be lower than the ascending pressure drop (11).

The effect of the temperature on the pressure drop hysteresis is studied by Anderson et al. (17, 191), with the results shown in Figure 16. It can be observed from the figure that the pressure drop hysteresis decreases as the temperature increases. The lower pressure drop hysteresis for elevated temperatures originates from an increased water removal capacity of the supplied gas.

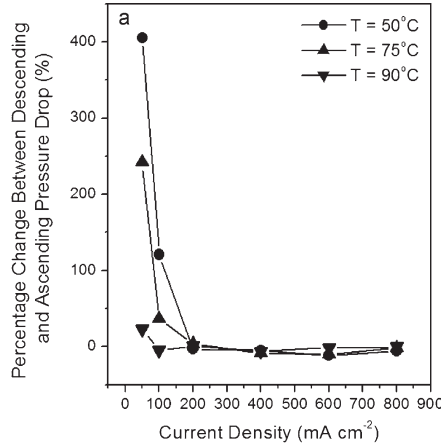


Figure 5.16: Effect of temperature on the pressure drop hysteresis reported by Anderson et al. (17)

## 5.6 Two-phase flow pressure drop models for the application of PEM fuel cell

The single phase internal flow is very well understood in terms of predicting the flow properties such as the pressure drop. The complicated physics behind the two-phase flow, however, has made it difficult to predict the two-phase flow pressure drop. While enormous effort has been expended in predicting the two-phase pressure drop in large scale industrial applications, there are few works focusing on the two-phase flow pressure drop in minichannels. The two-phase flow in PEM fuel cell minichannels is also different from other industrial applications. This is because of the unique water production and introduction as well as different surface energies of the surrounding walls in PEM fuel cell flow channels. These add to the complication of taking an analytical approach to study the subject of the two-phase flow pressure drop in PEM fuel cell flow channels. In this section, the two-phase flow pressure drop models that have been proposed for the application of PEM fuel cell will be reviewed.

As one of the early stage studies done on the two-phase flow pressure drop in PEM fuel cells, English and Kandlikar (20) extended the Mishima and Hibiki model (Equations 5.15 and 5.16) by replacing the turbulent liquid-turbulent gas Chisholm parameter, 21, with a laminar liquid-laminar gas Chisholm parameter, 5. They proposed a modified Chisholm equation that was claimed to result in a better two-phase flow pressure drop prediction:

$$C = 5(1 - e^{-0.319D_h}) \quad (5.24)$$

Zhang et al. (120) noticed that the pressure drop predicted by the homogeneous and separated flow models result in large deviations from the actual pressure drop, espe-

cially at low mass fluxes of PEM fuel cells. They proposed a flow pattern-dependent pressure drop model that is capable of predicting the two-phase pressure drop hysteresis in parallel channels.

In both of the studies mentioned above, the liquid water is directly introduced into a gas channel with all walls from the same material. Zhang et al. (18) focused on liquid-gas two-phase flow in minichannels with GDL as one of the walls. They compared the measured pressure drop with those predicted by the separated flow model and noticed a significant deviation between the results. This led them to modify the Lockhart-Martinelli (LM) method by considering a gradually increasing water flow rate along the gas channel, as shown in Figure 17.

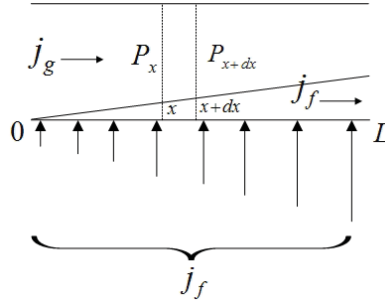


Figure 5.17: Water introduction model considered by Zhang et al. (18)

They assumed that the pressure drop over a small interval follows the LM method. They defined the Martinelli parameter,  $\chi^2$ , based on the local superficial liquid velocity,  $j_{f|_x}$ , which has been obtained by modeling the water transport through the porous GDL based on Darcy's law.

$$P_x - P_{x+dx} = \phi_g^2 \Delta P_g dx = (1 + C\chi + \chi^2)_x \Delta P_g dx \quad (5.25)$$

$$\chi^2|_x = \frac{j_{f|_x} \mu_f}{j_g \mu_g} \quad (5.26)$$

Substituting Equation 5.26 into Equation 5.25 yields:

$$\frac{dP}{dx} = \Delta P_g \left( 1 + C \left( \frac{\dot{j}_f|_x \mu_f}{\dot{j}_g \mu_g} \right)^{0.5} + \frac{\dot{j}_f|_x \mu_f}{\dot{j}_g \mu_g} \right) \quad (5.27)$$

The total pressure drop was then obtained by integrating Equation (5.27) from  $x = 0$  to  $x = L$ . The integration was performed with the assumption of uniform and non-uniform liquid water introduction. For uniform water introduction assumption, the integration of Eq. (5.27) yields:

$$\Delta P_{TP} = \Delta P_g (1 + 2/3 C \chi + 1/2 \chi^2) \quad (5.28)$$

For non-uniform liquid introduction, the integration of Eq. (5.27) yields:

$$\Delta P_{TP} = \Delta P_g (1 + 1/2 C \chi + 1/3 \chi^2) \quad (5.29)$$

Figure 18 compares the experimental results with the predicted pressure drop that has been calculated based on the model proposed in Ref. (18). The Chisholm parameter of 1.99 in the figure was calculated along with Equation (5.16) by using the square channel size of 1.59mm. The legends referring to Equation (10) and Equation (11) on the figure can be replaced with Equation (5.28) and Equation (5.29) of the current study, respectively. Figure 18 shows an overestimated two-phase pressure drop presented by the LM method with  $C = 5$  and  $C = 1.99$ . Also, different assumptions of uniform and non-uniform liquid water introduction do not exhibit any major differences. Figure 18 shows that the LM approach is not an appropriate method for predicting the pressure drop for slug flow that corresponds to high  $\phi^2$ . Nevertheless, the pressure drop model proposed by Zhang et al. (18) presents an improved prediction of the two-phase flow pressure drop.

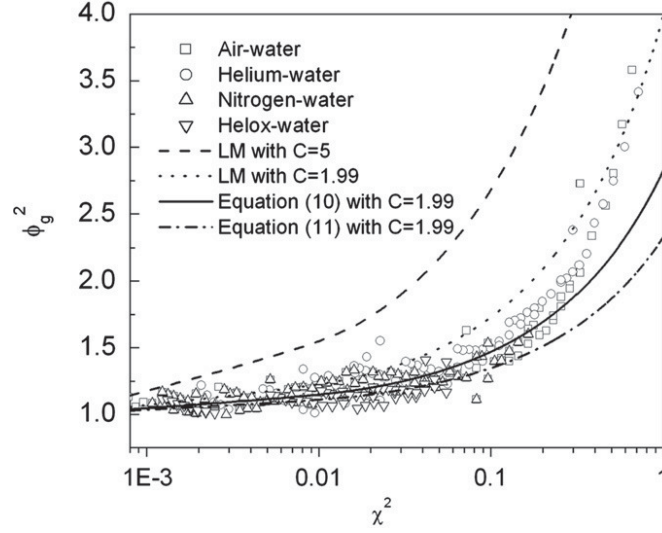


Figure 5.18: Comparison of the two-phase flow pressure drop model proposed by Zhang et al. (18) with experimentally measured two-phase flow pressure drop. Line tagging with Equation (10) corresponds to uniform liquid water introduction which is given by Equation 5.28 in the current review. Also line tagging with Equation (11) corresponds to non-uniform liquid water introduction which is given by Equation 5.29 in the current review.

So far, all of the pressure drop models proposed were based on ex-situ observations. Anderson et al. (17) conducted in-situ experiments and compared the pressure drop measured with the pressure drop predicted based on the correlation given by Zhang et al. (18). It was observed that the model proposed in Ref. (18) had a closer prediction to the actual pressure drop rather than the classical LM method. However, the proposed model proved to be inferior in expressing all of the water transport phenomena within an operating PEM fuel cell.

Grimm et al. (7) studied the two-phase flow pressure drop at different flow patterns of slug flow, film flow, and mist flow. For slug flow and film flow, they proposed two different series of C equations. In one equation, they proposed a modified C equation by back calculating the measured pressure drop based on Equation (5.24). Their proposed C equation is:



$$C = A\left(\frac{1-x}{x}\right)^b \quad (5.30)$$

where  $A$  and  $b$  are given by:

$$A = 0.0856(j_f)^{-1.202} \quad (5.31)$$

$$b = 0.004(j_f)^{-0.526} \quad (5.32)$$

It was claimed that this correlation yields a mean error of 14%. They also proposed other series of correlations based on the model developed by Lee and Lee (173) by weighting each of the terms in the original correlation and adding the liquid-to-air quality ratio,  $(1-x)/x$ . For slug flow they proposed:

$$C = 1.9087 Re_f^{-0.405} \lambda^{-0.134} \psi^{-0.421} \left(\frac{1-x}{x}\right)^{-0.107} \quad (5.33)$$

For film flow they proposed:

$$C = 0.772 Re_f^{0.051} \lambda^{0.016} \psi^{-1.716} \left(\frac{1-x}{x}\right)^{0.034} \quad (5.34)$$

where  $\lambda$  and  $\psi$  are defined by Lee and Lee (173) in Table 5.4.

The mean error reported by these correlations was 14% for slug flow and 4% for film flow. For mist flow, they suggested using the homogeneous flow model proposed by Dukler (156).

The two-phase flow pressure drop models developed for the application of PEM fuel cells were reviewed in this section. A comparison between the early studies to those done recently reveals some improvements in the models proposed. The experimental setups have been improved and more precise assumptions have been employed for

analyzing the results. However, the complicated multiphysics behind the two-phase flow pressure drop seeks further attention in this area. The assumptions need some corrections to yield models with a better prediction of the two-phase flow. In Section 5.6, the areas that need further attention are introduced.

## 5.7 Conclusion

Liquid-gas two-phase flow pressure drop with the application of PEM fuel cells is reviewed in this study. Most of the literature studying the pressure drop in PEM fuel cells is based on parametric studies. These studies compare the pressure drop measured at different liquid and gas flow rates, channel geometries, flow field geometries, gas stoichiometries, surface energies, temperatures, and relative humidities, and try to fit the results with models. Pressure drop in PEM fuel cell gas channels is considered to be a diagnostic tool that describes the amount of liquid water in the gas channels. By monitoring the pressure drop both in the cathode and anode of an operating fuel cell, water transport between the two electrodes can also be identified. Few studies propose modified models that predict the two-phase flow pressure drop in PEM fuel cell gas channels. While in most cases the proposed models are limited to a modified Chisholm parameter, there are some studies that go beyond this and introduce more accurate assumptions to model the unknown parameters. To summarize, the Lockhart-Martinelli (LM) method is an appropriate method to base the pressure drop prediction of slug flow and film flow, while the pressure drop of mist flow is better predicted with the homogeneous flow model because of the comparable liquid and gas superficial velocities.

The two-phase flow pressure drop prediction can be improved by enhancing the current assumptions or experimental conditions. The pressure drop correlations proposed

are only applicable over a limited range of working conditions and in most cases are only valid for the experimental setup used in the study. Also, the proposed models are based on the experimental results obtained from ex-situ setups with either a single gas channel or parallel gas channels. However, because the pressure drop strongly depends on the flow field geometry, the variation of pressure drop in common flow fields should also be studied. While the pressure drop has been known to depend on the existence of the GDL in the experimental setup, most of the proposed correlations are based on the observation of channels without a GDL.

The pressure drop correlations proposed are based on ex-situ experiments. Although ex-situ approach may be more accurate when studying a particular phenomenon, the applicability of the findings to an operating fuel cell is in doubt. The electrochemical reactions consume the reactants along the gas channel, and therefore, the gas flow rate differs from the channel inlet to the outlet of an operating cell. Ex-situ setup also mimics a constant water introduction along the gas channel, while the water production rate is not uniform along the gas channel of an operating cell. Furthermore, water back diffusion from the cathode to anode is always ignored in ex-situ studies. It is of extreme importance to consider all of the multiphysics occurring in an operating cell when studying the topic of two-phase flow pressure drop. Otherwise, any incomplete assumption may lead to an inaccurate pressure drop model. For instance, the assumption of liquid water being removed as the consequence of the pressure gradient before and after the slug may not be extended to a general scenario. This is because liquid water may be removed by other mechanisms, such as evaporation and/or capillary flow along the channel walls. Similarly, the local superficial water velocity should be determined with a more precise assumption. The water transport through the porous GDL can be modeled by Darcy's law, but the assumption of water being transported at an equal superficial gas velocity does not seem accurate. This

is because liquid water detachment from the surface of the GDL depends on different parameters such as GDL surface energy and superficial gas velocity. These reflect the need for a more fundamental study of the two-phase flow pressure drop in PEM fuel cell gas channels.

# Chapter 6

## Two-phase flow pressure drop measurement in PEM fuel cell flow channels

1

### 6.1 abstract

Proton exchange membrane (PEM) fuel cells produce power with water and heat as inevitable byproducts. Accumulated liquid water within gas channel blocks the reactant flow and cause pressure drop along the gas channel. It is of extreme importance to accurately predict the liquid and gas two-phase flow pressure drop in PEM fuel cell flow channels. This pressure drop can be considered as an in-situ diagnostic tool that reveals information about the amount of liquid water accumulated within the flow channels. In this paper, the two-phase flow pressure drops are measured in

---

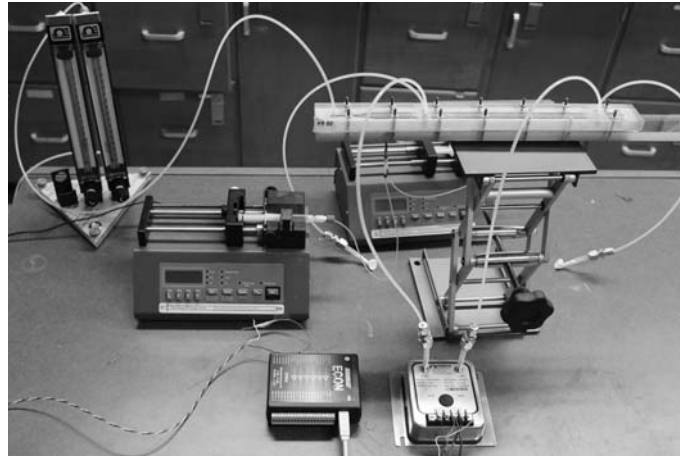
<sup>1</sup>The contents of this chapter will be published in ASME 2014 Fuel Cell Science, Engineering & Technology Proceeding

ex-situ PEM fuel cell parallel flow channels. The pressure drops were measured for air mass fluxes of  $2.4 - 6.3 \text{ kg/m}^2\text{s}$  and water mass fluxes of  $0.0071 - 1.28 \text{ kg/m}^2\text{s}$ . These mass fluxes correspond to  $2 - 5.33 \text{ m/s}$  and  $7.14 \times 10^{-6} - 0.0012 \text{ m/s}$  air and water superficial velocities, respectively. The measured two-phase flow pressure drops are then compared with different two-phase flow pressure drop models. Qualitative and quantitative comparison between the experimental results and existing models is provided in this work.

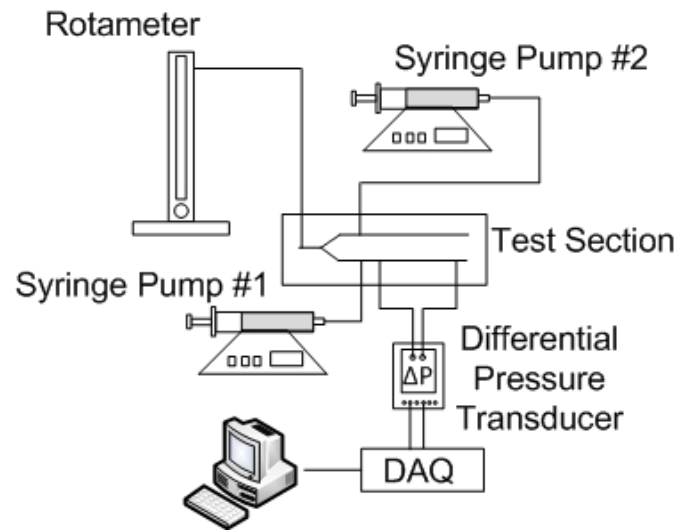
## 6.2 Experimental setup

An ex-situ experimental setup was designed and fabricated to measure the liquid and gas two-phase flow pressure drop in two parallel gas channels. Figure 6.1 shows the photograph and the schematic of the experimental setup used in this study. The experimental setup includes a test section that holds two rectangular parallel flow channels, two rotameters to adjust the required air flow rate, two separate syringe pumps to inject liquid water into the GDL, a differential pressure transducer, and a digital data acquisition system. The test section includes two polycarbonate plates, each with 1/2 inch thickness, an aluminum plate with header and parallel gas channels machined on, and a GDL to simulate similar surface condition of the gas channel in PEM fuel cell. Air was supplied to the header of the test section with 1mm and 2.5mm cross-sectional area. The header branches into two parallel gas channels, each with similar dimensions as the header. Liquid water was injected to the surface of the GDL in both channels through two capillary tubes with  $250 \mu\text{m}$  diameters (U-111, Upchurch). The capillary tubes were inserted into the polycarbonate plate with their water injection side aligned with the surface of the GDL. The capillary tubes were positioned 10mm downstream from the beginning of the gas channel. The two-phase

flow pressure drops were measured through two pressure taps that had been fabricated 200mm apart from each other. The first pressure tap (high pressure) was machined 40mm after the liquid injection port to satisfy a uniform two-phase flow in the pressure measurement length. Air was supplied into the test section through two different rotameters (Omega, FL\_3802C and FL\_3804ST) depending on the required air flow rate. A differential pressure transducer (Omega, PX653\_02D5V) was employed to measure the two-phase flow pressure drop at a 50Hz sampling frequency. The pressure range that can be measured via this pressure transducer is from zero to 500Pa. This high accuracy of pressure measurement is required for the purpose of this study. Toray carbon paper TGP-060 was used as the GDL sample between the aluminum plate and the polycarbonate plate. The GDL had not been treated with PTFE. Table 6.1 lists the test conditions used in this study.



(a)



(b)

Figure 6.1: Photograph and the schematic of the experimental setup



Table 6.1: Test conditions used in this study

Air flow rate (header) ml/min	Superficial air velocity (each channel) m/s	Superficial air Reynolds number	Water flow rate (each channel) $\mu\ell/h$	Superficial water velocity m/s	Superficial water Reynolds number	Mass flow quality (x)
600	2	182	4072	0.000452	0.71	0.84
600	2	182	3480	0.000386	0.61	0.86
600	2	182	2915	0.000323	0.51	0.88
600	2	182	2375	0.000263	0.41	0.90
600	2	182	1859	0.000206	0.32	0.92
600	2	182	1364	0.000151	0.24	0.94
600	2	182	891	$9.89 \times 10^{-5}$	0.15	0.96
1000	3.33	303	4858	0.000539	0.85	0.88
1000	3.33	303	3959	0.000439	0.69	0.90
1000	3.33	303	3098	0.000344	0.54	0.92
1000	3.33	303	2274	0.000252	0.40	0.94
1000	3.33	303	1484	0.000164	0.26	0.96
1600	5.33	485	11000	0.001222	1.94	0.838
1600	5.33	485	9500	0.001055	1.67	0.857
1600	5.33	485	8500	0.000944	1.50	0.87
1600	5.33	485	7327	0.000814	1.29	0.885
1600	5.33	485	6297	0.000699	1.11	0.90
1600	5.33	485	4928	0.000547	0.87	0.92
1600	5.33	485	3618	0.000402	0.64	0.94
1600	5.33	485	2380	0.000264	0.42	0.959

### 6.3 Results and discussion

To validate the functionality of the experimental setup, the single phase air flow pressure drop was measured at different flow rates. Figure 6.2 compares the experimentally obtained friction factor with Darcy friction factor for laminar flow,  $f=64/Re$ . The compatibility between the experimental friction factor of both channels and the theoretical friction factor confirms that the setup can be properly used for this study.

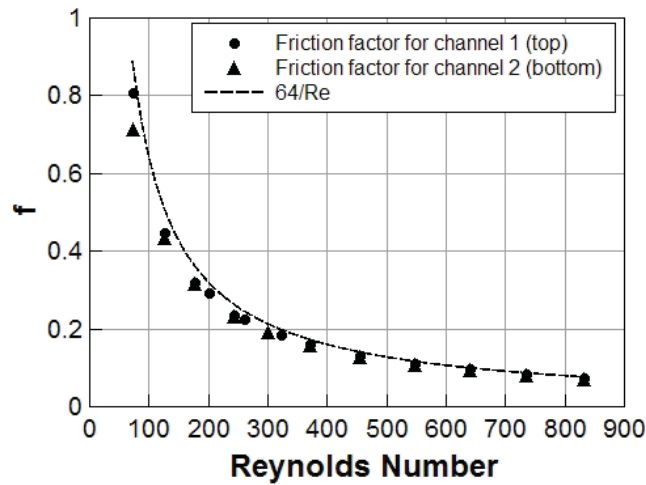


Figure 6.2: Comparing the experimental and theoretical friction factor for single phase air flow.

Figure 6.3 compares different models of two-phase flow pressure drop predictions for the whole range of mass flow quality. Models such as Mishima and Hibiki (Eqn. 5.16), English and Kandlikar (Eqn. 5.24), Sun and Mishima (167), and homogeneous flow model of Beattie and Walley (157) are compared in this figure. The pressure drop prediction has been done for 1600ml/min air flow rate. In general, it can be observed from the figure that the Sun and Mishima's model gives the maximum pressure drop prediction while the homogeneous flow model of the Beattie and Walley results in minimum pressure drop predictions. In all of these pressure drop predictions, the

Fanning friction factor given in Equation 5.10 has been utilized.

In PEM fuel cell application, the range of mass flow quality,  $x$ , is between 0.78 to 0.94. This corresponds to cathode stoichiometry ratios of 1 to 5. It is also assumed that all of the produced water is in liquid phase. The predicted pressure drop for mass flow quality between 0.8 and 1 is zoomed in within the inset of this Figure 6.3. It can be observed that the predicted two-phase flow pressure drop for mass flow quality of 0.9 ranges between 319Pa and 515Pa for Beattie-Walley and Mishima-Hibiki correlations, respectively.

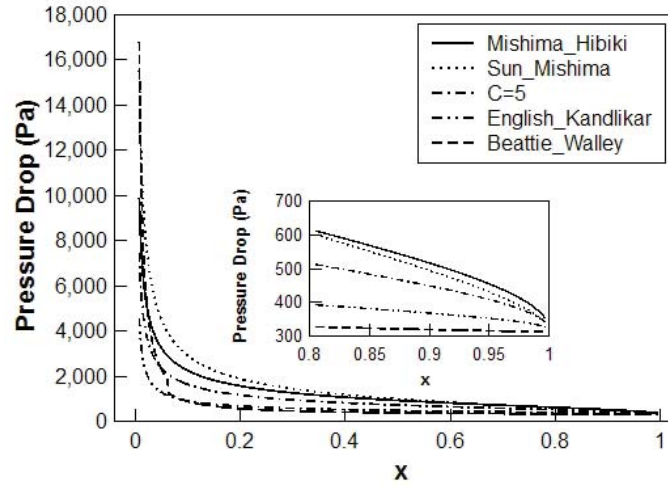


Figure 6.3: Two-phase flow pressure drop predictions based on different models. Air flow rate was considered to be at 1600ml/min.

The two-phase flow pressure drops were measured for different air flow rates and different mass qualities,  $x$ , according to the experimental conditions listed in Table 6.1. Figure 6.4 compares the experimentally measured two-phase flow pressure drops at 1600ml/min air flow rate with pressure drop calculated based on different models. Each data point is the time averaged over 60s. The error bars also represent the standard deviation of each pressure profile. The range of the mass flow quality,  $x$ , is chosen to be in the range of PEM fuel cell operation condition. It can be concluded

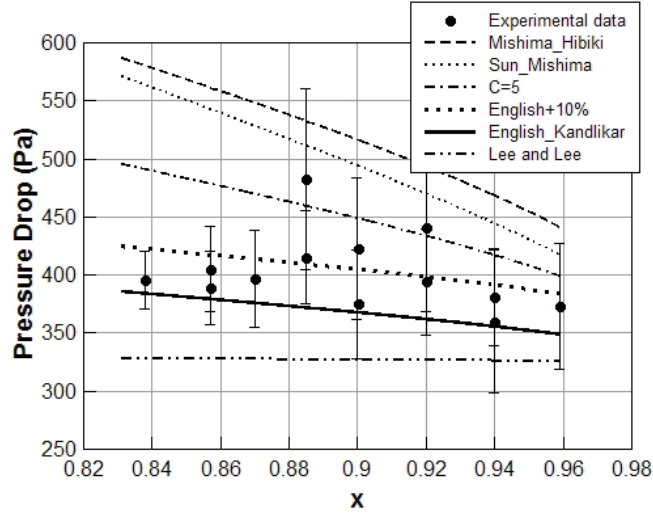


Figure 6.4: Comparison of experimental two-phase flow pressure drop with models for different mass fluxes at 1600ml/min air flow rate.

that while the English and Kandlikar's model (Eqn. 5.24) underestimates the two-phase flow pressure drop, it still gives the most accurate pressure drop prediction compared to other models. The green dashed line on this figure shows the upper 10% margin of this model. It can be observed that for 1600ml/min air flow rate, the pressure drop measured for most of the mass flow qualities fall within 10% of English and Kandlikar's model.

The two-phase flow pressure drop for different air flow rates have also been measured in this study. Figure 6.5 shows the two-phase flow pressure drops for 600ml/min, 1000ml/min and 1600ml/min air flow rates. Each data point is the time average of the pressure drop over 60s. The error bars show the standard deviation of the pressure drop profile. The solid line in this figure shows the pressure drop prediction based on English and Kandlikar's model. The dashed lines in the figure show the lower and upper 10% margin of this model. The pressure drop results of 1600ml/min air flow rate have been discussed in Figure 6.4. Figure 6.5 shows that while the English model can properly predict the two-phase flow pressure drop for high air flow

rate (1600ml/min), its accuracy deteriorates as the air flow rate decreases. While the majority of pressure drop data points for 1600ml/min air flow rate fall within 10% of the English model, no data point for 1000ml/min air flow rate falls within this range. However, the pressure drop for this air flow rate is still close to the pressure drop predicted by English and Kandlikar's model. For the lowest air flow rate considered in this study (600ml/min) the difference between the experimentally measured pressure drop and the predicted pressure drop by English and Kandlikar's model becomes significant. Figure 6.5 shows that for this air flow rate, the pressure drop data points are not even close to the 10% range of the English and Kandlikar's model. The difference between experimental and predicted pressure drop becomes significant for lower mass flow qualities. The pressure drop measured for mass flow quality of 0.84 was 256Pa while the English model predicts 141Pa for this mass flow quality. This is equivalent to 84% difference between the experiment and the model. In general, such discrepancies may be due to the lower air and water flow rates of this study compared to English and Kandlikar's work. Table 6.2 compares the range of the air and water flow rate for Ref.(20) and the current study for the lowest air flow rate, 600ml/min. It can be noticed from the table that the air and water flow rates corresponding to 600ml/min air flow are not within the experimental range of English and Kandlikar's work. Therefore it may be concluded that the C equation proposed by English and Kandlikar can only be valid over a limited range of air and water flow rates, as considered in Ref. (20). For flow rates lower than Ref.(20) another correlation might be used.

The two-phase flow pressure drop for 600ml/min has been further investigated. Figure 6.6 compares the experimental data with two different models of English and Kandlikar (Eqn. 5.24) and Mishima and Hibiki (Eqn. 5.16). Mishima and Hibiki's model has been chosen for the sake of comparison because it is the original source of

Table 6.2: Test conditions used in Ref.(20) and the lowest air flow rate in the current study

	English and Kandlikar (20)	Current study (600ml/min)
Air mass flux ( $\text{kg}/\text{m}^2\text{s}$ )	4.03-12	2.368
Water mass flux ( $\text{kg}/\text{m}^2\text{s}$ )	0.49-21.6	0.0071-0.48
Superficial air velocity (m/s)	3.19-10.06	2
Superficial water velocity (m/s)	0.0005-0.0217	$7.14 \times 10^{-6}$ -0.0004
Superficial air Reynolds number	211-654	182
Superficial water Reynolds number	0.56-24.6	0.011-0.76

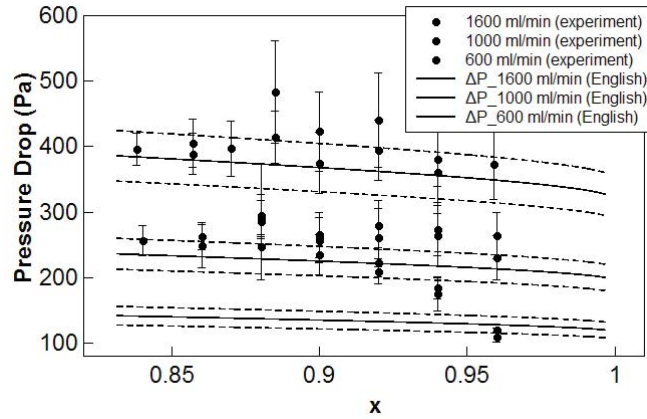


Figure 6.5: Comparison of experimental two-phase flow pressure drop with English and Kandlikar's model at different air flow rates.

the English and Kandlikar's model. This model was also observed to give the maximum pressure drop prediction compared to other models shown in Figure 6.3. The dashed lines on Figure 6.6 show the 10% margin of each model. Figure 6.6 shows that while the Mishima and Hibiki model does a better prediction of the two-phase flow pressure drop compared to the English and Kandlikar model, it still underestimates the pressure drop for 600ml/min air flow rate.

The two-phase flow pressure drops discussed in this study were the time average of the pressure profile over 60s. The two-phase flow pressure profile for 1600ml/min air flow rate and at three different mass qualities are shown in Figure 6.7. It can be observed in the general trend of this figure that as the mass flow quality decreases,

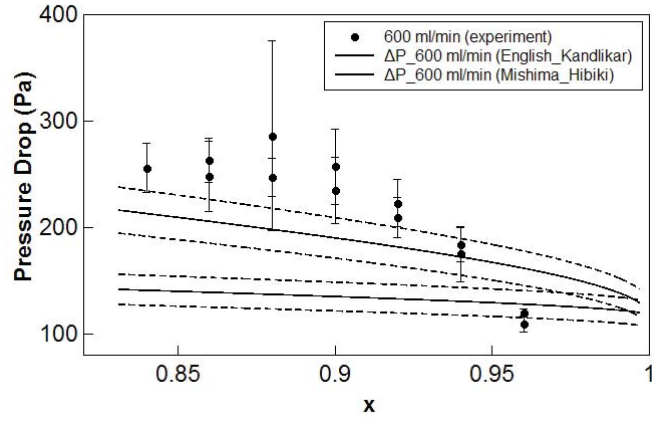


Figure 6.6: Comparing the English and Kanlikar's model with Mishima and Hibiki's model for 600ml/min air flow rate

the two-phase flow pressure drop increases. This is because more liquid water will enter the gas channel that consequently results in an increased pressure drop. The mean value of the pressure drop for mass flow qualities of 0.857, 0.9 and 0.959 were 409Pa, 375Pa, and 347Pa, respectively.

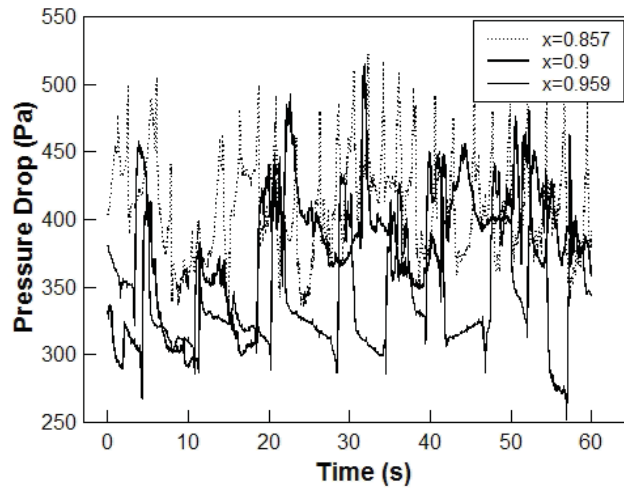


Figure 6.7: Two-phase flow pressure drop profiles for different mass qualities and at 1600ml/min air flow rate.

## 6.4 Conclusion

The two-phase flow pressure drop for the application of PEM fuel cell has been studied in this work. The two-phase flow pressure drops were measured for different air flow rates (600ml/min, 1000ml/min, and 1600ml/min) and different mass flow qualities. The measured pressure drops were then compared with different two-phase flow pressure drop models. It has been observed that the two-phase flow pressure drop for the highest air flow rate, 1600ml/min, falls within 10% of the English and Kandlikar's model. However, decreasing the air flow rate resulted in an underestimation of the pressure drop based on this model. The measured pressure drop for 600ml/min and 1000ml/min were not within 10% of the English and Kandlikar's model. The deviation became even worse for lower mass flow qualities and 600ml/min air flow rate. For this air flow rate, the pressure drop predicted by English and Kandlikar's model was up to 84% off from the measured pressure drop. Instead, the Mishima and Hibiki's model was found to give a more accurate pressure drop prediction for the lowest air flow rate.



## Chapter 7

# Two-phase flow pressure drop during droplet emergence and growth

### 7.1 Introduction

In this chapter, the pressure drop and the droplet size are monitored simultaneously. Liquid water was injected into the surface of the GDL in a single gas channel and the pressure drop before and after the droplet emergence location was measured. Droplet emergence and growth was also recorded by a high speed camera.

### 7.2 Experimental Setup

A single gas channel with  $2.5\text{mm} \times 3\text{mm}$  cross section was machined on a 3mm thick polycarbonate plate and was sandwiched by two other polycarbonate plates with 12.5mm tickness. Liquid water was injected through a  $250\mu\text{m}$  capillary into the surface of the GDL. PTFE treated (33wt.%) Toray carbon paper TGP-060 was used as GDL. The GDL was inserted between the gas channel polycarbonate plate

and the liquid water injection polycarbonate plate. Six 1/8inch screws tightened the whole assembly together. A high speed camera (50KD2B2, Mega Speed) was used to record the images of droplet growth and detachment at 100 frames per second. Pressure drop before and after the droplet was measured with a high accuracy pressure transducer (Omega, PX653\_0.25D5V) with 62Pa pressure range (0.25 inch water). The sampling was done at 1000Hz frequency. The pressure measurements were done along 4cm within the gas channel. Liquid water was injected 1cm from the first pressure tap. Figure 7.1 shows the schematic of the test section used. Air was supplied with superficial velocities of 5.33m/s, 6m/s, 6.66m/s, 7.22m/s, and 7.77m/s. Table 7.1 lists the experimental conditions considered in this study.

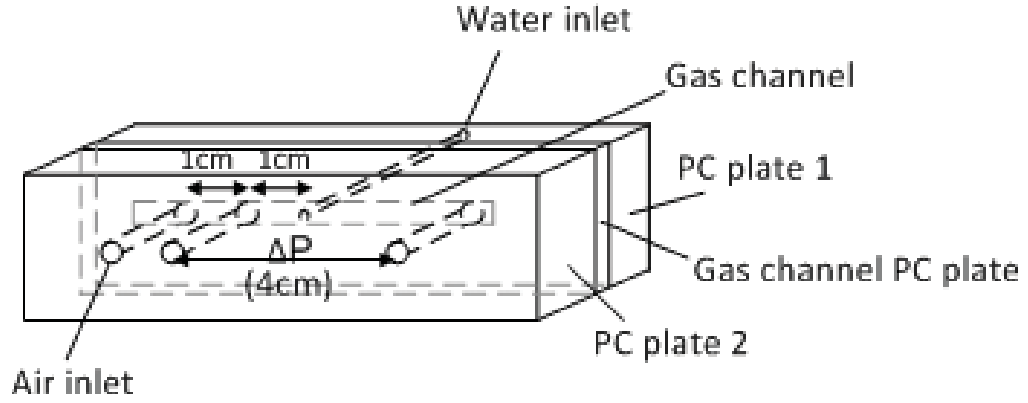


Figure 7.1: Schematic of test section

Table 7.1: Water flow rate considered in this study

Air flow rate (ml/min)	Superficial air velocity(m/s)	Water flow rate ( $\mu\ell/h$ )	Superficial water velocity (m/s)	Mass flow quality (x)
2400	5.33	1859	$6.883 \times 10^{-5}$	0.989
2700	6	2200	$8.14 \times 10^{-5}$	0.9885
3000	6.66	3255	$1.205 \times 10^{-4}$	0.985
3250	7.22	3255	$1.205 \times 10^{-4}$	0.986
3500	7.77	1253	$4.639 \times 10^{-5}$	0.995

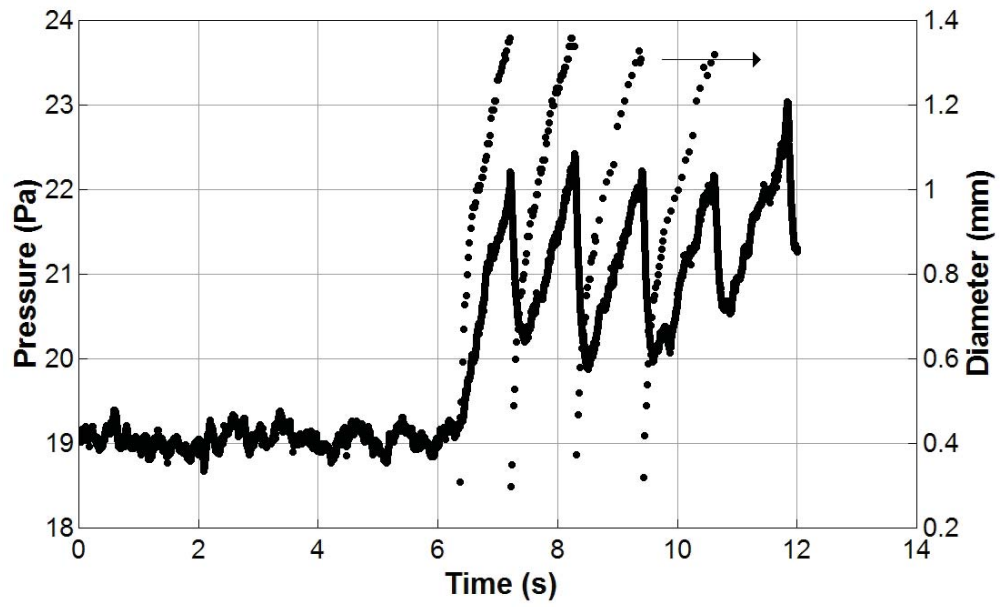
## 7.3 Result and discussion

### 7.3.1 Pressure drop and droplet diameter

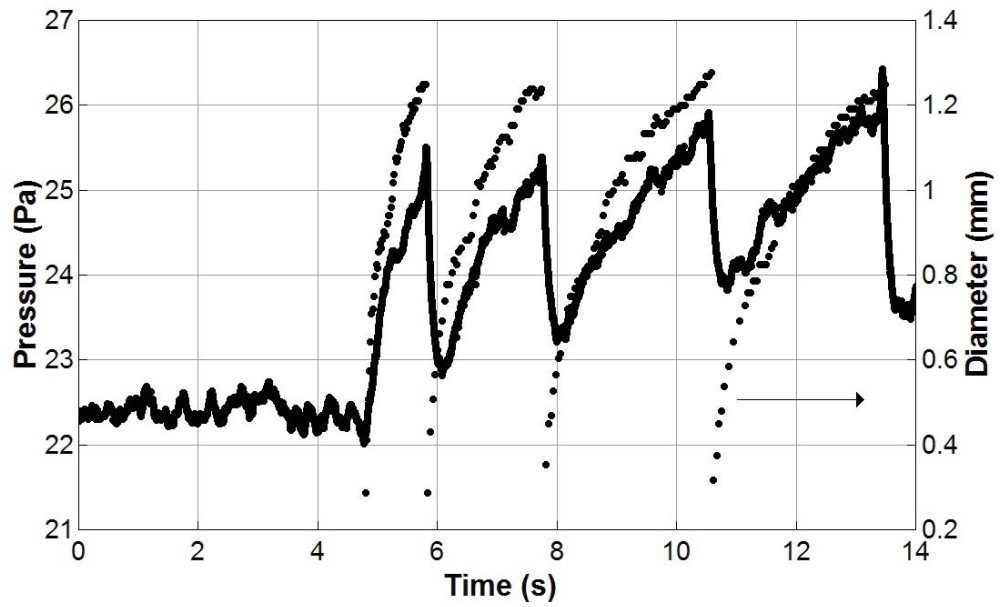
By injecting liquid water into the gas channel and by supplying air from the inlet, a two-phase flow forms within the channel. Figure 7.2 shows the pressure drop and droplet diameter overlaid for two different superficial air velocities. The pressure profile is almost constant at the beginning of the experiment that can be interpreted as having a single phase flow of air within the gas channel. The single phase air flow pressure drop shown in Figure 7.2-a is  $\sim 19\text{Pa}$ . The pressure drop then increases as the liquid water is emerged from the surface of the GDL. The pressure drop increases by the droplet size until the core gas flow can detach the droplet from the surface of the GDL. The figure shows a pressure drop equivalent of  $22.2\text{Pa}$  upon detachment of the first droplet at  $6.66\text{m/s}$  superficial air velocity. The droplet diameter upon detachment is  $1.36\text{mm}$ . Each peak above  $22\text{Pa}$  in this figure represents the droplet detachment from the surface of the GDL.

The pressure profile shows a change in slope in the pressure at  $6.8\text{s}$ . This change in the pressure profile can also be tracked by a slope change in the diameter. Similar behavior can be observed at  $10.25\text{s}$  on the same figure. For both cases, the droplet diameter at this pressure slope change is close to  $1\text{mm}$ . It can be concluded that at some cases, a change in the pressure profile occurs that is accompanied by a change in the droplet diameter over time.

Figure 7.2-b shows the pressure profile and the droplet diameter for  $7.77\text{m/s}$  superficial air velocity. Similar to Figure 7.2-a, the pressure profile shows a change in slope. However, it should be added that not all pressure spikes show this slope change. The second and the third spike in Figure 7.2-a, for instance, have a constant slope up to the droplet detachment at  $22.4\text{Pa}$  and  $22.2\text{Pa}$ , respectively.



(a) Superficial air velocity 6.66m/s and  $x = 0.985$



(b) Superficial air velocity 7.77m/s and  $x = 0.995$

Figure 7.2: Pressure profile and droplet diameter

Another noticeable observation of this figure suggests that while droplets are detaching at comparable diameter and pressure, the time interval they need to be detached is not constant. It can be observed from Figure 7.2-b that first droplet grows and detaches at 1s while the third droplet need 2.5s to be detached from the surface of the GDL.

The effect of superficial air velocity on the pressure profile can be noticed in Figure 7.2. It can be observed that increasing the superficial air velocity from 6.66m/s to 7.77m/s adds to the oscillation in the pressure profile. This increased oscillation due to higher superficial air velocity can be attributed to further droplet movement during its growth until detachment.

The pressure slope change can be further studied by analyzing the pressure profiles for all test conditions given in Table 7.1. Figure 7.3 shows the normalized droplet area at which pressure slope changes. The normalized droplet area is defined as the ratio of the projected area of the droplet upon detachment to the channel cross-sectional area:

$$\text{Normalized droplet area} = \frac{\text{Droplet projected area upon detachment}}{\text{Channel cross-sectional area}} \quad (7.1)$$

For calculating the projected area, droplet static contact angle of  $150^\circ$  was considered. Although the advancing and receding contact angles are different upon detachment, the static contact angle can give a close estimation to the actual projected area of the droplet.

The general trend of Figure 7.3 shows that the pressure slope change occurs at a higher normalized droplet area as the air flow rate increases. The pressure slope change can be attributed to a sudden and significant droplet repositioning within the gas channel before its detachment. As droplet emerges and grows, it pins to the

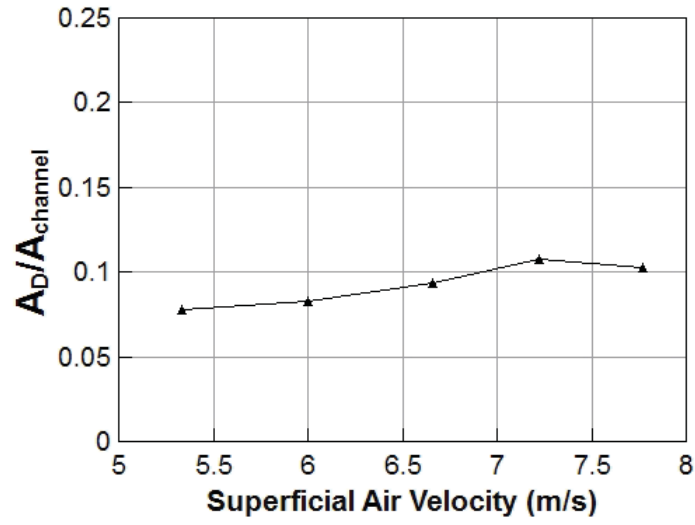


Figure 7.3: Normalized droplet projected area at pressure profile change

emergence location. However, the droplet slightly moves from its emergence location and that movement causes a change in the pressure profile. Figure 7.4 shows the images of droplet growth corresponding to the first spike in Figure 7.2-a. The first pressure slope change in Figure 7.2-a occurs at 6.82s. For the images shown in Figure 7.4, the droplet shows a maximal movement from 6.71s to 6.82s.

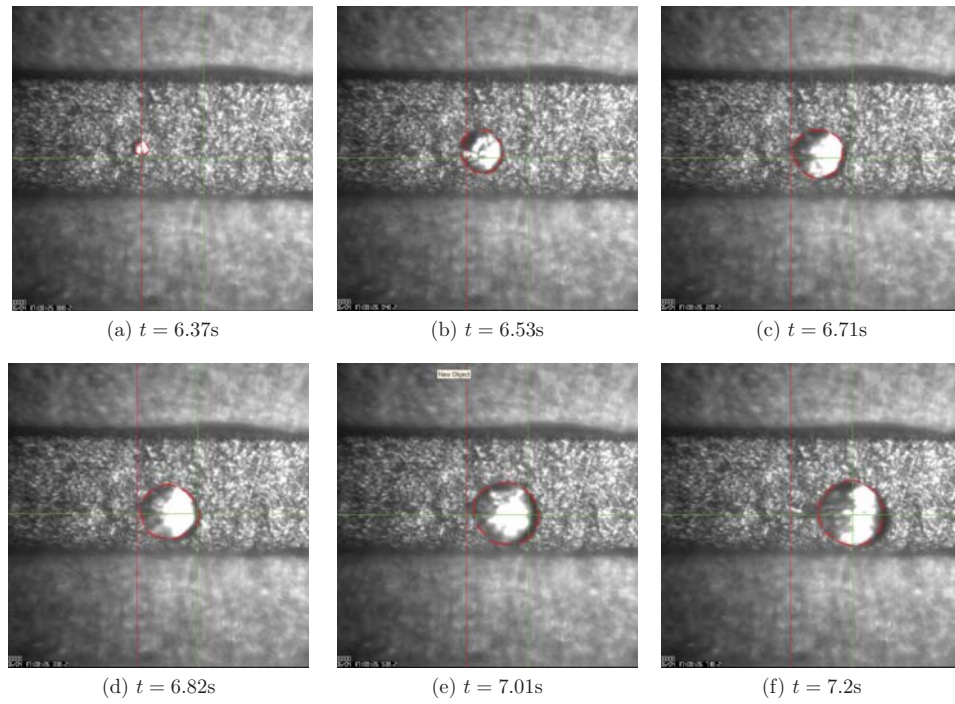


Figure 7.4: Droplet emergence and growth for 6.66m/s superficial air velocity. The images belong to the first pressure spike shown in Figure 7.2a. The red line in the figure shows the droplet emergence line and the green cross shows the droplet detachment location. The droplet moves  $\sim 1.3\text{mm}$  from the emergence to the detachment location.

Based on the pressure drop measurement and the droplet image recorded, the drag coefficient can be calculated by applying the linear momentum equation. For a non-deforming and fixed (inertia) control volume, the linear momentum equation is given as:

$$\frac{\partial}{\partial t} \int_{CV} \mathbf{V} \rho dV + \int_{CS} \mathbf{V} \rho \mathbf{V} \cdot \hat{\mathbf{n}} dA = \Sigma \mathbf{F} \quad (7.2)$$

When there is no liquid water in the gas flow channel, the pressure drop along the gas channel is due to the frictional force exerted by the channel wall. Following the linear momentum equation, this frictional force is simply proportional to the pressure gradient along the gas channel:

$$\text{Frictional force} = \Delta P \times \text{Area} \quad (7.3)$$

Any increase in the pressure is due to the emergence and growth of liquid water on the surface of the GDL. Using the linear momentum equation, the drag force can be obtained based on the pressure increase:

$$\text{Drag force} + \text{Frictional force} = \Delta P \times \text{Area} \quad (7.4)$$

The drag force calculated in Equation 7.4 can be used to calculate the drag coefficient:

$$C_D = \frac{2F_D}{\rho V^2 A_{projected}} \quad (7.5)$$

where  $V$  is the superficial air velocity and  $A_{projected}$  is the droplet projected area. As mentioned before, the static contact angle was used to calculate the droplet projected area. While the dynamic advancing and receding contact angles are different from static contact angle, the difference they cause in the calculated area can be considered



negligible.

Figure 7.5 shows the drag coefficient calculated for different superficial air velocities. The red points on the figure represent the pressure slope change in pressure profile. The general trend of this figure show that the drag coefficient decreases over time. Since droplet grows over time, it can be concluded that the drag coefficient decreases as droplet grows in size. This is because the droplet projected area increases faster than the drag force and according to Equation 7.5, the drag coefficient should decrease to compensate for this change.

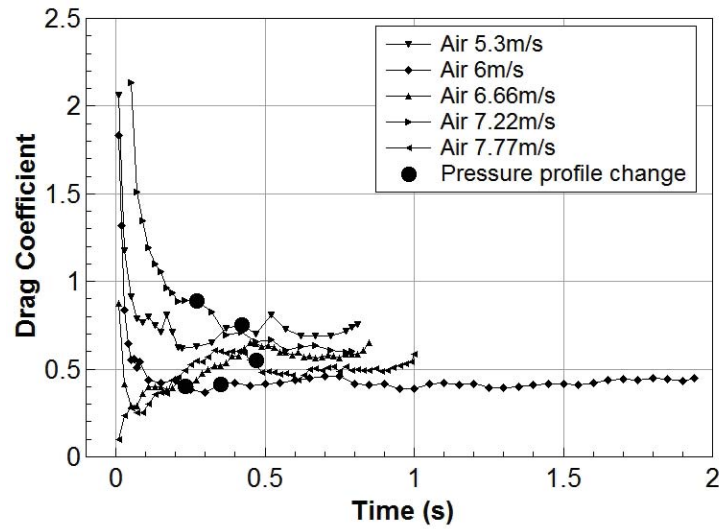


Figure 7.5: Drag coefficient and pressure profile change

## 7.4 Conclusion

Two-phase flow pressure drop for the application of PEM fuel cell has been studied. The pressure drop during droplet emergence and growth were measured with a high accuracy pressure transducer. The droplet emergence and growth was also captured using a high speed camera. The following conclusions can be drawn from this study:

1. Pressure profile shows a change in slope as droplet grows in size.
2. Pressure slope change occurs at larger droplet size as the air flow rate increases.
3. Increasing the superficial gas velocity was found to add to the oscillation of the pressure profile.
4. The drag coefficient calculated for different superficial air velocities was found to decrease as the droplet grows in size.

# Chapter 8

## Conclusion

In this research, liquid water transport within PEM fuel cell flow channels and through gas diffusion layer were studied by taking an ex-situ approach. Gas diffusion layer microstructural properties were also investigated by analyzing SEM images taken from the GDL samples.

- Droplet contact angles on Toray carbon papers were measured for PTFE treated and untreated samples. While PTFE treating of GDLs significantly increases the contact angle compared to untreated GDLs, the amount of PTFE content within GDL was found to have minimal impact on the contact angle. GDL microstructural properties such as mean pore diameter and pore diameter distribution were obtained by analyzing SEM images of GDLs. A mean pore diameter of  $\sim 26\mu\text{m}$  was obtained for Toray carbon paper used in this research. The GDL thickness was found to have no particular impact on the GDL mean pore diameter. Furthermore, the pore diameter distribution plots indicated that the majority of pores have diameters less than  $20\mu\text{m}$ .
- Liquid water transport through GDL was studied by measuring the breakthrough pressure. The liquid water breakthrough pressure was observed to

increase with GDL thickness. The GDL thickness was found to have a two-fold impact on the liquid water breakthrough pressure. While the thicker GDL has a greater number of pores that liquid water needs to pass, it is also more probable that liquid water passes through smaller pores in thicker GDLs. Furthermore it was noticed that while applying some amount of PTFE to an untreated GDL increases the breakthrough pressure, the breakthrough pressure slightly varies for different PTFE contents with GDLs. Moreover, the liquid water breakthrough pressure was found to increase with GDL compression. Another noticeable conclusion of this part was the effect of Nafion, as a hydrophilic agent, in GDL on the liquid water breakthrough pressure. It has been observed that while treating GDLs with Nafion increases the droplet contact angle, it decreases the liquid water breakthrough pressure. Such observation has been justified by hydrophobic characteristic of Nafion film and hydrophilic behavior of Nafion particles as they absorb water.

- Water transport on GDL surface was studied by measuring the droplet detachment diameter on GDLs with different PTFE contents. Air and hydrogen were supplied within the gas flow channel to resemble cathode and anode working conditions, respectively. It has been observed that liquid water does not detach from an untreated GDL surface. However, applying some amount of PTFE to an untreated GDL results in droplet detachment from the surface of the GDL. Furthermore, droplet detachment diameter was observed to decrease by increasing PTFE content within the GDL. A detailed discussion about this observation is provided in the relevant chapter. Moreover, it has been observed that droplet detachment in anode flow channels requires higher hydrogen superficial velocities compared to air flowing in the cathode flow channels. This originates from

hydrogen's lower density compared to air as the drag force exerted to the droplet is a function of gas density.

- Water transport in PEM fuel cell flow channels has been characterized by two-phase flow pressure drop. A comprehensive review has been done on two-phase flow pressure drop models, in general, and two-phase flow pressure drop correlations developed for the application of PEM fuel cell. The two-phase flow pressure drop was also measured for different air and water flow rates. The pressure drop data were compared with different models. Furthermore, the two-phase flow pressure drop during droplet formation and growth was measured. The pressure drop profile and droplet diameter were characterized in details.

# Bibliography

- [1] Mehdi Mortazavi and Kazuya Tajiri. In-plane microstructure of gas diffusion layers with different properties for pefc. *Journal of Fuel Cell Science and Technology*, 11(2):021002, 2014.
- [2] J. Benziger, J. Nehlsen, D. Blackwell, T. Brennan, J. Itescu. Water flow in the gas diffusion layer of PEM fuel cells. *J. Membr. Sci.*, 261(1-2):98–106, 2005.
- [3] A. Tamayol, M. Bahrami. Water permeation through gas diffusion layers of proton exchange membrane fuel cells. *J. Power Sources*, 196:6356–6361, 2011.
- [4] K.A. Triplett, S.M. Ghiaasiaan, S.I. Abdel-Khalik, D.L. Sadowski. Gas-liquid two-phase flow in microchannels Part I: two-phase flow patterns. *Int. J. Multiphas Flow*, 25(3):377–394, 1999.
- [5] F.Y. Zhang, X.G. Yang, C.Y. Wang. Liquid Water Removal From A Polymer Electrolyte Fuel Cell. *J. Electrochem. Soc.*, 153:A225, 2006.
- [6] Z. Lu, SG Kandlikar, C. Rath, M. Grimm, W. Domigan, AD White, M. Hardbarger, JP Owejan, and TA Trabold. Water management studies in PEM fuel cells, Part II: Ex situ investigation of flow maldistribution, pressure drop and two-phase flow pattern in gas channels. *Int. J. Hydrogen Energy*, 34(8):3445–3456, 2009.

- [7] M. Grimm, E.J. See, S.G. Kandlikar. Modeling gas flow in PEMFC channels: Part I-Flow pattern transitions and pressure drop in a simulated ex situ channel with uniform water injection through the GDL. *Int. J. Hydrogen Energy*, 37:12489–12503, 2012.
- [8] Xuan Liu, Hang Guo, Fang Ye, and Chong Fang Ma. Water flooding and pressure drop characteristics in flow channels of proton exchange membrane fuel cells. *Electrochim. Acta*, 52(11):3607–3614, 2007.
- [9] Shou-Shing Hsieh, Bing-Shyan Her, and Yi-Ji Huang. Effect of pressure drop in different flow fields on water accumulation and current distribution for a micro pem fuel cell. *Energy Conversion and Management*, 52(2):975–982, 2011.
- [10] N. Akhtar, A. Qureshi, J. Scholta, C. Hartnig, M. Messerschmidt, W. Lehnert. Investigation of water droplet kinetics and optimization of channel geometry for pem fuel cell cathodes. *Int. J. Hydrogen Energy*, 34(7):3104–3111, 2009.
- [11] R. Anderson, D.P. Wilkinson, X. Bi, L. Zhang. Two-phase flow pressure drop hysteresis in parallel channels of a proton exchange membrane fuel cell. *J. Power Sources*, 195(13):4168 – 4176, 2010.
- [12] Z. Lu, C. Rath, G. Zhang, S.G. Kandlikar. Water management studies in PEM fuel cells, part IV: Effects of channel surface wettability, geometry and orientation on the two-phase flow in parallel gas channels. *Int. J. Hydrogen Energy*, 36(16):9864–9875, 2011.
- [13] I.S. Hussaini, C.Y. Wang. Visualization and quantification of cathode channel flooding in pem fuel cells. *J. Power Sources*, 187(2):444–451, 2009.
- [14] M. Blanco, D.P. Wilkinson, and H. Wang. Application of water barrier layers

- in a proton exchange membrane fuel cell for improved water management at low humidity conditions. *Int. J. Hydrogen Energy*, 36:3635–3648, 2011.
- [15] L. Zhang, H.T. Bi, D.P. Wilkinson, J. Stumper, and H. Wang. Gas-liquid two-phase flow patterns in parallel channels for fuel cells. *J. Power Sources*, 183(2):643–650, 2008.
- [16] L. Zhang, W. Du, H.T. Bi, D.P. Wilkinson, J. Stumper, H. Wang. Gas-liquid two-phase flow distributions in parallel channels for fuel cells. *J. Power Sources*, 189(2):1023–1031, 2009.
- [17] R. Anderson, D.P. Wilkinson, X. Bi, and L. Zhang. Two-phase flow pressure drop hysteresis in an operating proton exchange membrane fuel cell. *J. Power Sources*, 196:8031–8040, 2011.
- [18] L. Zhang, X.T. Bi, D.P. Wilkinson, R. Anderson, J. Stumper, H. Wang. Gas-liquid two-phase flow behavior in minichannels bounded with a permeable wall. *Chem. Eng. Sci.*, 66(14):3377–3385, 2011.
- [19] D. Chisholm. A theoretical basis for the lockhart-martinelli correlation for two-phase flow. *Int. J. Heat Mass Tran.*, 10:1767–1778, 1967.
- [20] N.J. English, S.G. Kandlikar. An experimental investigation into the effect of surfactants on air-water two-phase flow in minichannels. *Heat Transfer Eng.*, 27(4):99–109, 2006.
- [21] M.V. Williams, E. Begg, L. Bonville, H.R. Kunz, J.M. Fenton. Characterization of gas diffusion layers for PEMFC. *J. Electrochem. Soc.*, 151:A1173, 2004.
- [22] T.V. Nguyen. Water Management by Material Design and Engineering for PEM Fuel Cells. *ECS Transactions*, 3:1171–1180, 2006.



- [23] P.K. Sinha, P.P. Mukherjee, C.Y. Wang. Impact of GDL structure and wettability on water management in polymer electrolyte fuel cells. *J. Mater. Chem.*, 17(30):3089–3103, 2007.
- [24] A. Bazylak. Liquid water visualization in PEM fuel cells: A review. *Int. J. Hydrogen Energy*, 34(9):3845–3857, 2009.
- [25] W. Dai, H. Wang, Z.Z. Yuan, J.J. Martin, D. Yang, J. Qiao, J. Ma. A review on water balance in the membrane electrode assembly of proton exchange membrane fuel cells. *Int. J. Hydrogen Energy*, 34(23):9461–9478, 2009.
- [26] K. Tüber, D. Pócza, C. Hebling. Visualization of water buildup in the cathode of a transparent PEM fuel cell. *J. Power Sources*, 124(2):403–414, 2003.
- [27] D. Spornjak, A.K. Prasad, S.G. Advani. Experimental investigation of liquid water formation and transport in a transparent single-serpentine PEM fuel cell. *J. Power Sources*, 170:334–344, 2007.
- [28] X.G. Yang, F.Y. Zhang, A.L. Lubawy, C.Y. Wang. Visualization of liquid water transport in a PEFC. *Electrochem. Solid St.*, 7:A408, 2004.
- [29] A. Theodorakakos, T. Ous, M. Gavaises, J.M. Nouri, N. Nikolopoulos, H. Yanagihara. Dynamics of water droplets detached from porous surfaces of relevance to PEM fuel cells. *J. Colloid Interf. Sci.*, 300(2):673–687, 2006.
- [30] M.A. Hickner, N.P. Siegel, K.S. Chen, D.S. Hussey, D.L. Jacobson, M. Arif. In Situ High-Resolution Neutron Radiography of Cross-Sectional Liquid Water Profiles in Proton Exchange Membrane Fuel Cells. *J. Electrochem. Soc.*, 155:B427, 2008.

- [31] A.M. Niroumand, M. Saif. Two-phase flow measurement system for polymer electrolyte fuel cells. *J. Power Sources*, 195(10):3250–3255, 2010.
- [32] G. Lin, T.V. Nguyen. Effect of Thickness and Hydrophobic Polymer Content of the Gas Diffusion Layer on Electrode Flooding Level in a PEMFC. *J. Electrochem. Soc.*, 152:A1942–A1948, 2005.
- [33] G.G. Park, Y.J. Sohn, T.H. Yang, Y.G. Yoon, W.Y. Lee, C.S. Kim. Effect of PTFE contents in the gas diffusion media on the performance of PEMFC. *J. Power Sources*, 131:182–187, 2004.
- [34] U. Pasaogullari, C.Y. Wang. Liquid Water Transport in Gas Diffusion Layer of Polymer Electrolyte Fuel Cells. *J. Electrochem. Soc.*, 151:A399–A406, 2004.
- [35] J.H. Nam, M. Kaviany. Effective diffusivity and water-saturation distribution in single-and two-layer PEMFC diffusion medium. *Int. J. Heat Mass Tran.*, 46(24):4595–4611, 2003.
- [36] S. Litster, D. Sinton, N. Djilali. Ex situ visualization of liquid water transport in PEM fuel cell gas diffusion layers. *J. Power Sources*, 154(1):95–105, 2006.
- [37] R. Defay, I. Prigogine. *Surface tension and adsorption*. Wiley, 1966.
- [38] C.M. Hwang, M. Ishida, H. Ito, T. Maeda, A. Nakano, Y. Hasegawa, N. Yokoi, A. Kato, T. Yoshida. Influence of properties of gas diffusion layers on the performance of polymer electrolyte-based unitized reversible fuel cells. *Int. J. Hydrogen Energy*, 36:1740, 2010.
- [39] <http://www.me.mtu.edu/mnit/>.

- [40] V. Konduru. Static and Dynamic Contact Angle Measurement on Rough Surfaces Using Sessile Drop Profile Analysis with Application to Water Management in Low Temperature Fuel Cells. Master’s thesis, Michigan Technological University, 2010.
- [41] N. Parikh, J.S. Allen, R.S. Yassar. Microstructure of Gas Diffusion Layers for PEM Fuel Cells. *Fuel Cells*.
- [42] G. Leinhardt, and S. Leinhardt. Exploratory data analysis: New tools for the analysis of empirical data. *Rev. Res. Educ.*, pages 85–157, 1980.
- [43] M. Sezgin and B.L. Sankur. Survey over image thresholding techniques and quantitative performance evaluation. *J. Electron. Imaging*, 13(1):146–168, 2004.
- [44] N. Otsu. A threshold selection method from gray-level histograms. *Automatica*, 11(285-296):23–27, 1975.
- [45] J.T. Gostick, M.A. Ioannidis, M.W. Fowler, M.D. Pritzker. Wettability and capillary behavior of fibrous gas diffusion media for polymer electrolyte membrane fuel cells. *J. Power Sources*, 194(1):433–444, 2009.
- [46] J.T. Gostick, M.W. Fowler, M.D. Pritzker, M.A. Ioannidis, L.M. Behra. In-plane and through-plane gas permeability of carbon fiber electrode backing layers. *J. Power sources*, 162(1):228–238, 2006.
- [47] E.C. Kumbar, K.V. Sharp, M.M. Mench. Liquid droplet behavior and instability in a polymer electrolyte fuel cell flow channel. *J. Power Sources*, 161(1):333–345, 2006.
- [48] G.M. Whitesides, P.E. Laibinis. Wet chemical approaches to the characteriza-

- tion of organic surfaces: self-assembled monolayers, wetting, and the physical-organic chemistry of the solid-liquid interface. *Langmuir*, 6(1):87–96, 1990.
- [49] J.D. Fairweather, P. Cheung, D.T. Schwartz. The effects of wetproofing on the capillary properties of proton exchange membrane fuel cell gas diffusion layers. *J. Power Sources*, 195(3):787–793, 2010.
- [50] B.R. Jennings, K. Parslow, B.R. Jennings, K. Parslow. Particle size measurement: the equivalent spherical diameter. *Pro. Roy. Soc. London. A. Mathematical and Physical Sciences*, 419(1856):137–149, 1988.
- [51] F.A.L. Dullien, *Porous Media: Fluid Transport and Pore Structure*, 2nd ed., Academic Press, New York, 1992.
- [52] J. Ihonen, M. Mikkola, and G. Lindbergh. Flooding of Gas Diffusion Backing in PEMFCs, Physical and Electrochemical Characterization. *J. Electrochem. Soc.*, 151(8):A1152–A1161, 2004.
- [53] T.L. Liu, C. Pan. Visualization and back pressure analysis of water transport through gas diffusion layers of proton exchange membrane fuel cell. *J. Power Sources*, 2012.
- [54] A. Bazylak, D. Sinton, N. Djilali. Dynamic water transport and droplet emergence in PEMFC gas diffusion layers. *J. Power Sources*, 176(1):240–246, 2008.
- [55] A. Rofaiel, J.S. Ellis, P.R. Challa, A. Bazylak. Heterogeneous through-plane distributions of polytetrafluoroethylene in polymer electrolyte membrane fuel cell gas diffusion layers. *J. Power Sources*, 201:219–225, 2012.
- [56] C. Lim, C.Y. Wang. Effects of hydrophobic polymer content in GDL on power performance of a PEM fuel cell. *Electrochim. Acta*, 49(24):4149–4156, 2004.

- [57] Z. Fishman and A. Bazylak. Heterogeneous Through-Plane Porosity Distributions for Treated PEMFC GDLs I. PTFE Effect. *J. Electrochem. Soc.*, 158:B841, 2011.
- [58] K.G. Gallagher, R.M. Darling, T.W. Patterson, M.L. Perry. Capillary Pressure Saturation Relations for PEM Fuel Cell Gas Diffusion Layers. *J. Electrochem. Soc.*, 155:B1225, 2008.
- [59] A. Faghri and Z. Guo. Challenges and opportunities of thermal management issues related to fuel cell technology and modeling. *Int. J. Heat Mass Transfer*, 48(19):3891–3920, 2005.
- [60] M. Mortazavi and K. Tajiri. Effect of the PTFE content in the gas diffusion layer on water transport in polymer electrolyte fuel cells (PEFCs). *J. Power Sources*, 245:236–244, 2014.
- [61] U. Pasaogullari, C.Y. Wang, K.S. Chen. Two-phase transport in polymer electrolyte fuel cells with bilayer cathode gas diffusion media. *J. Electrochem. Soc.*, 152(8):A1574–A1582, 2005.
- [62] U. Pasaogullari, C.Y. Wang. Two-phase transport and the role of micro-porous layer in polymer electrolyte fuel cells. *Electrochim. Acta*, 49(25):4359–4369, 2004.
- [63] A.Z. Weber and J. Newman. Effects of microporous layers in polymer electrolyte fuel cells. *J. Electrochem. Soc.*, 152:A677, 2005.
- [64] Jon G Pharoah, Brant Peppley, Hasan Atiyeh, Ela Halliop, Kunal Karan, and Aaron Phoenix. Investigating the Role of a Microporous Layer on the Water

- Transport and Performance of a PEMFC. *ECS Transactions*, 3(1):1227–1237, 2006.
- [65] K. Karan, H. Atiyeh, A. Phoenix, E. Halliop, J. Pharoah, and B. Peppley. An experimental investigation of water transport in pemfcs. *Electrochemical and solid-state letters*, 10:B34, 2007.
- [66] H.K. Atiyeh, K. Karan, B. Peppley, A. Phoenix, E. Halliop, and J. Pharoah. Experimental investigation of the role of a microporous layer on the water transport and performance of a pem fuel cell. *J. Power Sources*, 170(1):111–121, 2007.
- [67] Dzmitry Malevich, Ela Halliop, Brant A Peppley, Jon G Pharoah, and Kunal Karan. Investigation of charge-transfer and mass-transport resistances in pemfcs with microporous layer using electrochemical impedance spectroscopy. *J. Electrochem. Soc.*, 156(2):B216–B224, 2009.
- [68] H. Li, Y. Tang, Z. Wang, Z. Shi, S. Wu, D. Song, J. Zhang, K. Fatih, J. Zhang, H. Wang, et al. A review of water flooding issues in the proton exchange membrane fuel cell. *Journal of Power Sources*, 178(1):103–117, 2008.
- [69] R. Lenormand, E. Touboul, C. Zarcone. Numerical models and experiments on immiscible displacements in porous media. *Journal of Fluid Mechanics*, 189:165–187, 1988.
- [70] R. Lenormand. Liquids in porous media. *J. Phys-condens Mat.*, 2:SA79–SA311, 1990.
- [71] E.F. Medici and J.S. Allen. Existence of the phase drainage diagram in pro-

- ton exchange membrane fuel cell fibrous diffusion media. *J. Power Sources*, 191(2):417 – 427, 2009.
- [72] P.K. Das, A. Grippin, A. Kwong, A. Weber. *J. Electrochem. Soc.*, 159:489–496, 2012.
- [73] Yibo Zhou, Kui Jiao, Qing Du, Yan Yin, and Xianguo Li. Gas diffusion layer deformation and its effect on the transport characteristics and performance of proton exchange membrane fuel cell. *Int. J. Hydrogen Energy*, 38(29):12891–12903, 2013.
- [74] Jeff T Gostick, Marios A Ioannidis, Michael W Fowler, and Mark D Pritzker. Pore network modeling of fibrous gas diffusion layers for polymer electrolyte membrane fuel cells. *J. Power Sources*, 173(1):277–290, 2007.
- [75] P.K. Sinha and C.Y. Wang. Pore-network modeling of liquid water transport in gas diffusion layer of a polymer electrolyte fuel cell. *Electrochimica Acta*, 52(28):7936–7945, 2007.
- [76] V.A. Paganin, E.A. Ticianelli, E.R. Gonzalez. Development and electrochemical studies of gas diffusion electrodes for polymer electrolyte fuel cells. *J. Appl. Electrochem.*, 26:297–304, 1996.
- [77] J.M. Song, S.Y. Cha, W.M. Lee, WM. Optimal composition of electrolyte fuel cell electrodes determined by the ac impedance method. *J. Power Sources*, 94(1):78–84, 2001.
- [78] J. Lobato, P. Canizares, M.A. Rodrigo, C. Ruiz-López, J.J. Linares. Influence of the Teflon loading in the gas diffusion layer of PBI-based PEM fuel cells. *J. Appl. Electrochem.*, 38(6):793–802, 2008.

- [79] S. Ge, C.Y. Wang. Liquid water formation and transport in the pefc anode. *J. Electrochem. Soc.*, 154(10):B998–B1005, 2007.
- [80] W. Dai, H. Wang, X.Z. Yuan, J. Martin, J. Shen, M. Pan, Z. Luo. *J. Power Sources*, 188(1):122–126, 2009.
- [81] X. Li, F. Feng, K. Zhang, S. Ye, D.Y. Kwok, V. Birss. Wettability of  $\text{Na}^+$ -ion and  $\text{Na}^+$ -ion/VulcanCarbonCompositeFilms. *Langmuir*, 28 : 6698 – 6705, 2012.
- [82] Jiabin Ge, Andrew Higier, and Hongtan Liu. Effect of gas diffusion layer compression on pem fuel cell performance. *Journal of Power Sources*, 159(2):922–927, 2006.
- [83] IS Hussaini and CY Wang. Measurement of relative permeability of fuel cell diffusion media. *Journal of Power Sources*, 195(12):3830–3840, 2010.
- [84] A. Bazylak, D. Sinton, Z.S. Liu, N. Djilali. Effect of compression on liquid water transport and microstructure of PEMFC gas diffusion layers. *J. Power Sources*, 163(2):784–792, 2007.
- [85] Z. Qi and A. Kaufman. Improvement of water management by a microporous sublayer for PEM fuel cells. *J. Power Sources*, 109(1):38–46, 2002.
- [86] L. Giorgi, E. Antolini, A. Pozio, and E. Passalacqua. *Electrochim. Acta*, 43(24):3675–3680, 1998.
- [87] L.R Jordan, A.K Shukla, T Behrsing, N.R Avery, B.C Muddle, and M Forsyth. Diffusion layer parameters influencing optimal fuel cell performance. *J. Power Sources*, 86(12):250 – 254, 2000.



- [88] D. Bevers, R. Rogers, M.V. Bradke. *J. Power Sources*, 63(2):193–201, 1996.
- [89] O.S. Burheim, J.G. Pharoah, H. Lampert, P.J. Vie, S. Kjelstrup. *J. Fuel Cell Sci. Tech.*, 8(2), 2011.
- [90] J.P. Owejan, T.A. Trabold, D.L. Jacobson, M. Arif, S.G. Kandlikar. Effects of flowfield and diffusion layer properties on water accumulation in a PEM fuel cell. *Int. J. Hydrogen Energy*, 32(17):4489–4502, 2007.
- [91] M.M. Mench, Q.L. Dong, C.Y. Wang. In situ water distribution measurements in a polymer electrolyte fuel cell. *J. Power Sources*, 124(1):90–98, 2003.
- [92] X.G. Yang, N. Burke, C.Y. Wang, K. Tajiri, K. Shinohara. Simultaneous measurements of species and current distributions in a pefc under low-humidity operation. *J. Electrochem. Soc.*, 152:A759–A766, 2005.
- [93] P.K. Sinha, P. Halleck, C.Y. Wang. Quantification of Liquid Water Saturation in a PEM Fuel Cell Diffusion Medium Using X-ray Microtomography. *Electrochem. Solid St.*, 9(7):A344–A348, 2006.
- [94] S.J. Lee, N.Y. Lim, S. Kim, G.G. Park, C.S. Kim. X-ray imaging of water distribution in a polymer electrolyte fuel cell. *J. Power Sources*, 185(2):867–870, 2008.
- [95] T.C. Wu, N. Djilali. Experimental investigation of water droplet emergence in a model polymer electrolyte membrane fuel cell microchannel.
- [96] C.N. Lam, N. Kim, D. Hui, D.Y. Kwok, M.L. Hair, A.W. Neumann. *Colloid Surface A*, 189(1):265–278, 2001.
- [97] J.S. Allen. *J. Colloid Interf. Sci.*, 261(2):481–489, 2003.

- [98] G. Velayutham, J. Kaushik, N. Rajalakshmi, K.S. Dhathathreyan. *Fuel Cells*, 7(4):314–318, 2007.
- [99] A.J. Appleby. Issues in fuel cell commercialization. *Journal of Power Sources*, 58(2):153–176, 1996.
- [100] X. Liu, H. Guo, C. Ma. Water flooding and two-phase flow in cathode channels of proton exchange membrane fuel cells. *J. Power Sources*, 156(2):267–280, 2006.
- [101] R. Anderson, L. Zhang, Y. Ding, M. Blanco, X. Bi, and D.P. Wilkinson. A critical review of two-phase flow in gas flow channels of proton exchange membrane fuel cells. *J. Power Sources*, 195(15):4531–4553, 2010.
- [102] S.G. Kandlikar, W.J. Grande. Evolution of microchannel flow passages—thermohydraulic performance and fabrication technology. *Heat Transfer Eng.*, 24(1):3–17, 2003.
- [103] S. Wongwises, M. Pipathattakul. Flow pattern, pressure drop and void fraction of two-phase gas-liquid flow in an inclined narrow annular channel. *Exp. Therm Fluid Sci.*, 30(4):345–354, 2006.
- [104] S. Saisorn, S. Wongwises. Flow pattern, void fraction and pressure drop of two-phase air-water flow in a horizontal circular micro-channel. *Exp. Therm Fluid Sci.*, 32(3):748–760, 2008.
- [105] A. Kawahara, P.M.-Y. Chung, M. Kawaji. Investigation of two-phase flow pattern, void fraction and pressure drop in a microchannel. *Int. J. Multiphas Flow*, 28(9):1411–1435, 2002.

- [106] S. Saisorn, S. Wongwises. The effects of channel diameter on flow pattern, void fraction and pressure drop of two-phase air-water flow in circular microchannels. *Exp. Therm. Fluid Sci.*, 34(4):454–462, 2010.
- [107] P.M.-Y. Chung and M. Kawaji. The effect of channel diameter on adiabatic two-phase flow characteristics in microchannels. *Int. J. Multiphas. Flow*, 30:735–761, 2004.
- [108] P. Satitchaicharoen and S. Wongwises. Two-phase flow pattern maps for vertical upward gas-liquid flow in mini-gap channels. *Int. J. Multiphas. Flow*, 30(2):225–236, 2004.
- [109] S. Saisorn, S. Wongwises. An experimental investigation of two-phase air-water flow through a horizontal circular micro-channel. *Exp. Thermal Fluid Sci.*, 33(2):306–315, 2009.
- [110] Hideo Ide and Hirohisa Matsumura. Frictional pressure drops of two-phase gas-liquid flow in rectangular channels. *Exp. Therm. Fluid Sci.*, 3(4):362–372, 1990.
- [111] M.W. Wambsganss, J.A. Jendrzeczyk, D.M. France. Two-phase flow patterns and transitions in a small, horizontal, rectangular channel. *Int. J. Multiphas flow*, 17:327–342, 1991.
- [112] B. Lowry, M. Kawaji. Adiabatic vertical two-phase flow in narrow flow channels. *AIChE Symposium Series*, 84:133–139, 1988.
- [113] M. Venkatesan, S.K. Das, A.R. Balakrishnan. Effect of diameter on two-phase pressure drop in narrow tubes. *Exp. Therm. Fluid Sci.*, 35(3):531–541, 2011.

- [114] C.W. Choi, D.I. Yu, M.H. Kim. Adiabatic two-phase flow in rectangular microchannels with different aspect ratios: Part I - Flow pattern, pressure drop and void fraction. *Int. J. Heat Mass Tran.*, 54:616–624, 2011.
- [115] C.C. Wang, K.S. Yang, Y.J. Chang, D.C. Lu. Characteristics of air-water two-phase flow in a 3-mm smooth tube. *Can. J. Chem. Eng.*, 78(5):1011–1016, 2000.
- [116] JL Xu, P Cheng, and TS Zhao. Gas-liquid two-phase flow regimes in rectangular channels with mini/micro gaps. *Int. J. Multiphas. Flow*, 25(3):411–432, 1999.
- [117] J. Pettersen. Flow vaporization of co2 in microchannel tubes. *Exp. Therm. Fluid Sci.*, 28:111–121, 2004.
- [118] T.S. Zhao, Q.C. Bi. Co-current air-water two-phase flow patterns in vertical triangular microchannels. *Int. J. Multiphas. Flow*, 27(5):765–782, 2001.
- [119] K.A. Triplett, S.M. Ghiaasiaan, S.I. Abdel-Khalik, A. LeMouel, B.N. McCord. Gas liquid two-phase flow in microchannels: Part II: void fraction and pressure drop. *Int J. of Multiphas. Flow*, 25:395–410, 1999.
- [120] L. Zhang, H.T. Bi, D.P. Wilkinson, J. Stumper, H. Wang. Gas flow rate distributions in parallel minichannels for polymer electrolyte membrane fuel cells: Experiments and theoretical analysis. *Journal of Power Sources*, 195(10):3231–3239, 2010.
- [121] S.D. Knights, K.M. Colbow, J.S. Pierre, D.P. Wilkinson. Aging mechanisms and lifetime of PEFC and DMFC. *J. Power Sources*, 127:127–134, 2004.
- [122] Thomas A Trabold. Minichannels in polymer electrolyte membrane fuel cells. *Heat Transfer Eng.*, 26(3):3–12, 2005.

- [123] J. Chen. Experimental study on the two phase flow behavior in PEM fuel cell parallel channels with porous media inserts. *J. Power Sources*, 195(4):1122–1129, 2010.
- [124] S.G. Kandlikar, Z. Lu, W.E. Domigan, A.D. White, M.W. Benedict. Measurement of flow maldistribution in parallel channels and its application to ex-situ and in-situ experiments in pemfc water management studies. *Int. J. Heat Mass Tran.*, 52:1741–1752, 2009.
- [125] I. Manke, Ch. Hartnig, M. Grünerbel, W. Lehnert, N. Kardjilov, A. Haibel, A. Hilger, J. Banhart, and H. Riesemeier. Investigation of water evolution and transport in fuel cells with high resolution synchrotron x-ray radiography. *Applied Physics Letters*, 90(17):174105–174105, 2007.
- [126] A. Kariyasaki, T. Fukano, A. Ousaka, M. Kagawa. Characterization of time-varying void fraction in isothermal air-water co-current flow in horizontal capillary tube. *Trans. JSME*, pages 4036–4043, 1991.
- [127] S.M. Zivi. Estimation of steady-state steam void-fraction by means of the principle of minimum entropy production. *J. Heat Transfer. AMSE*, 86:247–252, 1964.
- [128] K.I. Choi, A.S. Pamitran, C.Y. Oh, J.T. Oh. Two-phase pressure drop of R-410A in horizontal smooth minichannels. *Int. J. Refrig.*, 31:119–129, 2008.
- [129] R.W. Lockhart, R.C. Martinelli. Proposed correlation of data for isothermal two-phase, two-components flow in pipes. *Chemical Eng Prog*, 45:39–48, 1949.
- [130] Z.Y. Bao, M.G. Bosnich, B.S. Haynes. Estimation of void fraction and pressure

- drop for two-phase flow in fine passages. *Chemical Engineering Research and Design*, 72:625–632, 1994.
- [131] S.D. Chang, S.T. Ro. Pressure drop of pure HFC refrigerants and their mixtures flowing in capillary tubes. *Int. J. Multiphas. flow*, 22:551–561, 1996.
- [132] Y.Y. Yan, T.F. Lin. Evaporation heat transfer and pressure drop of refrigerant R-134a in a small pipe. *Int. J. Heat Mass Tran.*, 41(24):4183–4194, 1998.
- [133] C.C. Wang, S.K. Chiang, Y.J. Chang, T.W. Chung. Two-Phase Flow Resistance of Refrigerants R-22, R-410A and R-407C in Small Diameter Tubes. *Chem. Eng. Res. Des.*, 79(5):553–560, 2001.
- [134] I.Y. Chen, K.S. Yang, Y.J. Chang, C.C. Wang. Two-phase pressure drop of air-water and R-410A in small horizontal tubes. *Int. J. Multiphas. Flow*, 27(7):1293–1299, 2001.
- [135] M. Zhang, R.L. Webb. Correlation of two-phase friction for refrigerants in small-diameter tubes. *Exp. Therm. Fluid Sci.*, 25:131–139, 2001.
- [136] W. Yu, D.M. France, M.W. Wambsganss, J.R. Hull. Two-phase pressure drop, boiling heat transfer, and critical heat flux to water in a small-diameter horizontal tube. *Int. J. Multiphas. Flow*, 28(6):927–941, 2002.
- [137] E.P. Bandarra Filho, J.M. Saiz Jabardo, P.E.L. Barbieri. Convective boiling pressure drop of refrigerant r-134a in horizontal smooth and microfin tubes. *Int. J. Refrig.*, 27(8):895–903, 2004.
- [138] A. Greco, G.P. Vanoli. Evaporation of refrigerants in a smooth horizontal tube: prediction of R22 and R507 heat transfer coefficients and pressure drop. *Appl. Therm. Eng.*, 24:2189 – 2206, 2004.

- [139] J. Wongsangam, T. Nualboonrueng, S. Wongwises. Performance of smooth and micro-fin tubes in high mass flux region of R-134a during evaporation. *Heat Mass Transfer*, 40:425–435, 2004.
- [140] K. Choi, A.S. Pamitran. Effect of boiling heat transfer of horizontal smooth minichannel for R-410A and R-407C. *J. Mech. Sci. Tech.*, 19:156–163, 2005.
- [141] K. Pehlivan, I. Hassan, M. Vaillancourt. Experimental study on two-phase flow and pressure drop in millimeter-size channels. *Appl. Therm. Eng.*, 26:1506–1514, 2006.
- [142] I.Y. Chen, Y.M. Chen, J.S. Liaw, C.C. Wang. Two-phase frictional pressure drop in small rectangular channels. *Exp. Therm. Fluid Sci.*, 32(1):60–66, 2007.
- [143] A.W. Mauro, J.M. Moreno, R. Mastrullo, J.R. Thome. Comparison of experimental pressure drop data for two phase flows to prediction methods using a general model. *Int. J. Refrig.*, 30(8):1358–1367, 2007.
- [144] C.Y. Lee, S.Y. Lee. Pressure drop of two-phase plug flow in round mini-channels: Influence of surface wettability. *Exp. Therm. Fluid Sci.*, 32(8):1716–1722, 2008.
- [145] T.N. Tran, M.C. Chyu, M.W. Wambsganss, D.M. France. Two-phase pressure drop of refrigerants during flow boiling in small channels: an experimental investigation and correlation development. *Int. J. Multiphas. Flow*, 26(11):1739–1754, 2000.
- [146] R.J. da Silva Lima, J.M. QuibÃ©n, C. Kuhn, T. Boyman, J.R. Thome. Ammonia two-phase flow in a horizontal smooth tube: Flow pattern observations, diabatic and adiabatic frictional pressure drops and assessment of prediction methods. *Int. J. Heat Mass Tran.*, 52:2273 – 2288, 2009.

- [147] H.T. Hu, G.L. Ding, X.C. Huang, B. Deng, Y.F. Gao. Pressure drop during horizontal flow boiling of R410A/oil mixture in 5 mm and 3 mm smooth tubes. *Appl. Therm. Eng.*, 29(16):3353–3365, 2009.
- [148] J. Kaew-On, S. Wongwises. Experimental investigation of evaporation heat transfer coefficient and pressure drop of R-410A in a multiport mini-channel. *Int. J. Refrig.*, 32(1):124–137, 2009.
- [149] J.M. Quiben, L. Cheng, R.J. da Silva Lima, J.R. Thome. Flow boiling in horizontal flattened tubes: Part I - Two-phase frictional pressure drop results and model. *Int. J. Heat Mass Tran.*, 52:3634–3644, 2009.
- [150] J. Wu, T. Koettig, Ch. Franke, D. Helmer, T. Eisel, F. Haug, J. Bremer. Investigation of heat transfer and pressure drop of CO<sub>2</sub> two-phase flow in a horizontal minichannel. *Int. J. Heat Mass Tran.*, 54:2154–2162, 2011.
- [151] Sira Saisorn and Somchai Wongwises. Two-phase air-water flow in micro-channels: An investigation of the viscosity models for pressure drop prediction. *Int. Commun. Heat Mass*, 38(2):212–217, 2011.
- [152] W.H. McAdams, W.K. Woods, L.C. Heroman. Vaporization inside horizontal tubes. *Trans. ASME*, 64:193–200, 1942.
- [153] W.W. Akers, H.A. Deans, O.K. Crosser. Condensing heat transfer within horizontal tubes. *Chem. Eng. Prog.*, 54:89–90, 1958.
- [154] A. Cicchitti, C. Lombardi, M. Silvestri, G. Soldaini, R. Zavalluilli. Two-phase cooling experiments-pressure drop, heat transfer and burnout measurements. *Energia nucleare*, 7:407–425, 1960.



- [155] W.L. Owens. Two-phase pressure gradient. *Int. Dev. Heat Transfer, Pt. II.*, ASME New York, 1961.
- [156] A.E. Dukler, M. Wicks, R.G. Cleaveland. Pressure drop and hold up in two-phase flow. *AIChE J.*, 10:38–51, 1964.
- [157] D.R.H. Beattie, P.B. Whalley. A simple two-phase frictional pressure drop calculation method. *Int. J. Multiphas Flow*, 8:83–87, 1982.
- [158] S. Lin, C.C.K. Kwok, R.Y. Li, Z.H. Chen, Z.Y. Chen. Local frictional pressure drop during vaporization of R-12 through capillary tubes. *Int. J. Multiphas. Flow*, 17:95–102, 1991.
- [159] S.M. Kim and I. Mudawar. Universal approach to predicting two-phase frictional pressure drop for mini/micro-channel saturated flow boiling. *Int. J. Heat Mass Tran.*, 58:718–734, 2013.
- [160] J. Lee, I. Mudawar. Two-phase flow in high-heat-flux micro-channel heat sink for refrigeration cooling applications: Part I-pressure drop characteristics. *Int. J. Heat Mass Transfer*, 48(5):928–940, 2005.
- [161] S. Saisorn, S. Wongwises. An inspection of viscosity model for homogeneous two-phase flow pressure drop prediction in a horizontal circular micro-channel. *Int. Commun. Heat Mass*, 35(7):833–838, 2008.
- [162] Chiwoong Choi and Moohwan Kim. Flow pattern based correlations of two-phase pressure drop in rectangular microchannels. *Int. J. Heat Fluid Flow*, 32(6):1199–1207, 2011.
- [163] R.K. Shah, A.L. London. *Laminar Flow Forced Convection in Ducts*. Academic Press, New York, 1978.

- [164] C.C. Wang, C.S. Chiang, D.C. Lu. Visual observation of two-phase flow pattern of R-22, R-134a, and R-407C in a 6.5-mm smooth tube. *Exp. Therm. Fluid Sci.*, 15(4):395 – 405, 1997.
- [165] L. Friedel. Improved friction pressure drop correlations for horizontal and vertical two-phase pipe flow. *European Two-Phase Group Meeting, Ispra, Italy, Paper E2*, 1979.
- [166] H Müller-Steinhagen and K Heck. A simple friction pressure drop correlation for two-phase flow in pipes. *Chem. Eng. Process*, 20(6):297–308, 1986.
- [167] Licheng Sun and Kaichiro Mishima. Evaluation analysis of prediction methods for two-phase flow pressure drop in mini-channels. *Int. J. Multiphas. Flow*, 35(1):47–54, 2009.
- [168] G. Ribatski, L. Wojtan, J.R. Thome. An analysis of experimental data and prediction methods for two-phase frictional pressure drop and flow boiling heat transfer in micro-scale channels. *Exp. Therm. Fluid Sci.*, 31(1):1–19, 2006.
- [169] D.S. Jung, R. Radermacher. Prediction of pressure drop during horizontal annular flow boiling of pure and mixed refrigerants. *Int. J. Heat Mass Tran.*, 32:2435–2446, 1989.
- [170] K. Mishima, T. Hibiki. Some characteristics of air-water two-phase flow in small diameter vertical tubes. *Int. J. Multiphas. Flow*, 22:703–712, 1996.
- [171] Wambsganss. Frictional pressure gradient in two-phase flow in a small horizontal rectangular channel. *Exp. Therm. Fluid Sci.*, 5:40–56, 1992.
- [172] C-Y. Yang and R.L. Webb. Friction pressure drop of r-12 in small hydraulic

- diameter extruded aluminum tubes with and without micro-fins. *Int. J. Heat Mass Tran.*, 39(4):801–809, 1996.
- [173] H.L. Lee, S.Y. Lee. Pressure drop correlations for two-phase flow within horizontal rectangular channels with small heights. *Int. J. Multiphas. Flow*, 27:783–796, 2001.
- [174] Yun Wook Hwang and Min Soo Kim. The pressure drop in microtubes and the correlation development. *Int. J. Heat Mass Tran.*, 49:1804–1812, 2006.
- [175] Wei Li and Zan Wu. A general correlation for adiabatic two-phase pressure drop in micro/mini-channels. *Int. J. Heat Mass Tran.*, 53:2732–2739, 2010.
- [176] Wei Li and Zan Wu. Generalized adiabatic pressure drop correlations in evaporative micro/mini-channels. *Exp. Therm. Fluid Sci.*, 35(6):866–872, 2011.
- [177] W. Zhang, T. Hibiki, and K. Mishima. Correlations of two-phase frictional pressure drop and void fraction in mini-channel. *Int. J. Heat Mass Tran.*, 53:453–465, 2010.
- [178] D Chisholm. Pressure gradients due to friction during the flow of evaporating two-phase mixtures in smooth tubes and channels. *Int. J. Heat Mass Tran.*, 16(2):347–358, 1972.
- [179] P. Concus and R. Finn. On the behavior of a capillary surface in a wedge. *Proceedings of the National Academy of Science*, 63:292–299, 1969.
- [180] Paul Rodatz, Felix BÃÄ¼chi, Chris Onder, and Lino Guzzella. Operational aspects of a large pefc stack under practical conditions. *J. Power Sources*, 128(2):208–217, 2004.

- [181] F. Barbir, H. Gorgun, X. Wang. Relationship between pressure drop and cell resistance as a diagnostic tool for pem fuel cells. *J. Power Sources*, 141:96–101, 2005.
- [182] Jeffrey S. Allen. Two phase flow in small channels and the implications for pem fuel cell operation. *ECS Transactions*, 3:1197–1206, 2006.
- [183] H.P. Ma, H.M. Zhang, J. Hu, Y.H. Cai, and B.L. Yi. Diagnostic tool to detect liquid water removal in the cathode channels of proton exchange membrane fuel cells. *J. Power Sources*, 162(1):469–473, 2006.
- [184] H. Yamada, T. Hatanaka, H. Murata, Y. Morimoto. Measurement of flooding in gas diffusion layers of polymer electrolyte fuel cells with conventional flow field. *J. Electrochem. Soc.*, 153 (9):A1748–A1754, 2006.
- [185] Xianguo Li, Imran Sabir, and Jaewan Park. A flow channel design procedure for pem fuel cells with effective water removal. *J. Power Sources*, 163(2):933–942, 2007.
- [186] Kohei Ito, Kensuke Ashikaga, Hiromitsu Masuda, Toshihiro Oshima, Yasushi Kakimoto, and Kazunari Sasaki. Estimation of flooding in pemfc gas diffusion layer by differential pressure measurement. *J. Power Sources*, 175(2):732–738, 2008.
- [187] SG Kandlikar, Z. Lu, TY Lin, D. Cooke, and M. Daino. Uneven gas diffusion layer intrusion in gas channel arrays of proton exchange membrane fuel cell and its effects on flow distribution. *J. Power Sources*, 194(1):328–337, 2009.
- [188] Xiao Yu, Ming Pingwen, Hou Ming, Yi Baolian, and Zhi-Gang Shao. The

- critical pressure drop for the purge process in the anode of a fuel cell. *J. Power Sources*, 188(1):163–169, 2009.
- [189] Shou-Shing Hsieh, Yi-Ji Huang, and Bing-Shyan Her. Pressure drop on water accumulation distribution for a micro pem fuel cell with different flow field plates. *Int. J. Heat Mass Tran.*, 52:5657–5659, 2009.
- [190] J. Chen. Dominant frequency of pressure drop signal as a novel diagnostic tool for the water removal in proton exchange membrane fuel cell flow channel. *J. Power Sources*, 195(4):1177–1181, 2010.
- [191] Ryan Anderson, David Wilkinson, Xiaotao Bi, and Lifeng Zhang. Two-phase flow pressure drop hysteresis under typical operating conditions for a proton exchange membrane fuel cell. *ECS Transactions*, 28(30):127–137, 2010.
- [192] J. Dillet, O. Lottin, G. Maranzana, S. Didierjean, D. Conteau, C. Bonnet. Direct observation of the two-phase flow in the air channel of a proton exchange membrane fuel cell and of the effects of a clogging/unclogging sequence on the current density distribution. *J. Power Sources*, 195(9):2795 – 2799, 2010.
- [193] Dusan Spornjak, Ajay K. Prasad, and Suresh G. Advani. In situ comparison of water content and dynamics in parallel, single-serpentine, and interdigitated flow fields of polymer electrolyte membrane fuel cells. *J. Power Sources*, 195(11):3553 – 3568, 2010.
- [194] C.E. Colosqui, M.J. Cheah, I.G. Kevrekidis, and J.B. Benziger. Droplet and slug formation in polymer electrolyte membrane fuel cell flow channels: The role of interfacial forces. *J. Power Sources*, 196(23):10057–10068, 2011.

- [195] Vijay Radhakrishnan and Prathap Haridoss. Effect of gdl compression on pressure drop and pressure distribution in pemfc flow field. *Int. J. Hydrogen Energy*, 36(22):14823–14828, 2011.
- [196] Kui Jiao, Ibrahim E. Alaefour, Gholamreza Karimi, and Xianguo Li. Cold start characteristics of proton exchange membrane fuel cells. *Int. J. Hydrogen Energy*, 36(18):11832–11845, 2011.
- [197] Rodolfo Taccani and Nicola Zuliani. Effect of flow field design on performances of high temperature pem fuel cells: Experimental analysis. *Int. J. Hydrogen Energy*, 36(16):10282–10287, 2011.
- [198] J. Bachman, M. Charvet, A. Santamaria, H.Y. Tang, J.W. Park, R. Walker. Experimental investigation of the effect of channel length on performance and water accumulation in a PEMFC parallel flow field. *Int. J. Hydrogen Energy*, 37(22):17172 – 17179, 2012.
- [199] Xianguo Li and Imran Sabir. Review of bipolar plates in PEM fuel cells: Flow-field designs. *Int. J. Hydrogen Energy*, 30(4):359–371, 2005.
- [200] Frano Barbir. *PEM fuel cells: theory and practice*. Access Online via Elsevier, 2012.
- [201] Xianguo Li. *Principles of fuel cells*. Taylor Francis, 2006.
- [202] T.V. Nguyen and W. He. *Handbook of Fuel Cells*. John Wiley Sons Ltd., 2003.
- [203] Cody D Rath and Satish G Kandlikar. Liquid filling in a corner with a fibrous wallâan application to two-phase flow in pem fuel cell gas channels. *Colloids and Surfaces A: Physicochemical and Engineering Aspects*, 384(1):653–660, 2011.

- [204] F.B. Weng, A. Su, and C.Y. Hsu. The study of the effect of gas stoichiometric flow rate on the channel flooding and performance in a transparent fuel cell. *International journal of hydrogen energy*, 32(6):666–676, 2007.
- [205] T. Ous and C. Arcoumanis. Visualisation of water accumulation in the flow channels of pemfc under various operating conditions. *Journal of Power Sources*, 187(1):182–189, 2009.
- [206] MA Hickner, NP Siegel, KS Chen, DN McBrayer, DS Hussey, DL Jacobson, and M. Arif. Real-time imaging of liquid water in an operating proton exchange membrane fuel cell. *Journal of the Electrochemical Society*, 153:A902, 2006.
- [207] J.P. Owejan, J.J. Gagliardo, J.M. Sergi, S.G. Kandlikar, and T.A. Trabold. Water management studies in pem fuel cells, part i: Fuel cell design and in situ water distributions. *international journal of hydrogen energy*, 34(8):3436–3444, 2009.
- [208] X. Liu, H. Guo, F. Ye, and C.F. Ma. Flow dynamic characteristics in flow field of proton exchange membrane fuel cells. *International journal of hydrogen energy*, 33(3):1040–1051, 2008.
- [209] Zhigang Zhan, Chen Wang, Weiguo Fu, and Mu Pan. Visualization of water transport in a transparent pemfc. *International Journal of Hydrogen Energy*, 37(1):1094–1105, 2012.
- [210] Mathieu Paquin and Luc G Fr  chette. Understanding cathode flooding and dry-out for water management in air breathing pem fuel cells. *Journal of Power Sources*, 180(1):440–451, 2008.
- [211] Wei-Mon Yan, Xiao-Dong Wang, Sen-Sin Mei, Xiao-Feng Peng, Yi-Fan Guo,

- and Ay Su. Effects of operating temperatures on performance and pressure drops for a 256cm<sup>2</sup> proton exchange membrane fuel cell: An experimental study. *Journal of Power Sources*, 185(2):1040–1048, 2008.
- [212] H. Xu, Y. Song, H.R. Kunz, and J.M. Fenton. Effect of elevated temperature and reduced relative humidity on orr kinetics for pem fuel cells. *Journal of the Electrochemical Society*, 152:A1828, 2005.
- [213] KC Neyerlin, H.A. Gasteiger, C.K. Mittelsteadt, J. Jorne, and W. Gu. Effect of relative humidity on oxygen reduction kinetics in a pemfc. *Journal of The Electrochemical Society*, 152:A1073, 2005.
- [214] EA Wargo, VP Schulz, A. Çeçen, SR Kalidindi, and EC Kumbur. Resolving macro-and micro-porous layer interaction in polymer electrolyte fuel cells using focused ion beam and x-ray computed tomography. *Electrochimica Acta*, 87:201–212, 2012.
- [215] S. Litster and G. McLean. PEM fuel cell electrodes. *J. Power Sources*, 130:61–76, 2004.
- [216] I.E. Baranov, S.A. Grigoriev, D. Ylitalo, V.N. Fateev, I.I. Nikolaev. Transfer processes in PEM fuel cell: Influence of electrode structure . *Int. J. Hydrogen Energy*, 31(2):203–210, 2006.



## Appendix-Copyright Permissions



Mehdi Mortazavi &lt;mortazav@mtu.edu&gt;

---

**Asking for a permission**

---

**Beth Darchi** <DarchiB@asme.org>  
To: Mehdi Mortazavi <mortazav@mtu.edu>

Tue, Jun 24, 2014 at 2:43 PM

Dear Mr. Mortazavi:

It is our pleasure to grant you permission to use all or any part of the ASME paper "In-Plane Microstructure of Gas Diffusion Layer with Different Properties for PEFC," by Mehdi Mortazavi, Kazuya Tajiri, Journal of Fuel Cell Science and Technology, Volume 11(2), 2014, as cited in your letter for inclusion in a PhD dissertation entitled Water transport through porous media and in flow channels of proton exchange membrane fuel cell to be published by Michigan Technological University.

Permission is granted for the specific use as stated herein and does not permit further use of the materials without proper authorization. Proper attribution must be made to the author(s) of the materials. **PLEASE NOTE:** if any or all of the figures and/or Tables are of another source, permission should be granted from that outside source or include the reference of the original source. ASME does not grant permission for outside source material that may be referenced in the ASME works.

As is customary, we request that you ensure full acknowledgment of this material, the author(s), source and ASME as original publisher. Acknowledgment must be retained on all pages printed and distributed.

Many thanks for your interest in ASME publications.

Sincerely,



**Beth Darchi**  
Publishing Administrator  
ASME  
2 Park Avenue, 6th Floor  
New York, NY 10016-5990  
Tel 1.212.591.7700  
[darchib@asme.org](mailto:darchib@asme.org)

Permission to use the material of chapter 2



Mehdi Mortazavi &lt;mortazav@mtu.edu&gt;

---

**Asking for permission to reuse the material of a paper**

---

T. Nejat Veziroglu <veziroglu@iahe.org>  
To: Mehdi Mortazavi <mortazav@mtu.edu>  
Cc: "Emre A. Veziroglu" <emrev1@cox.net>

Tue, Jul 1, 2014 at 3:36 PM

To: Mehdi Mortazavi [mortazav@mtu.edu]

Cc: Emre A. Veziroglu [emrev1@cox.net]

Subject: Copyright permission

Dear Mehdi:

In accordance with your request, we are happy to give you permission to use the following article in your Ph.D. thesis:

Mehdi Mortazavi, Kazuya Tajiri, Liquid water breakthrough pressure through gas diffusion layer of proton exchange membrane fuel cell, International Journal of Hydrogen Energy, Volume 39, Issue 17, 5 June 2014, Pages 9409-9419

Wishing you all the best in your endeavors, I remain

Sincerely yours,

T. Nejat Veziroglu

Founding Editor-in-Chief

International Journal of Hydrogen Energy (IJHE)

5794 SW 40 St. #303

<https://mail.google.com/mail/u/0/?ui=2&ik=1a07065798&view=pt&search=inbox&msg=148f36dae544f41&siml=148f36dae544f41>

1/2

---

Permission to use the material of chapter 3

# ELSEVIER LICENSE TERMS AND CONDITIONS

Jun 18, 2014

This is a License Agreement between Mehdi Mortazavi ("You") and Elsevier ("Elsevier") provided by Copyright Clearance Center ("CCC"). The license consists of your order details, the terms and conditions provided by Elsevier, and the payment terms and conditions.

**All payments must be made in full to CCC. For payment instructions, please see information listed at the bottom of this form.**

Supplier	Elsevier Limited The Boulevard, Langford Lane Kidlington, Oxford, OX5 1GB, UK
Registered Company Number	1982084
Customer name	Mehdi Mortazavi
Customer address	822 R.L. Smith HOUGHTON, MI 49931
License number	3412090934763
License date	Jun 18, 2014
Licensed content publisher	Elsevier
Licensed content publication	Journal of Power Sources
Licensed content title	Effect of the PTFE content in the gas diffusion layer on water transport in polymer electrolyte fuel cells (PEFCs)
Licensed content author	Mehdi Mortazavi, Kazuya Tajiri
Licensed content date	1 January 2014
Licensed content volume number	245
Licensed content issue number	None
Number of pages	9
Start Page	236
End Page	244
Type of Use	reuse in a thesis/dissertation
Portion	full article
Format	both print and electronic
Are you the author of this Elsevier article?	Yes
Will you be translating?	No
Title of your	Water transport through porous media and in flow channels of

<https://s100.copyright.com/AppDispatchServlet>

1/7

Permission to use the material of chapter 4

# ELSEVIER LICENSE TERMS AND CONDITIONS

Jun 18, 2014

This is a License Agreement between Mehdi Mortazavi ("You") and Elsevier ("Elsevier") provided by Copyright Clearance Center ("CCC"). The license consists of your order details, the terms and conditions provided by Elsevier, and the payment terms and conditions.

**All payments must be made in full to CCC. For payment instructions, please see information listed at the bottom of this form.**

Supplier	Elsevier Limited The Boulevard, Langford Lane Kidlington, Oxford, OX5 1GB, UK
Registered Company Number	1982084
Customer name	Mehdi Mortazavi
Customer address	822 R.L. Smith HOUGHTON, MI 49931
License number	3412130373760
License date	Jun 18, 2014
Licensed content publisher	Elsevier
Licensed content publication	International Journal of Multiphase Flow
Licensed content title	Gas-liquid two-phase flow in microchannels Part I: two-phase flow patterns
Licensed content author	K.A. Triplett, S.M. Ghiaasiaan, S.I. Abdel-Khalik, D.L. Sadowski
Licensed content date	April 1999
Licensed content volume number	25
Licensed content issue number	3
Number of pages	18
Start Page	377
End Page	394
Type of Use	reuse in a thesis/dissertation
Intended publisher of new work	other
Portion	figures/tables/illustrations
Number of figures/tables/illustrations	1
Format	both print and electronic

Permission to use Figure 5.1

### Request for Permission to Reproduce or Re-Publish ECS Material

Please fax this form to: The Electrochemical Society (ECS), Attn: Permissions Requests, 1.609.730.0629.  
You may also e-mail your request to: [copyright@electrochem.org](mailto:copyright@electrochem.org). Include all the information as required on this form. Please allow 3-7 days for your request to be processed.

I am preparing a (choose one): ☐ paper ☐ chapter ☐ book ☒ thesis

entitled: Water Transport Through Brine Media and in Flow Channels of proton exchange membrane fuel cell  
to be published by: Michigan Technological University

in an upcoming publication entitled: \_\_\_\_\_

I request permission to use the following material in the publication noted above, and request nonexclusive rights for all subsequent editions and in all foreign language translations for distribution throughout the world.

Description of material to be used—Indicate what material you wish to use (figures, tables, text, etc.) and give the full bibliographic reference for the source publication. You may attach a separate list, organized by ECS title.

Figure 5 of this paper:

Title: Liquid Water Removal From a Polymer Electrolyte Fuel Cell

Authors: F. Y. Zhang, X. G. Yang, C. Y. Wang

Year 2006

Volume 153 Pages A225-A232

Signature: Mortazavi Date: 6/18/2014

Name: Mehdi Mortazavi

Address: 822 R.L. Smith Bldg, Michigan Tech University

1400 Townsend Drive

Houghton, MI 49931

Telephone: 906-370-6360 Fax: \_\_\_\_\_

E-mail: mortazavi@mtu.edu

Permission is granted to reproduce the above-referenced material. Please acknowledge the author(s) and publication data of the original material, and include the words: "Reproduced by permission of The Electrochemical Society."

\_\_\_\_\_  
Date

\_\_\_\_\_  
John Lewis, Associate Director of Publications

Permission to use Figure 5.2



Mehdi Mortazavi &lt;mortazav@mtu.edu&gt;

---

**Asking for permission to reuse the material of a paper**

---

**T. Nejat Veziroglu** <veziroglu@jahe.org>  
To: Mehdi Mortazavi <mortazav@mtu.edu>  
Cc: "Emre A. Veziroglu" <emrev1@cox.net>

Tue, Jun 24, 2014 at 1:28 PM

To: Mehdi Mortazavi [[mortazav@mtu.edu](mailto:mortazav@mtu.edu)]Cc: Emre A. Veziroglu [[emrev1@cox.net](mailto:emrev1@cox.net)]

Subject: Copyright permission

Dear Mehdi:

In accordance with your request, we are happy to give you permission to use the following figures in your Ph.D. thesis:

Title: Water management studies in PEM fuel cells, Part II: Ex situ investigation of flow maldistribution, pressure drop and two-phase flow pattern in gas channels

Year: 2009

Author: Lu, Z. and Kandlikar, SG and Rath, C. and Grimm, M. and Domigan, W. and White, AD and Hardbarger, M. and Owejan, JP and Trabold, TA

Volume: 34

Issue: 8

Pages: 3445-3456

Number of figures to be use: 1

---

Title: Modeling gas flow in PEMFC channels: Part I--Flow pattern transitions and pressure drop in a simulated ex situ channel with uniform water injection through the GDL

Permission to use Figures 5.3, 5.4, 5.7, 5.8, 5.10, and 5.13, continue

Year: 2012

Author: Grimm, Michael and See, Evan J and Kandlikar, Satish G

Volume: 37

Issue:

Pages: 12489-12503

Number of figures to be used: 3

---

Title: Investigation of water droplet kinetics and optimization of channel geometry for PEM fuel cell cathodes

Year: 2009

Author: Nawaz Akhtar, Arshad Qureshi, Joachim Scholta, Christoph Hartnig, Matthias Messerschmidt, and Werner Lehnert

Volume: 34

Issue: 7

Pages: 3104-3111

Number of figures to be used: 2

---

Title: Water management studies in PEM fuel cells, part IV: Effects of channel surface wettability, geometry and orientation on the two-phase flow in parallel gas channels

Year: 2011

Author: Zijie Lu, Cody Rath, Guangsheng Zhang, and Satish G. Kandlikar

Volume: 36

Issue: 16

Pages: 9864-9875

Number of figures to be used: 1

Permission to use Figures 5.3, 5.4, 5.7, 5.8, 5.10, and 5.13



6/24/2014

Michigan Technological University Mail - Asking for permission to reuse the material of a paper

**Title:** Application of water barrier layers in a proton exchange membrane fuel cell for improved water management at low humidity conditions

**Year:** 2011

**Author:** Blanco, M. and Wilkinson, D.P. and Wang, H.

**Volume:** 36

**Issue:**

**Pages:** 3635-3648

**Number of figures to be used:** 1

Wishing you all the best in your endeavors, I remain

Sincerely yours,

T. Nejat Veziroglu

Founding Editor-in-Chief

International Journal of Hydrogen Energy (IJHE)

5794 SW 40 St, #303

Miami, FL 33155, USA

Tel: 1-305-456-9353

Fax: 1-305-675-3295

Email: [veziroglu@ijahe.org](mailto:veziroglu@ijahe.org)

**From:** Mehdi Mortazavi [mailto:[mortazav@mtu.edu](mailto:mortazav@mtu.edu)]

**Sent:** Wednesday, June 18, 2014 6:07 PM

**To:** [veziroglu@ijahe.org](mailto:veziroglu@ijahe.org)

**Subject:** Fwd: Asking for permission to reuse the material of a paper

<https://mail.google.com/mail/u/0/?ui=2&ik=1a07065798&view=pt&search=inbox&msg=146ceabe08e059a4&dsqt=1&siml=146ceabe08e059a4>

3/7

Permission to use Figures 5.3, 5.4, 5.7, 5.8, 5.10, and 5.13, continue

# ELSEVIER LICENSE TERMS AND CONDITIONS

Jun 18, 2014

This is a License Agreement between Mehdi Mortazavi ("You") and Elsevier ("Elsevier") provided by Copyright Clearance Center ("CCC"). The license consists of your order details, the terms and conditions provided by Elsevier, and the payment terms and conditions.

**All payments must be made in full to CCC. For payment instructions, please see information listed at the bottom of this form.**

Supplier	Elsevier Limited The Boulevard, Langford Lane Kidlington, Oxford, OX5 1GB, UK
Registered Company Number	1982084
Customer name	Mehdi Mortazavi
Customer address	822 R.L. Smith HOUGHTON, MI 49931
License number	3412150921586
License date	Jun 18, 2014
Licensed content publisher	Elsevier
Licensed content publication	Electrochimica Acta
Licensed content title	Water flooding and pressure drop characteristics in flow channels of proton exchange membrane fuel cells
Licensed content author	Xuan Liu, Hang Guo, Fang Ye, Chong Fang Ma
Licensed content date	1 March 2007
Licensed content volume number	52
Licensed content issue number	11
Number of pages	8
Start Page	3607
End Page	3614
Type of Use	reuse in a thesis/dissertation
Intended publisher of new work	other
Portion	figures/tables/illustrations
Number of figures/tables/illustrations	2
Format	both print and electronic

<https://s100.copyright.com/AppDispatchServlet>

1/7

Permission to use Figures 5.5 and 5.11

Are you the author of this Elsevier article?	No
Will you be translating?	No
Title of your thesis/dissertation	Water transport through porous media and in flow channels of proton exchange membrane fuel cell
Expected completion date	Jul 2014
Estimated size (number of pages)	200
Elsevier VAT number	GB 494 6272 12
Permissions price	0.00 USD
VAT/Local Sales Tax	0.00 USD / 0.00 GBP
Total	0.00 USD
Terms and Conditions	

### INTRODUCTION

1. The publisher for this copyrighted material is Elsevier. By clicking "accept" in connection with completing this licensing transaction, you agree that the following terms and conditions apply to this transaction (along with the Billing and Payment terms and conditions established by Copyright Clearance Center, Inc. ("CCC"), at the time that you opened your Rightslink account and that are available at any time at <http://myaccount.copyright.com>).

### GENERAL TERMS

2. Elsevier hereby grants you permission to reproduce the aforementioned material subject to the terms and conditions indicated.

3. Acknowledgement: If any part of the material to be used (for example, figures) has appeared in our publication with credit or acknowledgement to another source, permission must also be sought from that source. If such permission is not obtained then that material may not be included in your publication/copies. Suitable acknowledgement to the source must be made, either as a footnote or in a reference list at the end of your publication, as follows:

“Reprinted from Publication title, Vol /edition number, Author(s), Title of article / title of chapter, Pages No., Copyright (Year), with permission from Elsevier [OR APPLICABLE SOCIETY COPYRIGHT OWNER].” Also Lancet special credit - “Reprinted from The Lancet, Vol. number, Author(s), Title of article, Pages No., Copyright (Year), with permission from Elsevier.”

4. Reproduction of this material is confined to the purpose and/or media for which permission is hereby given.

5. Altering/Modifying Material: Not Permitted. However figures and illustrations may be altered/adapted minimally to serve your work. Any other abbreviations, additions, deletions and/or any other alterations shall be made only with prior written authorization of Elsevier Ltd. (Please contact Elsevier at [permissions@elsevier.com](mailto:permissions@elsevier.com))

6. If the permission fee for the requested use of our material is waived in this instance, please be

Permission to use Figures 5.5 and 5.11, continue

# ELSEVIER LICENSE TERMS AND CONDITIONS

Jun 18, 2014

This is a License Agreement between Mehdi Mortazavi ("You") and Elsevier ("Elsevier") provided by Copyright Clearance Center ("CCC"). The license consists of your order details, the terms and conditions provided by Elsevier, and the payment terms and conditions.

**All payments must be made in full to CCC. For payment instructions, please see information listed at the bottom of this form.**

Supplier	Elsevier Limited The Boulevard, Langford Lane Kidlington, Oxford, OX5 1GB, UK
Registered Company Number	1982084
Customer name	Mehdi Mortazavi
Customer address	822 R.L. Smith HOUGHTON, MI 49931
License number	3412151094120
License date	Jun 18, 2014
Licensed content publisher	Elsevier
Licensed content publication	Energy Conversion and Management
Licensed content title	Effect of pressure drop in different flow fields on water accumulation and current distribution for a micro PEM fuel cell
Licensed content author	Shou-Shing Hsieh, Bing-Shyan Her, Yi-Ji Huang
Licensed content date	February 2011
Licensed content volume number	52
Licensed content issue number	2
Number of pages	8
Start Page	975
End Page	982
Type of Use	reuse in a thesis/dissertation
Intended publisher of new work	other
Portion	figures/tables/illustrations
Number of figures/tables/illustrations	1
Format	both print and electronic

Permission to use Figure 5.6

Are you the author of this Elsevier article?	No
Will you be translating?	No
Title of your thesis/dissertation	Water transport through porous media and in flow channels of proton exchange membrane fuel cell
Expected completion date	Jul 2014
Estimated size (number of pages)	200
Elsevier VAT number	GB 494 6272 12
Permissions price	0.00 USD
VAT/Local Sales Tax	0.00 USD / 0.00 GBP
Total	0.00 USD
Terms and Conditions	

### INTRODUCTION

1. The publisher for this copyrighted material is Elsevier. By clicking "accept" in connection with completing this licensing transaction, you agree that the following terms and conditions apply to this transaction (along with the Billing and Payment terms and conditions established by Copyright Clearance Center, Inc. ("CCC"), at the time that you opened your Rightslink account and that are available at any time at <http://myaccount.copyright.com>).

### GENERAL TERMS

2. Elsevier hereby grants you permission to reproduce the aforementioned material subject to the terms and conditions indicated.

3. Acknowledgement: If any part of the material to be used (for example, figures) has appeared in our publication with credit or acknowledgement to another source, permission must also be sought from that source. If such permission is not obtained then that material may not be included in your publication/copies. Suitable acknowledgement to the source must be made, either as a footnote or in a reference list at the end of your publication, as follows:

“Reprinted from Publication title, Vol /edition number, Author(s), Title of article / title of chapter, Pages No., Copyright (Year), with permission from Elsevier [OR APPLICABLE SOCIETY COPYRIGHT OWNER].” Also Lancet special credit - “Reprinted from The Lancet, Vol. number, Author(s), Title of article, Pages No., Copyright (Year), with permission from Elsevier.”

4. Reproduction of this material is confined to the purpose and/or media for which permission is hereby given.

5. Altering/Modifying Material: Not Permitted. However figures and illustrations may be altered/adapted minimally to serve your work. Any other abbreviations, additions, deletions and/or any other alterations shall be made only with prior written authorization of Elsevier Ltd. (Please contact Elsevier at [permissions@elsevier.com](mailto:permissions@elsevier.com))

6. If the permission fee for the requested use of our material is waived in this instance, please be

Permission to use Figure 5.6, continue

# ELSEVIER LICENSE TERMS AND CONDITIONS

Jun 18, 2014

This is a License Agreement between Mehdi Mortazavi ("You") and Elsevier ("Elsevier") provided by Copyright Clearance Center ("CCC"). The license consists of your order details, the terms and conditions provided by Elsevier, and the payment terms and conditions.

**All payments must be made in full to CCC. For payment instructions, please see information listed at the bottom of this form.**

Supplier	Elsevier Limited The Boulevard, Langford Lane Kidlington, Oxford, OX5 1GB, UK
Registered Company Number	1982084
Customer name	Mehdi Mortazavi
Customer address	822 R.L. Smith HOUGHTON, MI 49931
License number	3412160700886
License date	Jun 18, 2014
Licensed content publisher	Elsevier
Licensed content publication	Journal of Power Sources
Licensed content title	Two-phase flow pressure drop hysteresis in parallel channels of a proton exchange membrane fuel cell
Licensed content author	Ryan Anderson, David P. Wilkinson, Xiaotao Bi, Lifeng Zhang
Licensed content date	1 July 2010
Licensed content volume number	195
Licensed content issue number	13
Number of pages	9
Start Page	4168
End Page	4176
Type of Use	reuse in a thesis/dissertation
Intended publisher of new work	other
Portion	figures/tables/illustrations
Number of figures/tables/illustrations	1
Format	both print and electronic

<https://s100.copyright.com/AppDispatchServlet>

1/7

Permission to use Figure 5.9

Are you the author of this Elsevier article?	No
Will you be translating?	No
Title of your thesis/dissertation	Water transport through porous media and in flow channels of proton exchange membrane fuel cell
Expected completion date	Jul 2014
Estimated size (number of pages)	200
Elsevier VAT number	GB 494 6272 12
Permissions price	0.00 USD
VAT/Local Sales Tax	0.00 USD / 0.00 GBP
Total	0.00 USD
Terms and Conditions	

### INTRODUCTION

1. The publisher for this copyrighted material is Elsevier. By clicking "accept" in connection with completing this licensing transaction, you agree that the following terms and conditions apply to this transaction (along with the Billing and Payment terms and conditions established by Copyright Clearance Center, Inc. ("CCC"), at the time that you opened your Rightslink account and that are available at any time at <http://myaccount.copyright.com>).

### GENERAL TERMS

2. Elsevier hereby grants you permission to reproduce the aforementioned material subject to the terms and conditions indicated.

3. Acknowledgement: If any part of the material to be used (for example, figures) has appeared in our publication with credit or acknowledgement to another source, permission must also be sought from that source. If such permission is not obtained then that material may not be included in your publication/copies. Suitable acknowledgement to the source must be made, either as a footnote or in a reference list at the end of your publication, as follows:

“Reprinted from Publication title, Vol /edition number, Author(s), Title of article / title of chapter, Pages No., Copyright (Year), with permission from Elsevier [OR APPLICABLE SOCIETY COPYRIGHT OWNER].” Also Lancet special credit - “Reprinted from The Lancet, Vol. number, Author(s), Title of article, Pages No., Copyright (Year), with permission from Elsevier.”

4. Reproduction of this material is confined to the purpose and/or media for which permission is hereby given.

5. Altering/Modifying Material: Not Permitted. However figures and illustrations may be altered/adapted minimally to serve your work. Any other abbreviations, additions, deletions and/or any other alterations shall be made only with prior written authorization of Elsevier Ltd. (Please contact Elsevier at [permissions@elsevier.com](mailto:permissions@elsevier.com))

6. If the permission fee for the requested use of our material is waived in this instance, please be

Permission to use Figure 5.9, continue

**ELSEVIER LICENSE  
TERMS AND CONDITIONS**

Jun 18, 2014

---

This is a License Agreement between Mehdi Mortazavi ("You") and Elsevier ("Elsevier") provided by Copyright Clearance Center ("CCC"). The license consists of your order details, the terms and conditions provided by Elsevier, and the payment terms and conditions.

**All payments must be made in full to CCC. For payment instructions, please see information listed at the bottom of this form.**

Supplier	Elsevier Limited The Boulevard, Langford Lane Kidlington, Oxford, OX5 1GB, UK
Registered Company Number	1982084
Customer name	Mehdi Mortazavi
Customer address	822 R.L. Smith HOUGHTON, MI 49931
License number	3412160938345
License date	Jun 18, 2014
Licensed content publisher	Elsevier
Licensed content publication	Journal of Power Sources
Licensed content title	Visualization and quantification of cathode channel flooding in PEM fuel cells
Licensed content author	Irfan S. Hussaini, Chao-Yang Wang
Licensed content date	15 February 2009
Licensed content volume number	187
Licensed content issue number	2
Number of pages	8
Start Page	444
End Page	451
Type of Use	reuse in a thesis/dissertation
Intended publisher of new work	other
Portion	figures/tables/illustrations
Number of figures/tables/illustrations	1
Format	both print and electronic

<https://s100.copyright.com/AppDispatchServlet>

1/7

Permission to use Figure 5.12



Are you the author of this Elsevier article?	No
Will you be translating?	No
Title of your thesis/dissertation	Water transport through porous media and in flow channels of proton exchange membrane fuel cell
Expected completion date	Jul 2014
Estimated size (number of pages)	200
Elsevier VAT number	GB 494 6272 12
Permissions price	0.00 USD
VAT/Local Sales Tax	0.00 USD / 0.00 GBP
Total	0.00 USD
Terms and Conditions	

### INTRODUCTION

1. The publisher for this copyrighted material is Elsevier. By clicking "accept" in connection with completing this licensing transaction, you agree that the following terms and conditions apply to this transaction (along with the Billing and Payment terms and conditions established by Copyright Clearance Center, Inc. ("CCC"), at the time that you opened your Rightslink account and that are available at any time at <http://myaccount.copyright.com>).

### GENERAL TERMS

2. Elsevier hereby grants you permission to reproduce the aforementioned material subject to the terms and conditions indicated.

3. Acknowledgement: If any part of the material to be used (for example, figures) has appeared in our publication with credit or acknowledgement to another source, permission must also be sought from that source. If such permission is not obtained then that material may not be included in your publication/copies. Suitable acknowledgement to the source must be made, either as a footnote or in a reference list at the end of your publication, as follows:

“Reprinted from Publication title, Vol /edition number, Author(s), Title of article / title of chapter, Pages No., Copyright (Year), with permission from Elsevier [OR APPLICABLE SOCIETY COPYRIGHT OWNER].” Also Lancet special credit - “Reprinted from The Lancet, Vol. number, Author(s), Title of article, Pages No., Copyright (Year), with permission from Elsevier.”

4. Reproduction of this material is confined to the purpose and/or media for which permission is hereby given.

5. Altering/Modifying Material: Not Permitted. However figures and illustrations may be altered/adapted minimally to serve your work. Any other abbreviations, additions, deletions and/or any other alterations shall be made only with prior written authorization of Elsevier Ltd. (Please contact Elsevier at [permissions@elsevier.com](mailto:permissions@elsevier.com))

6. If the permission fee for the requested use of our material is waived in this instance, please be

Permission to use Figure 5.12, continue

# ELSEVIER LICENSE TERMS AND CONDITIONS

Jun 18, 2014

This is a License Agreement between Mehdi Mortazavi ("You") and Elsevier ("Elsevier") provided by Copyright Clearance Center ("CCC"). The license consists of your order details, the terms and conditions provided by Elsevier, and the payment terms and conditions.

**All payments must be made in full to CCC. For payment instructions, please see information listed at the bottom of this form.**

Supplier	Elsevier Limited The Boulevard, Langford Lane Kidlington, Oxford, OX5 1GB, UK
Registered Company Number	1982084
Customer name	Mehdi Mortazavi
Customer address	822 R.L. Smith HOUGHTON, MI 49931
License number	3412161181946
License date	Jun 18, 2014
Licensed content publisher	Elsevier
Licensed content publication	Journal of Power Sources
Licensed content title	Gas-liquid two-phase flow patterns in parallel channels for fuel cells
Licensed content author	Lifeng Zhang, Hsiaotao T. Bi, David P. Wilkinson, Jürgen Stumper, Haijiang Wang
Licensed content date	1 September 2008
Licensed content volume number	183
Licensed content issue number	2
Number of pages	8
Start Page	643
End Page	650
Type of Use	reuse in a thesis/dissertation
Intended publisher of new work	other
Portion	figures/tables/illustrations
Number of figures/tables/illustrations	1

Permission to use Figure 5.14

Format	both print and electronic
Are you the author of this Elsevier article?	No
Will you be translating?	No
Title of your thesis/dissertation	Water transport through porous media and in flow channels of proton exchange membrane fuel cell
Expected completion date	Jul 2014
Estimated size (number of pages)	200
Elsevier VAT number	GB 494 6272 12
Permissions price	0.00 USD
VAT/Local Sales Tax	0.00 USD / 0.00 GBP
Total	0.00 USD
Terms and Conditions	

### INTRODUCTION

1. The publisher for this copyrighted material is Elsevier. By clicking "accept" in connection with completing this licensing transaction, you agree that the following terms and conditions apply to this transaction (along with the Billing and Payment terms and conditions established by Copyright Clearance Center, Inc. ("CCC"), at the time that you opened your Rightslink account and that are available at any time at <http://myaccount.copyright.com>).

### GENERAL TERMS

2. Elsevier hereby grants you permission to reproduce the aforementioned material subject to the terms and conditions indicated.

3. Acknowledgement: If any part of the material to be used (for example, figures) has appeared in our publication with credit or acknowledgement to another source, permission must also be sought from that source. If such permission is not obtained then that material may not be included in your publication/copies. Suitable acknowledgement to the source must be made, either as a footnote or in a reference list at the end of your publication, as follows:

"Reprinted from Publication title, Vol /edition number, Author(s), Title of article / title of chapter, Pages No., Copyright (Year), with permission from Elsevier [OR APPLICABLE SOCIETY COPYRIGHT OWNER]." Also Lancet special credit - "Reprinted from The Lancet, Vol. number, Author(s), Title of article, Pages No., Copyright (Year), with permission from Elsevier."

4. Reproduction of this material is confined to the purpose and/or media for which permission is hereby given.

5. Altering/Modifying Material: Not Permitted. However figures and illustrations may be altered/adapted minimally to serve your work. Any other abbreviations, additions, deletions and/or any other alterations shall be made only with prior written authorization of Elsevier Ltd. (Please contact Elsevier at [permissions@elsevier.com](mailto:permissions@elsevier.com))

Permission to use Figure 5.14, continue

# ELSEVIER LICENSE TERMS AND CONDITIONS

Jun 18, 2014

This is a License Agreement between Mehdi Mortazavi ("You") and Elsevier ("Elsevier") provided by Copyright Clearance Center ("CCC"). The license consists of your order details, the terms and conditions provided by Elsevier, and the payment terms and conditions.

**All payments must be made in full to CCC. For payment instructions, please see information listed at the bottom of this form.**

Supplier	Elsevier Limited The Boulevard, Langford Lane Kidlington, Oxford, OX5 1GB, UK
Registered Company Number	1982084
Customer name	Mehdi Mortazavi
Customer address	822 R.L. Smith HOUGHTON, MI 49931
License number	3412161492002
License date	Jun 18, 2014
Licensed content publisher	Elsevier
Licensed content publication	Journal of Power Sources
Licensed content title	Gas-liquid two-phase flow distributions in parallel channels for fuel cells
Licensed content author	Lifeng Zhang, Wei Du, Hsiaotao T. Bi, David P. Wilkinson, Jürgen Stumper, Haijiang Wang
Licensed content date	15 April 2009
Licensed content volume number	189
Licensed content issue number	2
Number of pages	9
Start Page	1023
End Page	1031
Type of Use	reuse in a thesis/dissertation
Intended publisher of new work	other
Portion	figures/tables/illustrations
Number of figures/tables/illustrations	1

Permission to use Figure 5.15

Format	both print and electronic
Are you the author of this Elsevier article?	No
Will you be translating?	No
Title of your thesis/dissertation	Water transport through porous media and in flow channels of proton exchange membrane fuel cell
Expected completion date	Jul 2014
Estimated size (number of pages)	200
Elsevier VAT number	GB 494 6272 12
Permissions price	0.00 USD
VAT/Local Sales Tax	0.00 USD / 0.00 GBP
Total	0.00 USD
Terms and Conditions	

### INTRODUCTION

1. The publisher for this copyrighted material is Elsevier. By clicking "accept" in connection with completing this licensing transaction, you agree that the following terms and conditions apply to this transaction (along with the Billing and Payment terms and conditions established by Copyright Clearance Center, Inc. ("CCC"), at the time that you opened your Rightslink account and that are available at any time at <http://myaccount.copyright.com>).

### GENERAL TERMS

2. Elsevier hereby grants you permission to reproduce the aforementioned material subject to the terms and conditions indicated.

3. Acknowledgement: If any part of the material to be used (for example, figures) has appeared in our publication with credit or acknowledgement to another source, permission must also be sought from that source. If such permission is not obtained then that material may not be included in your publication/copies. Suitable acknowledgement to the source must be made, either as a footnote or in a reference list at the end of your publication, as follows:

"Reprinted from Publication title, Vol /edition number, Author(s), Title of article / title of chapter, Pages No., Copyright (Year), with permission from Elsevier [OR APPLICABLE SOCIETY COPYRIGHT OWNER]." Also Lancet special credit - "Reprinted from The Lancet, Vol. number, Author(s), Title of article, Pages No., Copyright (Year), with permission from Elsevier."

4. Reproduction of this material is confined to the purpose and/or media for which permission is hereby given.

5. Altering/Modifying Material: Not Permitted. However figures and illustrations may be altered/adapted minimally to serve your work. Any other abbreviations, additions, deletions and/or any other alterations shall be made only with prior written authorization of Elsevier Ltd. (Please contact Elsevier at [permissions@elsevier.com](mailto:permissions@elsevier.com))

Permission to use Figure 5.15, continue

# ELSEVIER LICENSE TERMS AND CONDITIONS

Jun 18, 2014

This is a License Agreement between Mehdi Mortazavi ("You") and Elsevier ("Elsevier") provided by Copyright Clearance Center ("CCC"). The license consists of your order details, the terms and conditions provided by Elsevier, and the payment terms and conditions.

**All payments must be made in full to CCC. For payment instructions, please see information listed at the bottom of this form.**

Supplier	Elsevier Limited The Boulevard, Langford Lane Kidlington, Oxford, OX5 1GB, UK
Registered Company Number	1982084
Customer name	Mehdi Mortazavi
Customer address	822 R.L. Smith HOUGHTON, MI 49931
License number	3412170159045
License date	Jun 18, 2014
Licensed content publisher	Elsevier
Licensed content publication	Journal of Power Sources
Licensed content title	Two-phase flow pressure drop hysteresis in an operating proton exchange membrane fuel cell
Licensed content author	Ryan Anderson, David P. Wilkinson, Xiaotao Bi, L. Zhang
Licensed content date	1 October 2011
Licensed content volume number	196
Licensed content issue number	19
Number of pages	10
Start Page	8031
End Page	8040
Type of Use	reuse in a thesis/dissertation
Intended publisher of new work	other
Portion	figures/tables/illustrations
Number of figures/tables/illustrations	1
Format	both print and electronic

Permission to use Figure 5.16

Are you the author of this Elsevier article?	No
Will you be translating?	No
Title of your thesis/dissertation	Water transport through porous media and in flow channels of proton exchange membrane fuel cell
Expected completion date	Jul 2014
Estimated size (number of pages)	200
Elsevier VAT number	GB 494 6272 12
Permissions price	0.00 USD
VAT/Local Sales Tax	0.00 USD / 0.00 GBP
Total	0.00 USD
Terms and Conditions	

### INTRODUCTION

1. The publisher for this copyrighted material is Elsevier. By clicking "accept" in connection with completing this licensing transaction, you agree that the following terms and conditions apply to this transaction (along with the Billing and Payment terms and conditions established by Copyright Clearance Center, Inc. ("CCC"), at the time that you opened your Rightslink account and that are available at any time at <http://myaccount.copyright.com>).

### GENERAL TERMS

2. Elsevier hereby grants you permission to reproduce the aforementioned material subject to the terms and conditions indicated.

3. Acknowledgement: If any part of the material to be used (for example, figures) has appeared in our publication with credit or acknowledgement to another source, permission must also be sought from that source. If such permission is not obtained then that material may not be included in your publication/copies. Suitable acknowledgement to the source must be made, either as a footnote or in a reference list at the end of your publication, as follows:

“Reprinted from Publication title, Vol /edition number, Author(s), Title of article / title of chapter, Pages No., Copyright (Year), with permission from Elsevier [OR APPLICABLE SOCIETY COPYRIGHT OWNER].” Also Lancet special credit - “Reprinted from The Lancet, Vol. number, Author(s), Title of article, Pages No., Copyright (Year), with permission from Elsevier.”

4. Reproduction of this material is confined to the purpose and/or media for which permission is hereby given.

5. Altering/Modifying Material: Not Permitted. However figures and illustrations may be altered/adapted minimally to serve your work. Any other abbreviations, additions, deletions and/or any other alterations shall be made only with prior written authorization of Elsevier Ltd. (Please contact Elsevier at [permissions@elsevier.com](mailto:permissions@elsevier.com))

6. If the permission fee for the requested use of our material is waived in this instance, please be

Permission to use Figure 5.16, continue

# ELSEVIER LICENSE TERMS AND CONDITIONS

Jun 18, 2014

This is a License Agreement between Mehdi Mortazavi ("You") and Elsevier ("Elsevier") provided by Copyright Clearance Center ("CCC"). The license consists of your order details, the terms and conditions provided by Elsevier, and the payment terms and conditions.

**All payments must be made in full to CCC. For payment instructions, please see information listed at the bottom of this form.**

Supplier	Elsevier Limited The Boulevard, Langford Lane Kidlington, Oxford, OX5 1GB, UK
Registered Company Number	1982084
Customer name	Mehdi Mortazavi
Customer address	822 R.L. Smith HOUGHTON, MI 49931
License number	3412170316921
License date	Jun 18, 2014
Licensed content publisher	Elsevier
Licensed content publication	Chemical Engineering Science
Licensed content title	Gas-liquid two-phase flow behavior in minichannels bounded with a permeable wall
Licensed content author	Lifeng Zhang, Xiaotao T. Bi, David P. Wilkinson, Ryan Anderson, Jürgen Stumper, Haijiang Wang
Licensed content date	15 July 2011
Licensed content volume number	66
Licensed content issue number	14
Number of pages	9
Start Page	3377
End Page	3385
Type of Use	reuse in a thesis/dissertation
Intended publisher of new work	other
Portion	figures/tables/illustrations
Number of figures/tables/illustrations	2

Permission to use Figures 5.17 and 5.18



Format	both print and electronic
Are you the author of this Elsevier article?	No
Will you be translating?	No
Title of your thesis/dissertation	Water transport through porous media and in flow channels of proton exchange membrane fuel cell
Expected completion date	Jul 2014
Estimated size (number of pages)	200
Elsevier VAT number	GB 494 6272 12
Permissions price	0.00 USD
VAT/Local Sales Tax	0.00 USD / 0.00 GBP
Total	0.00 USD
Terms and Conditions	

### INTRODUCTION

1. The publisher for this copyrighted material is Elsevier. By clicking "accept" in connection with completing this licensing transaction, you agree that the following terms and conditions apply to this transaction (along with the Billing and Payment terms and conditions established by Copyright Clearance Center, Inc. ("CCC"), at the time that you opened your Rightslink account and that are available at any time at <http://myaccount.copyright.com>).

### GENERAL TERMS

2. Elsevier hereby grants you permission to reproduce the aforementioned material subject to the terms and conditions indicated.

3. Acknowledgement: If any part of the material to be used (for example, figures) has appeared in our publication with credit or acknowledgement to another source, permission must also be sought from that source. If such permission is not obtained then that material may not be included in your publication/copies. Suitable acknowledgement to the source must be made, either as a footnote or in a reference list at the end of your publication, as follows:

"Reprinted from Publication title, Vol /edition number, Author(s), Title of article / title of chapter, Pages No., Copyright (Year), with permission from Elsevier [OR APPLICABLE SOCIETY COPYRIGHT OWNER]." Also Lancet special credit - "Reprinted from The Lancet, Vol. number, Author(s), Title of article, Pages No., Copyright (Year), with permission from Elsevier."

4. Reproduction of this material is confined to the purpose and/or media for which permission is hereby given.

5. Altering/Modifying Material: Not Permitted. However figures and illustrations may be altered/adapted minimally to serve your work. Any other abbreviations, additions, deletions and/or any other alterations shall be made only with prior written authorization of Elsevier Ltd. (Please contact Elsevier at [permissions@elsevier.com](mailto:permissions@elsevier.com))

Permission to use Figures 5.17 and 5.18, continue